DISSERTATION

# ATMOSPHERIC PROCESSING OF CHEMICAL COMPOUNDS AND DIRECT MEASUREMENTS OF PARTICLE LOSS BY DRY AND WET DEPOSITION

Submitted by

Ethan Walker Emerson

Department of Chemistry

In partial fulfillment of the requirements

For the Degree of Doctor of Philosophy

Colorado State University

Fort Collins, Colorado

Fall 2019

Doctoral Committee:

Advisor: Delphine Farmer
Co-Advisor: James Neilson

A.R. Ravi Ravishankara
Thomas Borch
George Barisas
Shantanu Jathar

# ABSTRACT

## ATMOSPHERIC PROCESSING OF CHEMICAL COMPOUNDS AND DIRECT MEASUREMENTS OF PARTICLE LOSS BY DRY AND WET DEPOSITION

Anthropogenic pollutants, like $NO_x$ and black carbon (BC), are ubiquitous in the atmosphere and impact human health and the climate. Understanding the atmospheric fate of such pollutants is critical in understanding their impact. This work focuses on understanding the loss of two key pollutants: the chemical termination of gas phase NO and $NO_2$ ($NO_x$) and the deposition of refractory black carbon (rBC) particles. Additionally, because the tools to analyze particle fluxes and coated rBC are lacking, this work describes the development of software to analyze particle fluxes and estimate the thickness of organic coatings on rBC.

Removal of aerosols from the atmosphere occurs via wet and dry deposition. Black carbon (BC) is one form of aerosol that impacts atmospheric temperature, cloud formation and properties, the albedo of snow and ice surfaces, and the timing of snowmelt. Parameterization of BC dry deposition is particularly limited due to the lack of available instrumentation for measuring the process, and thus there is a lack of observational datasets with which to evaluate existing models. We present observations of dry and wet deposition rates of size-resolved coated rBC and total aerosol number by eddy covariance technique using a single particle soot photometer (SP2; Droplet Measurement Technologies Inc.) and ultra high sensitivity aerosol spectrometer (UHSAS; Droplet Measurement Technologies Inc.) from the remote Southern Great Plains ARM Climate Research facility in north-central Oklahoma. Using these data, we show that (1) wet deposition dominates the removal of rBC from the atmosphere, (2) dry

deposition measurements agree with sophisticated deposition parameterizations, and (3) a simple parameterization adequately describes size-resolved deposition. We assess the implications of this parameterization in GEOS-Chem.

Size-resolved deposition schemes, such as those used in current chemical transport models use schemes that have not been compared to recent measurements. Using aggregated deposition velocities from literature observations and those collected by our group, we show that the current scheme used in chemical transport models does not accurately describe observed deposition velocities. Highly sophisticated leaf level models can accurately describe the aggregated observations, but they are ill-suited to global chemical transport models. We present a simple scheme that reasonably describes size-resolved particle deposition in a simple sectional scheme that includes atmospheric parameters. The result of this update is substantial changes in particle concentrations across the globe and these impact cloud condensation nuclei, the direct and indirect effects, and PM2.5 concentrations.

$NO_x$ is a key pollutant that propagates atmospheric chemistry through the coupled $HO_x$-$NO_x$ cycle. Trace gas measurements from the 2015 spring and summer SONGNEX campaign conducted at the Boulder Atmospheric Observatory (BAO) in Northern Front Range Metropolitan Area of Colorado (NFRMA) are characteristic of environment impacted by oil and natural gas, agricultural operations, traffic, biogenic, and urban sources. Using a previously published PMF analysis of volatile organic compounds, we show the impact of a changing atmospheric composition due to emissions from anthropogenic sources on $NO_x$ sinks and the implications of $HO_x$-$NO_x$ propagation through box modelling. These results indicate that the NFRMA is sensitive to $NO_x$ and VOC mixing ratios during spring, summer, and smoke-impacted periods.

# ACKNOWLEDGEMENTS

The work that has gone into this dissertation would not have been possible without the help and patience of many people. First and foremost, I'd like to thank and acknowledge my parents Robin and Lee who've always been there for me. I do not think this process would have been possible without the sage advice you've always offered and willingness to listen to me. Megan, you've always been there and whether I like it or not, you make me get outside and get out of my own head. To the friends who've been here and turned Fort Collins and Colorado State University into an incredible community I could not have dreamed of and would never have believed. You all made this a far more enjoyable experience from on campus to off and everything in between.

# DEDICATION

To Ken and Margaret Emerson

*They always found new tracks*

TABLE OF CONTENTS

# INTRODUCTION – PERSISTANCE OF ATMOSPHERIC POLLUTANTS

The atmosphere is a dynamic environment that is made up of gas phase and condensed phase material. Data strongly supports the idea that the climate is changing and on average, warming (Houghton and Intergovernmental Panel on Climate Change. Working Group I., 2001;Solomon et al., 2007;Stocker, 2014). Carbon dioxide is well understood to be a strong climate forcer and is known to absorb incident radiation from the sun and retain that energy and thus having a warming effect on the planet. As carbon dioxide has increased in concentration, because of combustion processes associated with human activities, the climate has warmed (Metz and Intergovernmental Panel on Climate Change. Working Group III., 2007;Charney, 1979). The earth's atmosphere is influenced by many constituents beyond carbon dioxide and these components influence climate, human health, terrestrial and marine landscapes, and all other planetary species (Jerrett et al., 2009;Cohen et al., 2005;Gwinn et al., 2011;IPCC;Houghton and Intergovernmental Panel on Climate Change. Working Group I., 2001;Solomon et al., 2007;Stocker, 2014;McCarthy and Intergovernmental Panel on Climate Change. Working Group II., 2001).

Earth's radiative balance can be used as a quantitative and conceptual tool to understand the warming or cooling impact a gas phase or condensed phase component can have. Solar radiation is constantly impinging on the earth's atmosphere. This radiation can either be absorbed in the atmosphere or by land and sea surfaces or scattered back into space by those same surfaces (Seinfeld and Pandis, 2006). The impact atmospheric constituents have on the radiative balance of the earth and on human health or ecosystems due to degraded air quality and toxicity is largely a

function of the time they spend in the atmosphere - their 'atmospheric lifetime' (Jerrett et al., 2009;Cohen et al., 2005;Gwinn et al., 2011;IPCC).

Imagine that every individual molecule and particle emitted into the atmosphere could be tracked. Further imagine we could fully understand all processes that dictate the climate and health effects of all atmospheric constituents. While the current state of science lacks this resolution in the atmosphere we have effective frameworks to understand and 'track' atmospheric constituents. Figure 0.1 provides a conceptual framework that is efficiently describes key atmospheric processes. This framework highlights two key components of atmospheric lifetime: sources and sinks. These components drive atmospheric lifetime and the impact an atmospheric constituent can have on either human health, climate, or many other effects. There are two sources for an atmospheric constituent: direct emission and atmospheric production. Direct emission is an anthropogenic or biogenic process that directly injects either particles or gas phase molecules into the atmosphere. Additionally, particles and gas phase molecules can be formed in the atmosphere through homogenous nucleation or oxidation, respectively. There are two loss processes for an atmospheric constituent as well. Particles and molecules can be directly lost to the Earth's surface by wet or dry deposition. Similar to atmospheric formation, both particles and molecules can be lost to the atmosphere through oxidative reactions or particle-to-gas phase partitioning. The atmospheric lifetime of any constituent is a function of the sources and sinks.

Atmospheric production and loss can also be described as an atmospheric transformation. Atmospheric transformation processes are the chemical or physical interactions that molecules and particles undergo in the atmosphere (Figure 0.2). Directly emitted chemical compounds from either anthropogenic or biogenic emissions are oxidized by reactive species in the atmosphere such as gas phase radicals (e.g. OH, $NO_3$, $RO_2$, or $HO_2$), molecular species (e.g. $O_3$), Criegee biradicals,

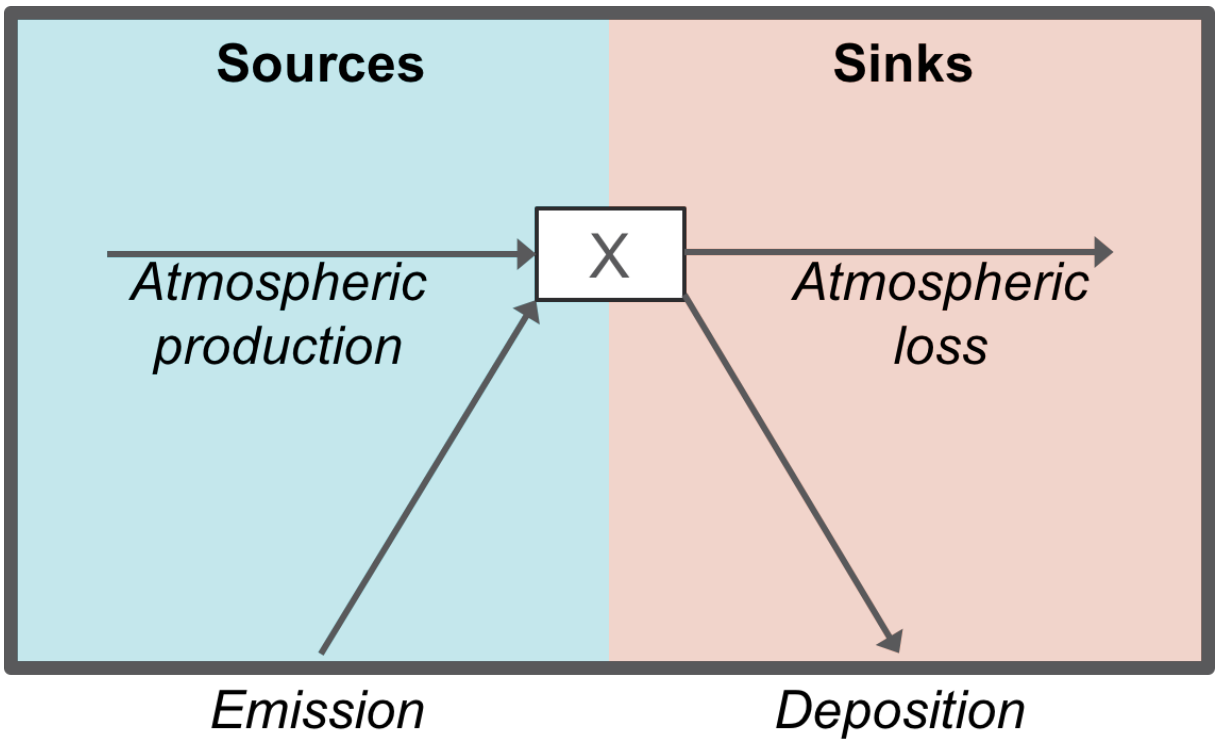


**Figure 0.1**: Schematic representation of atmospheric sources and sinks of particles and molecules.

and halogen radicals (e.g. Cl) (Jacob, 1999;Seinfeld and Pandis, 2006). Depending on their vapor pressure and other chemical properties, directly emitted and secondary gas phase molecules may undergo homogenous nucleation to form particles (Kirkby et al., 2016), or condense onto the surfaces of existing particles thereby affecting the phase state, surface chemistry, and size of the particle (Seinfeld and Pandis, 2006;Hinds, 1999). Additionally, particles can also be directly emitted by either anthropogenic or biogenic sources and undergo atmospheric processing. These processes include coagulation, surface oxidation, and heterogeneous chemistry. Figure 0.2 shows a schematic representation of gas and condensed phase atmospheric processing.

The degree of atmospheric processing that gas and condensed phase material undergoes can impact the climate and human health. Particles can serve as nucleation points for clouds ('cloud condensation nuclei', CCN) and ice ('ice nuclei', IN) which in turn have a pronounced effect on indirect radiative effect. Size is the dominant factor determining CCN activity, but chemical composition has an effect, with more hygroscopic particles typically being more effective CCN. Furthermore, the degree of atmospheric processing drives particle 'browning' or 'bleaching' which has a substantial impact on the direct radiative effect (Laskin et al., 2015;Zhao et al., 2015). Additionally, anthropogenic emissions of gas phase ammonia and nitric acid can react to form particle nitrate which can be transported and deposit in more remote regions that are sensitive to nitrogen fertilization (Benedict et al., 2013;Thompson et al., 2015). Atmospheric transformation changes particle and gas phase properties which changes the impact these particles and molecules have on the environment, human health and the rate at which they are removed from the atmosphere. For example, oxygenation often increases the solubility of gas phase molecules, thought to enhance dry deposition rates of gases (Nguyen et al., 2015).

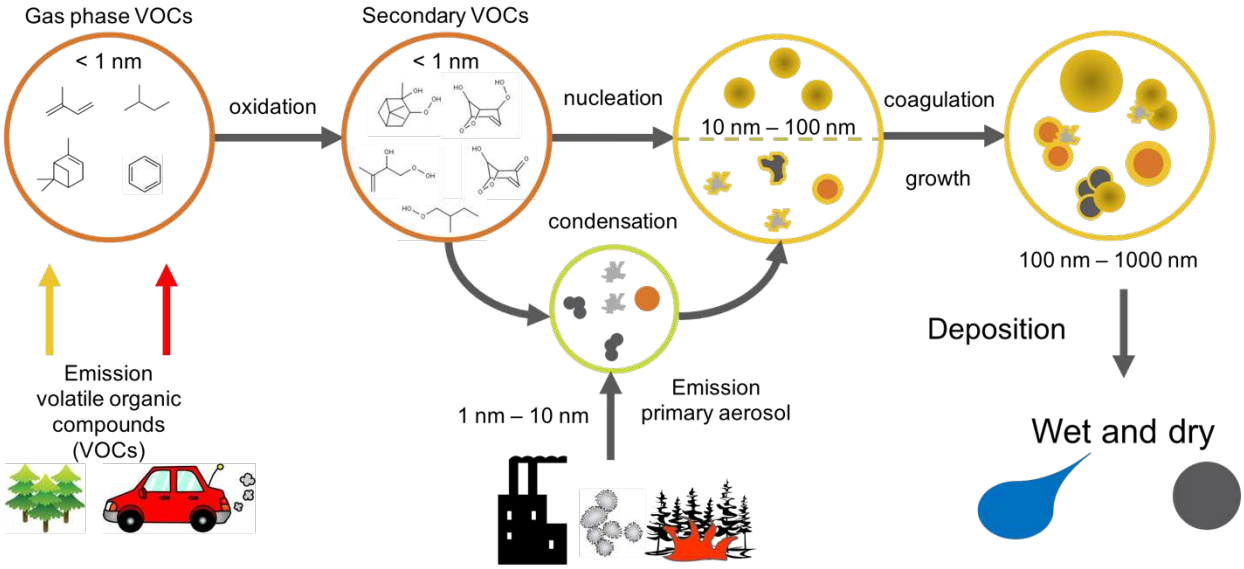


**Figure 0.2**: Schematic representation of atmospheric oxidation of gas phase constituents and condensed phase particle processing.

Atmospheric removal processes can be grouped in chemical loss (i.e. chemical transformation) and surface removal. Atmospheric surface removal processes are divided into two categories: wet and dry deposition. Chemical transformations in the atmosphere can occur by oxidation, photolysis, thermal decomposition, and heterogeneous chemistry thus removing a particular molecule (Jacob, 1999). This process can result in changes to the radiative or toxic effect of molecule. Chemical loss processes are typically first, second, or third order reactions (Table 1).

**Table 0.1**: Reaction order, reaction, and the relationship to chemical lifetime.

| Reaction order | Reaction | Lifetime |
|---|---|---|
| First order | $A \overset{k_1}{\rightarrow} Products$ | $\tau = \frac{1}{k_1}$ |
| Second order | $A + B \overset{k_2}{\rightarrow} Products$ | $\tau = \frac{1}{k_1[B]}$ |
| Third order | $A + B + C \overset{k_3}{\rightarrow} Products$ | $\tau = \frac{1}{k_1[B][C]}$ |

Wet deposition describes all processes by which any molecule or particle is lost from the atmosphere to the Earth's surface in an aqueous form. This process can be further described in three common methods: (1) dissolution of atmospheric gases into liquid phase water (e.g. direct uptake by cloud or fog droplets), (2) removal of particles that behave as a nucleation point for cloud droplets or ice crystals, and (3) removal of particles through direct impaction by precipitation below a cloud. These three processes result in gases or particles eventually being removed from the atmosphere and entering Earth's surface, and can thus be considered mechanisms of deposition. The less nuanced, but no less important process, is dry deposition which refers to a direct transfer process of molecules or particles to the Earth's surface in either the gas phase or condensed phase. Wet and dry deposition are typically thought to be a first order loss process (Seinfeld and Pandis, 2006). Chemical reactions in the atmosphere result further oxidized products and thus the loss of

the original reactant, but is distinct from deposition processes which are a true loss of some compound or particle from the atmosphere. However, chemical transformation can substantially alter the radiative forcing of the planet and influence the rate at which a particle or molecule is lost via wet or dry deposition (Hansen and Sato, 2001;Hansen and Sato, 2004;Stocker, 2014).

Atmospheric lifetime refers to the total lifetime molecules or particles spend in the atmosphere, but because multiple processes can impact the lifetime, we can consider atmospheric lifetime of gas phase molecules as the inverse sum of loss rates with respect to individual processes:

| | | |
|---|---|---|
| | $\tau = \frac{V_{dry\ dep.}}{BLH} + \frac{1}{k_{Ox}[Ox]} + \cdots$ | (0.1) |

Thus, we can consider the lifetime for gas phase molecules with respect to a particular oxidant. The lifetime against oxidation depends on both the rate constants and on the concentration of the oxidant. Understanding the chemical reactions and mixtures that lead to these adverse compounds is essential to mitigating the impact and implementing effective control strategies.

Particulate matter directly and indirectly affects climate. This impact is a function of direct emissions, particle formation, and deposition processes. Substantial efforts have been placed into refining emission inventories across many sectors, both anthropogenic and biogenic. Substantial work has also gone into understanding particle formation in the atmosphere from a process oriented perspective. However, far less work has been put into the deposition process, especially dry deposition. Measurements of dry deposition are typically a challenging measurement to make, especially for particles as the measurements are stochastic and finite. These are essential measurements and it is imperative to understand the loss rate to understand their atmospheric lifetime. Emission inventories could be substantially inaccurate if the loss rates are incorrect.

Reducing global climate model uncertainty is essential to understanding the impact of anthropogenic influence and feedback loops that may exist beyond our current understanding.

This work focuses on two aspects of the atmosphere. Initially, the chemical lifetime and processing of a direct anthropogenic pollutant NO and $NO_2$ are examined through measurements and modelling of data obtained in the Northern Front Range of Colorado. I then examine particulate dry and wet deposition. This demonstrates a novel approach to characterizing refractory black carbon deposition rates, and allows us to partition the relative importance of wet versus dry deposition as surface removal processes for particles. Total scattering aerosol particles are also examined through data collected at two field sites and compared with a large set of previously published datasets. These measurements allow me to develop a new parameterization that is implemented into a chemical transport model to understand how an observationally motivated parameterization could affect a wide swath of processes that involve particulate matter in the atmosphere.

INTRODUCTION REFERENCES


Benedict, K. B., Carrico, C. M., Kreidenweis, S. M., Schichtel, B., Malm, W. C., and Collett, J. L.: A seasonal nitrogen deposition budget for Rocky Mountain National Park, Ecol Appl, 23, 1156-1169, 10.1890/12-1624.1, 2013.

Charney, J. G.: Carbon dioxide and climate: a scientific assessment, 1979.

Cohen, A. J., Ross Anderson, H., Ostro, B., Pandey, K. D., Krzyzanowski, M., Kunzli, N., Gutschmidt, K., Pope, A., Romieu, I., Samet, J. M., and Smith, K.: The global burden of disease due to outdoor air pollution, J Toxicol Environ Health A, 68, 1301-1307, 10.1080/15287390590936166, 2005.

Gwinn, M. R., Craig, J., Axelrad, D. A., Cook, R., Dockins, C., Fann, N., Fegley, R., Guinnup, D. E., Helfand, G., Hubbell, B., Mazur, S. L., Palma, T., Smith, R. L., Vandenberg, J., and Sonawane, B.: Meeting Report: Estimating the Benefits of Reducing Hazardous Air Pollutants-Summary of 2009 Workshop and Future Considerations, Environ Health Persp, 119, 125-130, 10.1289/ehp.1002468, 2011.

Hansen, J., and Sato, M.: Greenhouse gas growth rates, P Natl Acad Sci USA, 101, 16109-16114, 10.1073/pnas.0406982101, 2004.

Hansen, J. E., and Sato, M.: Trends of measured climate forcing agents, P Natl Acad Sci USA, 98, 14778-14783, DOI 10.1073/pnas.261553698, 2001.

Hinds, W. C.: Aerosol technology : properties, behavior, and measurement of airborne particles, 2nd ed., Wiley, New York, xx, 483 p. pp., 1999.

Houghton, J. T., and Intergovernmental Panel on Climate Change. Working Group I.: Climate change 2001 : the scientific basis : contribution of Working Group I to the third assessment report of the Intergovernmental Panel on Climate Change, Cambridge University Press, Cambridge ; New York, x, 881 p. pp., 2001.

IPCC: Climate Change 2013: The Physical Science Basis. Contribution of Working Group I to the Fifth Assessment Report of the Intergovernmental Panel on Climate Change.

Jacob, D. J.: Introduction to Atmospheric Chemistry, Princeton University Press, 1999.

Jerrett, M., Burnett, R. T., Pope, C. A., 3rd, Ito, K., Thurston, G., Krewski, D., Shi, Y., Calle, E., and Thun, M.: Long-term ozone exposure and mortality, N Engl J Med, 360, 1085-1095, 10.1056/NEJMoa0803894, 2009.

Kirkby, J., Duplissy, J., Sengupta, K., Frege, C., Gordon, H., Williamson, C., Heinritzi, M., Simon, M., Yan, C., Almeida, J., Trostl, J., Nieminen, T., Ortega, I. K., Wagner, R., Adamov, A., Amorim, A., Bernhammer, A. K., Bianchi, F., Breitenlechner, M., Brilke, S., Chen, X., Craven, J., Dias, A., Ehrhart, S., Flagan, R. C., Franchin, A., Fuchs, C., Guida, R., Hakala, J., Hoyle, C. R., Jokinen, T., Junninen, H., Kangasluoma, J., Kim, J., Krapf, M., Kurten, A., Laaksonen, A., Lehtipalo, K., Makhmutov, V., Mathot, S., Molteni, U., Onnela, A., Perakyla, O., Piel, F., Petaja, T., Praplan, A. P., Pringle, K., Rap, A., Richards, N. A., Riipinen, I., Rissanen, M. P., Rondo, L., Sarnela, N., Schobesberger, S., Scott, C. E., Seinfeld, J. H., Sipila, M., Steiner, G., Stozhkov, Y., Stratmann, F., Tome, A., Virtanen, A., Vogel, A. L., Wagner, A. C., Wagner, P. E., Weingartner, E., Wimmer, D., Winkler, P. M., Ye, P., Zhang, X., Hansel, A., Dommen, J., Donahue, N. M., Worsnop, D. R., Baltensperger, U., Kulmala, M., Carslaw, K. S., and Curtius, J.: Ion-induced nucleation of pure biogenic particles, Nature, 533, 521-526, 10.1038/nature17953, 2016.

Laskin, A., Laskin, J., and Nizkorodov, S. A.: Chemistry of atmospheric brown carbon, Chem Rev, 115, 4335-4382, 10.1021/cr5006167, 2015.

McCarthy, J. J., and Intergovernmental Panel on Climate Change. Working Group II.: Climate change 2001 : impacts, adaptation, and vulnerability : contribution of Working Group II to the third assessment report of the Intergovernmental Panel on Climate Change, Cambridge University Press, Cambridge, UK ; New York, x, 1032 p. pp., 2001.

Metz, B., and Intergovernmental Panel on Climate Change. Working Group III.: Climate change 2007 : mitigation of climate change : contribution of Working Group III to the Fourth assessment report of the Intergovernmental Panel on Climate Change, Cambridge University Press, Cambridge ; New York, x, 851 p. pp., 2007.

Nguyen, T. B., Crounse, J. D., Teng, A. P., St Clair, J. M., Paulot, F., Wolfe, G. M., and Wennberg, P. O.: Rapid deposition of oxidized biogenic compounds to a temperate forest, Proc Natl Acad Sci U S A, 112, E392-401, 10.1073/pnas.1418702112, 2015.

Seinfeld, J. H., and Pandis, S. N.: Atmospheric chemistry and physics : from air pollution to climate change, 2nd ed. ed., J. Wiley, Hoboken, N.J., 2006.

Solomon, S., Intergovernmental Panel on Climate Change., and Intergovernmental Panel on Climate Change. Working Group I.: Climate change 2007 : the physical science basis : contribution of Working Group I to the Fourth Assessment Report of the Intergovernmental Panel on Climate Change, Cambridge University Press, Cambridge ; New York, viii, 996 p. pp., 2007.

Stocker, T.: Climate change 2013 : the physical science basis : Working Group I contribution to the Fifth assessment report of the Intergovernmental Panel on Climate Change, Cambridge University Press, New York, xi, 1535 pages. pp., 2014.

Thompson, T. M., Rodriguez, M. A., Barna, M. G., Gebhart, K. A., Hand, J. L., Day, D. E., Malm, W. C., Benedict, K. B., Collett, J. L., and Schichtel, B. A.: Rocky Mountain National Park reduced nitrogen source apportionment, Journal of Geophysical Research: Atmospheres, 120, 4370-4384, 10.1002/2014jd022675, 2015.

Zhao, R., Lee, A. K. Y., Huang, L., Li, X., Yang, F., and Abbatt, J. P. D.: Photochemical processing of aqueous atmospheric brown carbon, Atmospheric Chemistry and Physics, 15, 6087-6100, 10.5194/acp-15-6087-2015, 2015.

# CHAPTER 1 – ANTHROPOGENIC SOURCES INFLUENCE $O_3$ AND $NO_y$ IN THE FRONT RANGE OF COLORADO[1]

## Overview

Using a suite of measurements collected during the spring and summer of 2015, positive matrix factorization (PMF) analysis, and zero-dimensional box modelling, we investigate the role played by different VOC sources and $NO_x$ in determining production of ozone, nitric acid, organic nitrate, and peroxy nitrate. A deficit between total reactive nitrogen oxides ($NO_y$) and observed components occurs in the summer, but can be at least partially reconciled by modeled organic nitrates stemming from non-methane volatile organic compounds (NMVOCs), and isoprene in particular. A box model shows that NMVOCs associated with oil and natural gas are substantial levers on the ozone, nitric acid, and peroxy nitrate budgets in both spring and summer – although summer time isoprene also plays an important role. The average chemical system predisposes the region to high ozone events from even small additions of NMVOC or $NO_x$ via anthropogenic or wildfire sources as the system is sensitive to small changes in both ozone precursors. We estimate that on average oil and natural gas NMVOCs contribute to 30% of the ozone production, and influence all aspects of the $NO_y$ budget.

## Introduction

Tropospheric ozone ($O_3$) is an atmospheric oxidant, a greenhouse gas, and an air pollutant that causes adverse effects on human health and ecosystems [*Bell et al.*, 2005; *Booker et al.*, 2009; *Selin et al.*, 2009; *Silverman and Ito*, 2009]. $O_3$ reacts with other compounds in the atmosphere to

[1] This chapter is with coauthors for review. All analysis of this publicly available data was carried out by Ethan W. Emerson. Measurements were collected by a team of scientists from Colorado State University and Aerodyne including, Emily V. Fischer, Ilana B. Pollack, Andrew Abeleira, Rob Roscioli, Scott Herndon, Jakob Lindaas, and Delphine K. Farmer.

form secondary organic aerosols, which have known adverse effects on human health, but uncertain impacts on climate [*Change*, 2014; *Pope and Dockery*, 2006]. In the past two decades, $O_3$ mixing ratios in the eastern US have decreased in response to declines in $NO_x$ emissions. In contrast, the western US has experienced only moderate decreases or even increases in surface $O_3$ mixing ratios across the high elevation states [*Butler et al.*, 2011; *Owen R. Cooper et al.*, 2012; *O. R. Cooper et al.*, 2015]. Several hypotheses have emerged to explain the aberrant western US ozone trends including increased anthropogenic emissions of volatile organic compounds (VOCs) through non-traditional oil and gas development, increased incidence of wildfires releasing $O_3$ precursors, and decreased $NO_x$ emissions and thus increased $O_3$ in $NO_x$-saturated environments [*A J Abeleira and Farmer*, 2017; *Brey and Fischer*, 2016; *Cheadle et al.*, 2017; *McDuffie et al.*, 2016]. Understanding the sensitivity of relevant urban and sub-urban regions to $O_3$ precursors, and the role of different source factors in controlling $O_3$ production and termination reactions is essential for developing effective control strategies.

Tropospheric $O_3$ formation results from the oxidation of hydrocarbons in the presence of nitrogen oxide radicals ($NO_x = NO + NO_2$) by the catalytic $HO_x$-$NO_x$ cycles (R1-R6 and Figure 1). At low concentrations, $NO_x$ reacts with $HO_x$ radicals ($HO_x = OH + RO_2 + RO + HO_2$) to catalytically form ozone. At high concentrations, $NO_x$ reactions terminate the cycle. Termination products such as nitric acid ($HNO_3$), organic nitrates (ANs or $RONO_2$), and PAN (peroxyacetyl nitrate) typically comprise the bulk of oxidized nitrogen ($NO_z$, $NO_z \equiv NO_y - NO_x$), and thus total reactive nitrogen oxides ($NO_y = NO_z + NO_x$) in suburban and remote regions downwind of fresh $NO_x$ emissions [*Douglas A. Day*, 2003; *D. A. Day et al.*, 2009; *Murphy et al.*, 2006]. Chain termination reactions, and thus partitioning of these $NO_z$ components, impact how much $O_3$ can be formed in a given airmass [*Farmer et al.*, 2011; *Perring et al.*, 2010].

$$OH + RH + O_2 \longrightarrow RO_2 + H_2O \quad (R1)$$
$$RO_2 + NO \longrightarrow RO + NO_2 \quad (R2a)$$
$$RO_2 + NO \longrightarrow RONO_2 \quad (R2b)$$
$$RO + O_2 \longrightarrow R'C(O) + HO_2 \quad (R3)$$
$$HO_2 + NO \longrightarrow OH + NO_2 \quad (R4)$$
$$NO_2 + h\nu \longrightarrow NO + O(^3P) \quad (R5)$$
$$O(^3P) + O_2 + M \longrightarrow O_3 + M \quad (R6)$$

The formation of $RONO_2$ species in reaction R2b represent a chain termination step that competes with $NO_2$ formation and thus relates to the production of $O_3$. Competing chain termination reactions (R6-8) give rise to the non-linear behavior of $P(O_3)$ for varying $NO_x$ at constant VOC reactivity [*Kleinman*, 2005; *X Lin et al.*, 1988; *Liu and Trainer*, 1988; *Liu et al.*, 1987b; *Murphy et al.*, 2006; *Murphy et al.*, 2007; *Thornton*, 2002]. $NO_x$-limited regimes occur when the ratio of $NO_x$ to gas phase VOCs is low; chain termination primarily occurs by removal of $HO_2$ and $RO_2$ radicals by formation of peroxides and $NO_x$ addition increases R2a and R4, and thus $P(O_3)$. Under a VOC-limited regime, termination steps are dominated by $HNO_3$ formation (R7), and the addition of $NO_x$ decreases $P(O_3)$.

$$OH + NO_2 + M \longrightarrow HNO_3 + M \quad (R7)$$

Peroxy nitrates (PNs or $RO_2NO_2$, typically peroxy acyl nitrates; R8) maximize with $O_3$ production due to the simultaneous need for both $RO_2$ and $NO_x$, and are temporary reservoirs for $NO_x$ as they thermally decompose to (re-)release $NO_x$ (R8) [*Sanford Sillman and Samson*, 1995].

$$RO_2 + NO_2 \rightleftharpoons RO_2NO_2 \quad (R8)$$

PN chemistry redistributes $NO_x$ from urban areas where $NO_x$ is emitted to downwind suburban, rural, or remote regions on a regional and global scale [*Heald et al.*, 2003; *Hudman et al.*, 2004; *Moxim et al.*, 1996; *Singh and Hanst*, 1981].

$RONO_2$ production also maximizes with $O_3$ production, and is typically considered a permanent sink for $NO_x$, although some evidence points to eventual release of $NO_x$ in some cases [*Horowitz et al.*, 2007; *Ito et al.*, 2009; *Moxim et al.*, 1996; *Perring et al.*, 2009; *Shepson et al.*, 1993]. Gas phase organic nitrates can be transported, further reacted, deposited, or incorporated into the aerosol phase [*Koppmann*, 2007]. The rates of each of these steps are dictated by the structures of the R groups, and thus the identity of the parent hydrocarbon (RH). Products of $RONO_2$ oxidation by OH, $O_3$, and $NO_3$ follow two possible pathways: further functionalization to form a stable multifunctional nitrate, or release of $NO_2$. Laboratory experiments indicate that longer linear alkanes are more likely to retain nitrate functionality [*Aschmann et al.*, 2011]. Additionally, retention of the nitrate group is expected if the functional group is well separated from the most reactive hydrogen atoms or remaining double bonds *Aschmann et al.* [2011]. It has been shown that neglecting organic nitrate formation when reducing VOCs reactivity would overestimate $O_3$ production [*Farmer et al.*, 2011; *Perring et al.*, 2013].

Here we investigate the effect of VOC mixtures on $NO_y$ speciation using *in situ* measurements from the Boulder Atmospheric Observatory (BAO) site in the Northern Front Range Metropolitan Area of Colorado (NFRMA) in summer 2015. Multiple counties in the NFRMA have exceeded the EPA National Ambient Air Quality Standard for $O_3$ since 2008, and the region is a moderate non-attainment region for $O_3$. Despite this designation and the close link between $NO_z$ and $O_3$ described above, the region lacks a detailed analysis of the total summertime $NO_y$ budget. Unlike most other US metropolitan regions, where summertime $O_3$ has declined over the last two decades, summertime $O_3$ in the NFRMA has increased [*Strode et al.*, 2015]. All categories of anthropogenic VOC emissions have decreased slightly since 2000 except for ONG emissions, which increased between 2000 and 2011 ($7.4\times10^3$ to $2.6\times10^5$ tons) and in 2015 was $1.5\times10^5$ tons

[*A Abeleira et al.*, 2017; *A J Abeleira and Farmer*, 2017]. The NFRMA may be distinct from many eastern US regions because urban sources of air pollutants (i.e. traffic and light industrial) are adjacent to intense fossil fuel refining operations and wide land areas with large emissions from oil and natural gas production and concentrated agriculture feed operations [*Gilman et al.*, 2013; *Pétron et al.*, 2012; *Pétron et al.*, 2014]. The complex meteorology of the region often facilitates mixing of sources [*May and Wilczak*, 1993; *Reddy and Pfister*, 2016; *Vu et al.*, 2016]. We examine $RONO_2$ branching ratios inferred from $NO_y$ and $O_3$ observations, and calculated from VOC observations. Using previously published positive matrix factorization (PMF) source factors we provide insight into the fate of $NO_x$ and the consequences of shifting VOC sources on $O_3$ chemistry [*A Abeleira et al.*, 2017; *A J Abeleira and Farmer*, 2017].

**Methods**

*Field Site Description*

We present observations collected over the spring and summer of 2015. The spring campaign was conducted between 18 March and 18 May and the summer campaign ran from 28 June and 7 September 2015 at BAO (40.05°N, 105.01°W, 1584 m above sea level). BAO is ~35 km north of Denver, ~25 km east of Boulder (and the foothills of the Rocky Mountains), and <3 km west of Interstate-25, at the southeastern corner of the Wattenberg Gas Field [*A Abeleira et al.*, 2017; *Kaimal and Gaynor*, 1983]. The site has a 300 m tower with meteorological measurements of temperature, relative humidity, wind speed and direction at 10 m, 100 m, and 300 m. Trace gas instruments were located in two trailers at the base of the tower. The spring campaign hourly average temperatures ranged from 6-15 °C with an hourly standard deviation of about 6 °C. Summertime temperatures were warmer and ranged from 16-30 °C with campaign hourly standard deviations of less than 4 °C. Both campaigns observed thermally driven upslope winds from the

southeast occurred during the day until evening and into the night when the wind shift to a southwesterly downslope. Significant variability in wind direction is observed during both campaigns (Figure 1.8).

*Measurements*

The measurement techniques, inlet and sampling specifications, uncertainties, and LODs of each measurement used in this paper are summarized in Table 1.

$O_3$ was measured by a commercial UV (254 nm) photometric absorption analyzer (2B Technologies Inc. Model 202 Ozone Monitor), calibrated from 0-400 ppb using a NIST-traceable ozone calibration source (2B Technologies, Inc., Model 306 Ozone Calibrator).

NO, $NO_2$, and $NO_y$ were measured using a single-channel commercial analyzer (Teledyne Model 200EU) employing NO-$O_3$ chemiluminescence detection. The NO detector was operated in tandem with two commercially-available converters: (1) a molybdenum converter (Thermo Scientific Inc.) heated to 320 °C for reduction of $NO_y$ species to NO, and (2) a 395 nm LED converter (Air Quality Designs, Inc., Blue Light Converter) for photolysis of $NO_2$ to NO. Both converters were positioned as close as possible to the inlet tip (~25 cm downstream). A 7 μm stainless steel filter (Swagelok) was positioned immediately downstream of the molybdenum converter; no other filters were used. A solenoid valve switched the analyzer from sampling from the molybdenum ($NO_y$) converter or the LED ($NO_x$) converter every 10 s; the LEDs in the blue light converter were switched on (to measure NO+$NO_{2,converted}$) and off (to measure NO only) every minute. $NO_2$ was determined by subtracting 1-min averaged NO from the subsequent minute 1-min averaged NO+$NO_{2,converted}$ divided by the conversion efficiency (fraction of $NO_2$ photolyzed to NO). $NO_y$ measurements were collected every other 10 s and averaged to 2 min to be reported on the same time-base as NO and $NO_2$. The analyzer was calibrated daily to a known mixing ratio

**Table 1.1**: Summary of trace gas measurements used in this analysis.

| Measurement | Detection method (Detector make/model for commercial units) | Inlet configuration[a] | Sample line configuration[b] | Residence time[c] (s) | | Sampling and averaging rates | LOD[d] (pptv) | Uncertainty (%) |
|---|---|---|---|---|---|---|---|---|
| $O_3$ | UV absorption (2B Technologies, model 202) | 5 um PTFE particulate filter positioned at the inlet tip | 1 LPM flow rate; 9 m of ¼" o.d. PFA tubing | 5 | | 6 samples per min, final data average to 1 min | 3000 | 5 |
| NO, $NO_2$ | NO-$O_3$ Chemiluminescence (Teledyne, model 200E) | 395 nm LED converter positioned 25 cm downstream of the inlet tip; LEDs on for NO+$NO_2$ measure, LEDs off for NO measure | 1 LPM flow rate; ~10 m of ¼" o.d. PFA tubing | 5 | 10 | 6 samples per min, LEDs switched on/off every 1 min, final data averaged to 2 mins | 50 | 5 for NO; 7 for NO2 |
| $NO_y$ | NO-$O_3$ Chemiluminescence (Teledyne, model 200E) | Mo converter heated to 320 °C and positioned 25 cm downstream of the inlet tip; a 7 µm stainless steel particulate was positioned in line just downstream of the converter | 1 LPM flow rate; ~10 m of ¼" o.d. PFA tubing | 5 | 10 | 6 samples per min, final data averaged to 2 mins | 50 | 20 |
| PAN/PPN *Flocke et al*., [2005] | Dual channel GC-ECD | 1 um PTFE particulate filter positioned at the inlet tip; 7 LPM pumped bypass flow through 7.3 m of 1/2" o.d. PFA tubing | 0.05 LPM sample flow picked-off inlet bypass flow through ¼" o.d. PFA tubing to detector | 1 | 120 | 1 chromatogram collected every 5 mins | 2 | 16 |
| $HNO_3$ *Ellis et al.*, [2010]; *McManus et al.*, [2011]; *Roscioli et al.*, [2016] | Dual quantum cascade laser spectrometry (Aerodyne, dual-TILDAS) | Inertial inlet actively passivated with nonafluorobutane sulfonic acid | | <1 | | 1 sec sampling rate, final data averaged to 1 min | 70 | 25 |
| VOCs *Sive et al.*, [2005]; *Zhou et al.*, [2005, 2008]; *Abeleira et al.,* [2017] | GC-(FID & ECD) (Shimadzu, GC-17A) | 1 um PTFE particulate filter positioned at the inlet tip | 0.2 LPM flow rate; ~9 m of ¼" o.d. PFA tubing | N/A | | 1 chromatogram collected every ~40 mins | NMHCs: 2-23 $C_1$-$C_2$ halocarbons: <1-6 ANs: 0.2-0.5 OVOCs: 60-100 | 0.6 – 10 depending on the VOC species |

of NO via standard addition of a NIST traceable 5 ppmv NO in $N_2$ standard (Scott-Marrin) into a flow of synthetic ultrapure zero air (UZA). The conversion efficiencies of the LED ($NO_x$) and molybdenum ($NO_y$) converters were calibrated using a known concentration of $NO_2$ generated by gas phase titration of the NO standard. The $NO_y$ channel was also challenged daily with $HNO_3$ generated from a permeation tube (Kintek, 30.5 ± 0.8 ng/min at 40 ºC). Conversion efficiencies were 90 ± 10-15% for $NO_y$ and consistently 93% for $NO_2$.

Nitric acid ($HNO_3$) measurements were collected at 10 Hz with a dual quantum cascade laser spectrometer (Aerodyne Research Inc.) at the 1722 $cm^{-1}$ absorption feature [*McManus et al.*, 2011]. A prototype 50 cm astigmatic multipass absorption cell (AMAC; 400 m path length) was used for increased sensitivity during the first month of the campaign, after which it was replaced by a 50 cm AMAC (157 m path length). An active passivation inlet using continuous injection of nonafluorobutane sulfonic acid (10-100 ppb) was employed to maintain a response time of 0.75 s [*Roscioli et al.*, 2016]. The inlet (~2 m from primary inlet) was followed by a heated, fused silica inertial separator to remove particles >300 nm from the sample stream [*Ellis et al.*, 2010]. Hourly calibrations (5 ppb $HNO_3$ from a permeation tube) were injected at the inlet tip.

Peroxyacetyl nitrate (PAN) and peroxypropionyl nitrate (PPN) were measured using the dual channel National Center for Atmospheric Research (NCAR) gas chromatograph with a common sample loop, two columns and ovens, and an electron capture detector (GC-ECD) [*Flocke et al.*, 2005]. For this work, the NCAR PAN GC pulled ambient air continuously through a1.5 mL sample loop. A plug of air was injected onto alternating columns for separation every 5 minutes. Both columns alternatively fed a single ECD, and this sequence of sampling within the NCAR PAN GC was controlled by five different multiport valves. Thus, the PAN measurement represents a point sample on a 5 minute interval, rather than a 5 minute average. The system was calibrated

for PAN every 4 hrs, alternating ovens (i.e. separation columns) for each calibration period. PAN was generated by photolyzing acetone (254 nm Jelight Lamp; 20 ppmv acetone in UZA (Scott-Marrin)) in the presence of $O_2$ and an accurately measured flow of NO (1 ppmv NO in $N_2$, Scott-Marrin) [*Warneck and Zerbach*, 1992].

Thorough measurement descriptions are presented in detail in the literature the non-methane volatile organic compounds (NMVOCs) measurements in detail [*A Abeleira et al.*, 2017]. Briefly, 46 NMVOCs including $C_2$-$C_8$ non-methane hydrocarbons (NMHCs), $C_1$-$C_2$ halocarbons, $C_1$-$C_5$ alkyl nitrates (ANs, the sum of these species is denoted as ΣANs = methyl + ethyl + 1-propyl + 2-propyl + 2-butyl + 2-pentyl + 3-pentyl nitrate), and a few oxygenated volatile organic compounds (OVOCs) were measured in 5 min integrated samples on a sub-hourly time basis with a 4-channel custom cryogen free online gas chromatography system [*Sive et al.*, 2005; *Zhou et al.*, 2008; *Zhou et al.*, 2005]. Response factors of NMHCs, halocarbons, OVOCs, and ΣANs were determined every 8-10 hours from a whole air calibration standard (Cyl-S; D. Blake, UC Irvine). Precision ranged from 0.6% - 10%, depending on the VOC.

For clarity, we define the following terms. $\Sigma NO_y$ as the sum of individual measured components: NO + $NO_2$ + PAN + PPN + $HNO_3$ + ΣANs, whereas $NO_y$ refers to the direct $NO_y$ measurement through the heated molybdenum converter. $\Sigma NO_z$ refers to the sum of measured oxidized nitrogen species ($HNO_3$, PAN, PPN, and ΣANs), where as $NO_z$ refers to an $NO_y$ species that is not $NO_x$. $NO_z$ mixing ratios are computed as $NO_y$-$NO_x$. Additionally, ΣANs refers to the sum of the speciated measurements collected at BAO (methyl, ethyl, 1-propyl, 2-propyl, 2-butyl, 2-pentyl, 3-pentyl nitrate). ANs is the generic term describing all organic nitrates.

*Data Treatment*

All data are presented in local time (Mountain Daylight Time – MDT) and were collected between 18 March and 18 May 2015 (spring campaign), and 28 June and 7 September 2015 (summer campaign). The summer campaign data are segregated into periods where the local atmosphere was influenced by aged wildfire smoke transported from fires in the Pacific Northwest, denoted as 'smoke-impacted'.[*Lindaas et al.*, 2017] Periods that are not influenced by aged wildfire smoke are referred to as 'smoke-free'. The temporal resolution of measured VOCs is approximately one hour, PAN and PPN have a temporal resolution of five minutes, and the remaining trace gases are gridded to one minute. The VOCs are analyzed on their native time basis and not gridded to the one minute resolution of all other species.

A portion of this analysis uses source apportionment factors generated from a positive matrix factorization (PMF) analysis [*A Abeleira et al.*, 2017]. PMF is a source apportionment technique that has the ability to separate groups of species with co-varying ambient mixing ratios from other species that exhibit different temporal variability, and the groupings are referred to as factors that co-vary simultaneously [*Ulbrich et al.*, 2009]. These factors can represent direct sources, photochemically produced species, chemical processes affecting those species, or transport processes. These are presented for the spring and smoke-free periods, the PMF analysis was restricted to periods of time without the influence of aged wildfire smoke.

*Positive Matrix Factorization Source Factors*

The VOC mixture observed at BAO represents an urban site with significant contributions from oil and natural gas operations [*A Abeleira et al.*, 2017]. In other urban regions VOC reactivity is typically dominated by alkenes, aromatics and alkynes from traffic emissions or industrial processes. This is not the case for the NFRMA: observations at BAO suggest traffic-related VOCs contribute <15% of the reactivity on average, and oil and natural gas activity dominate the

anthropogenic VOC reactivity [*A Abeleira et al.*, 2017]. In addition, the absolute magnitude of the reactivity contributed by isoprene is much lower than other biogenically-influenced urban sites, though isoprene can make a substantial relative contribution to VOC reactivity during select summer afternoons (up to 49% in 2015) [*A Abeleira et al.*, 2017].

*Zero-Dimensional Box Modelling*

We use the F0AM Box Model with the following approach to address several fundamental questions regarding the chemistry occurring at BAO [*Wolfe et al.*, 2016]. In doing so, we employ two distinct approaches to understand the chemical composition of unmeasured and measured compounds.

(1) We run an observationally constrained model to estimate mixing ratios of unmeasured compounds and understand the chemical lifetimes of measured and unmeasured species based on model outputs. This model is run for five days with a turnover time of 24 hrs to prevent buildup of compounds with long chemical lifetimes, no background mixing ratios were applied so the 24 hr turnover time represents a first order loss process for all compounds except those that were constrained. We refer to this approach as the 'constrained' case.

(2) To understand how particular chemical mixtures impact ozone and the $NO_z$ budget we follow a slightly different approach. We constrain the particular mixture we are testing and run the model in the same manner as the 'constrained' case and to allow a diel steady state to be achieved ~5 days. Following this 'spin-up', test species ($O_3$, $HNO_3$, PAN, PPN, 2-butyl nitrate, and 2-propyl nitrate) are unconstrained starting at 8AM. All measured species that are constrained in the spin-up remain constrained. Midnight mixing ratios of all other modeled species represent background mixing-ratios except ozone which uses a higher

value consistent with previous literature.[*McDuffie et al.*, 2016] The turnover time was systematically varied to minimize the relative deviations compared to observations for the test species (Figure 1.9). Error reached a minimum at 2.5 and 2 hrs for spring and summer models respectively. We refer to this approach as the 'unconstrained' case and is used to understand the role of particular PMF factors and varying the VOC and $NO_x$ loads.

**$NO_y$ Budget**

*Observed Nitrogen Oxide Species*

Over the three distinct measurements periods presented here, there is generally little variability between spring, summer smoke-free, and summer smoke-impacted periods for the reactive nitrogen oxides measured ($\Sigma NO_y$). A campaign overview of these species is presented in Figure 1 and a summary table of relative changes in concentration is in the supplemental (Table 5 & 6). The impact of smoke on $NO_y$ and $O_3$ is discussed in more detail by Lindaas et al REF. Daytime observations show a slight elevation of $NO_y$, NO, and $NO_2$ species during the spring and summer smoke-impacted periods relative to summer smoke-free data. Other secondary species do not show this variability in the spring, but during the summer smoke-impacted data PAN and PPN show substantial daytime enhancements. Nighttime trends generally follow the daytime, except for the summer smoke-impacted period where concentrations of all $NO_y$ species are enhanced.

The BAO measurement site was at the intersection of multiple emission sources including traffic, urban and suburban land-use, agriculture, oil and natural gas, and plants. In addition, the region is subject to distinct meteorological patterns. Direct comparisons to BAO are lacking and thus we present observational similarities as context. In general, measurements of primary emissions are less than those observed in urban cores such as Houston, Denver, or Los Angeles, but greater than those in suburban or biogenic environments (e.g. Granite Bay or Blodgett Forest

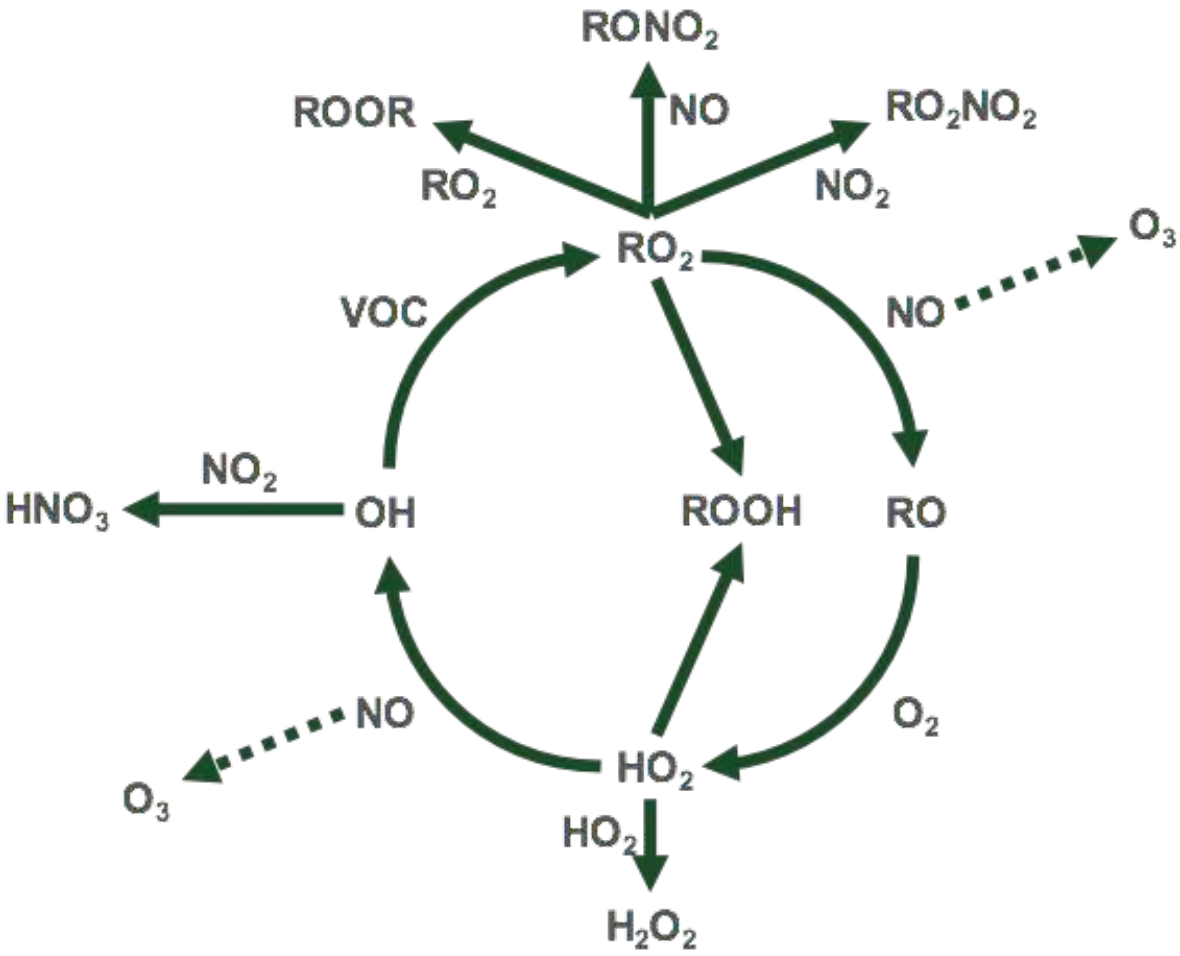


**Figure 1.1**: Schematic of the HOx cycle with shunts to the NOx cycle and ozone production shown as a dashed line.

Research Station). $NO_z$ constituents ($HNO_3$, PAN, PPN, ANs) have similar diel trends and magnitudes as observations from Granite Bay [*Douglas A. Day*, 2003; *D. A. Day et al.*, 2009; *Luke et al.*, 2010; *Murphy et al.*, 2006; *Murphy et al.*, 2007; *Pollack et al.*, 2013]. Observed VOCs show a region with a biogenic influence, but of differing magnitude when compared to Atlanta or St. Louis [*Millet et al.*, 2016; *S. Sillman et al.*, 1997]. Similarly, the dominance of oil and natural gas production and refining observed in the Houston area is of a more substantial scale than observed at BAO. The lack of direct comparisons highlights some of the challenge in determining the driving factors of secondary pollutants.

The diel behavior of $NO_y$ is influenced by regional traffic patterns and photochemistry. $NO_y$ magnitudes are driven by $NO_x$ mixing ratios and invariant nocturnal behavior for the three measurement periods. Overnight mixing ratios are ~ 5 ppb followed by a rapid rise in the morning driven by a rapid injection of $NO_x$ when $NO_x$ to $NO_y$ ratios approach unity. This daily injection of $NO_x$ is associated with traffic patterns in the region. Following this injection, the $NO_y$ budget decreases in magnitude due to a decrease of primary emissions and dilution from boundary layer expansion. During this decrease, $NO_y$ becomes dominated by $NO_z$. Speciated $NO_z$ measurements ($HNO_3$, PAN, PPN, ANs) show a clear photochemically driven diurnal cycle. In the evening the $NO_y$ budget shifts back to a $NO_x$ driven system associated with an evening traffic pattern.

Campaign measurements of the sum of measured alkyl nitrates are shown in Figure 2. ΣANs are dominated by contributions from 2-butyl nitrate (~35%) and 2-propyl nitrate (~25%) with 2-pentyl nitrate and 3-pentyl nitrate contributing ~10% each. Remaining alkyl nitrates contribute a minor fraction. These compounds have been associated with oil and natural gas operations [*A Abeleira et al.*, 2018]. Photochemical production of these compounds is observed across the suite of measured compounds and is especially distinct in the summer where

photochemistry occurs more rapidly than during the spring (Figure 1.11). Nocturnal concentrations of measured organic nitrates are persistently higher in the spring and smoke-impacted periods than during smoke-free periods of summer. While ΣANs contributes less than 5% at most to the total $NO_y$ budget, they are an important sink of $RO_2$ radicals that is dependent on the VOC composition present.

*Observed Nitrogen Oxide Budget Deficit*

Oxidized nitrogen species are often referred to as $NO_z$ and indicate the degree of atmospheric processing that has occurred. Comparing the measured suite of oxidized nitrogen compounds ($\Sigma NO_z$) to $NO_z$ allows us to estimate how much of the oxidize nitrogen budget that has been measured (Figure 3). During the spring, the $\Sigma NO_z$ constituents do not close the budget with a magnitude that is beyond the propagated uncertainty of the $NO_z - \Sigma NO_z$ difference. However, $HNO_3$ was not measured and is a key unobserved component that would likely close – or more nearly close – the budget. We restrict our discussion of the observational NOz budget to summer when $HNO_3$ was measured. The $NO_y$ budget is closed by summed measurements of individual components (NO, $NO_2$, ΣANs, PAN, PPN, $HNO_3$) beyond propagated uncertainty during the bulk of the summer. However, a budget discrepancy beyond uncertainty occurs during about a fifth of both smoke-impacted and smoke-free periods (N=70/392 = 18% of smoke-impacted and N=50/246 = 20% of smoke-free periods). The observed budget deficit generally follows photochemically driven diel cycle and typically peaks at ~1 ppb and up to 2 ppb at times. The budget deficit (i.e. $NO_y - \Sigma NO_y$) has been commonly referred to as 'missing' $NO_y$ and is often attributed to large or multifunctional organic nitrates species [*Douglas A. Day*, 2003; *Fahey et al.*, 1986; *Ridley*, 1991; *Shepson et al.*, 1993].

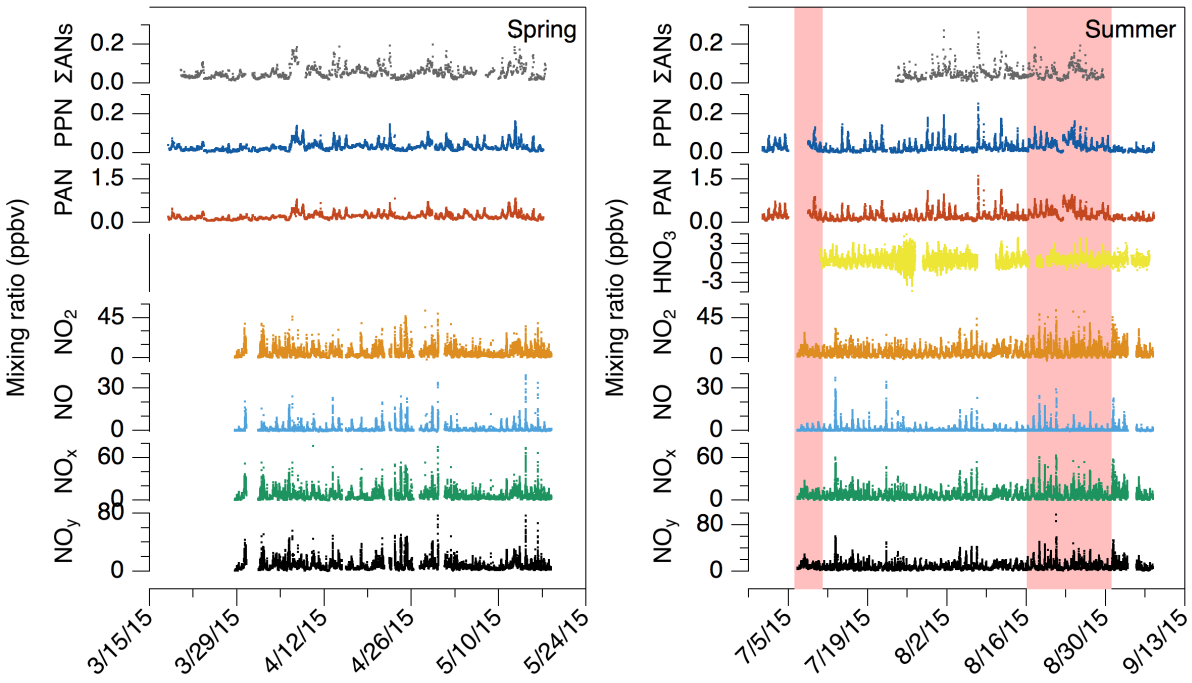


**Figure 1.2**: Spring and summer campaign overview of the $NO_y$ budget. Summer smoke-impacted periods are shown as a red swath through impacted dates.

However, at BAO the $NO_y$ instrument was deployed without a particle filter to minimize losses of nitric acid. Particulate ammonium nitrate ($NH_4NO_3$) can thus contribute to the $NO_y$ measurements and account for at least some of the observed 'missing' $NO_y$ [*Fahey et al.*, 1986]. Particulate nitrate was measured from the C-130 aircraft during the FRAPPE campaign, showing that high particulate $NO_3^-$ occurs in the region during cyclonic events [*Vu et al.*, 2016]. Wind sectors associated with agricultural operations, higher relative humidity, and lower temperatures are associated with slight enhancements of 'missing' $NO_y$ and these factors are known to favor particulate nitrate formation. The ensemble of evidence indicates that this is a likely cause of at least some of the observed 'missing' $NO_y$.

Unmeasured organic nitrates and particulate nitrate are not the only possible reasons for the observed missing $NO_y$. Below, we consider instrument interferences from non-$NO_y$ species and contributions from other un-measured $NO_y$ species. $NO_y$ measurements employing a heated molybdenum converter may be subject to potential interferences with non-$NO_y$ species, like gas-phase ammonia ($NH_3$) and hydrogen cyanide (HCN) or aerosol components such as particulate ammonium nitrate [*Fahey et al.*, 1986; *Williams et al.*, 1998]. Agricultural operations lie within 30 km of the BAO site, and thus provide a source of $NH_3$ (~15 ppb median daily maximum occurring in the late-morning from ground-based measurements at the BAO site during the FRAPPE campaign in summer 2014) in the local area [*Tevlin et al.*, 2017]. However, molybdenum converters heated to roughly 320 ºC convert negligible amounts of $NH_3$ and HCN in a dry air sample [*Fehsenfeld et al.*, 1987; *Nunnermacker*, 1990]. Thus, $NH_3$ and HCN should contribute minimally to the observed 'missing $NO_y$'. Similarly, $N_2O_5$, HONO, $ClNO_2$, and $NO_3$ tend to only be present in large abundances at night when photolysis is minimal, and are thus likely only minor

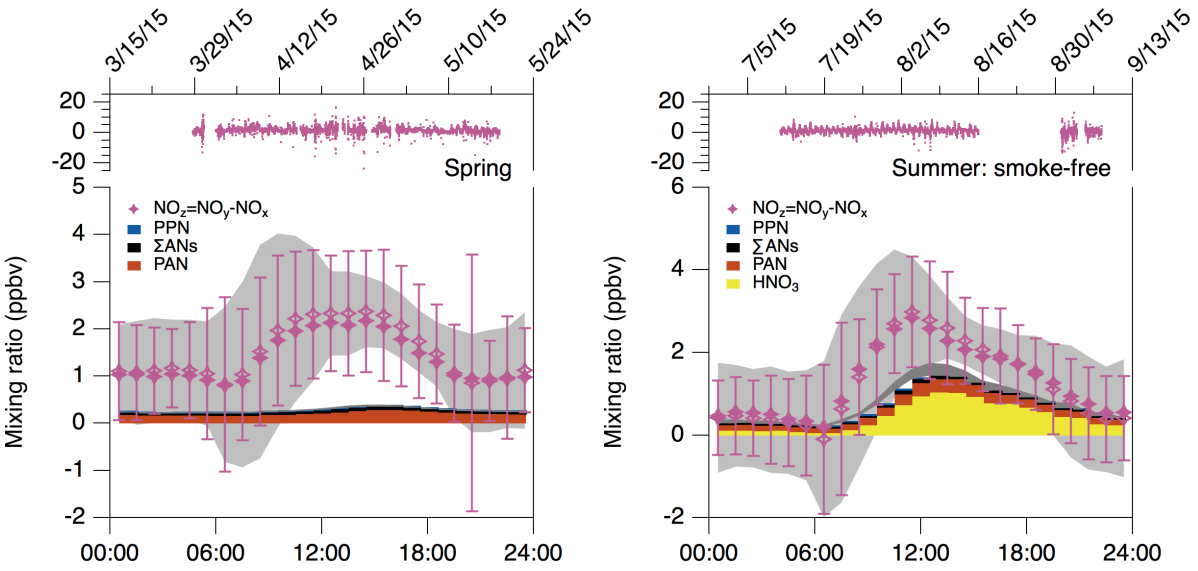


**Figure 1.3**: NOz budget deficit. Grey bands indicate propagated NOz error. Open symbols are averages with closed symbols as medians.

fractions of daytime 'missing $NO_y$' [*Kim et al.*, 2014; *Wagner et al.*, 2013; *Wild et al.*, 2016; *Wood et al.*, 2009]. No measurements of these species were made at BAO during the 2015 campaign, but previous campaigns at BAO suggest daytime mixing ratios of $N_2O_5$ <30 ppt (FRAPPE 2014, carriage measurements), $ClNO_2$ <50 ppt, and HONO <200 ppt [*S. S. Brown et al.*, 2007; *Kim et al.*, 2014; *Thornton et al.*, 2010]. Methacryloyl peroxynitrate, or MPAN, is photochemically produced and contributes to $NO_y$, but is typically a small fraction relative to PAN; in summer 2014 at BAO, MPAN/PAN ratios averaged <0.05 [*Zaragoza et al.*, 2017].

Organic nitrates have been previously measured and are known to contribute substantially to the $NO_y$ budget in many urban and suburban environments. While the GC measurements at BAO capture a wide range of VOCs, most large (> $C_8$), oxygenated, and multifunctional organic molecules do not make it through the instrument's GC columns, or are present at concentrations < LOD. Similarly, observing multifunctional or > $C_5$ ANs is challenging. While individual organic nitrate isomers may have low mixing ratios, the sum of these species can be a substantial fraction of the $NO_y$ budget (e.g. up to 28% reported at Granite Bay) [*Cleary et al.*, 2007; *Rosen*, 2004]. To more thoroughly investigate the potential contribution of organic nitrates to the $NO_y$ budget at BAO, we use the F0AM box model.

*Modeling the $NO_z$ Budget*

Here, we use a constrained zero-dimensional box model to investigate species that were not measured and could contribute to the $NO_y$ budget. Figure 4 provides an overview of the modelling results.

*Spring $NO_z$*

Measurements of the spring $NO_z$ budget notably lacked a nitric acid measurement, which modelling outputs suggest is the dominant $NO_x$ sink throughout the day. Generally, the modeled

$\Sigma NO_z$ and measured $NO_z$ (=$NO_y$-$NO_x$) agree within the standard deviation of the measurements. However, in the evening, the modeled $NO_z$ maximize later than the measurements. At least some of this disagreement may be due to underestimated dry deposition in the model. Dry deposition is parameterized relative to the boundary layer height, which is fixed throughout the model run and thus does not describe the separation of the nocturnal boundary layer and residual layer that occurs around sunset. With a much shallower boundary layer height in the evening and at night, depositional losses are substantially enhanced at night and should suppress the nitric acid.

Peroxy nitrates are a substantial fraction of the modeled $NO_z$ budget, with PAN and PPN accounting for 75% of the modeled peroxy nitrates. The remaining quarter peroxy nitrates are nearly all associated with oil and natural gas emission factors. Comparing the modeled production and loss rates of these compounds, we find that the chemical lifetimes of these peroxy nitrates as a class of compounds are <4 hours during the day, making them a temporary reservoir species that can efficiently export $NO_x$ and $HO_x$ radicals to other locations within the region on short time scales.

Organic nitrates in the springtime do not represent a substantial fraction of the modeled $NO_z$ budget. The formation of these compounds is driven almost entirely by oil and natural gas emissions and are thus well-captured by the ΣANs measurements. The modeled chemical lifetimes of the short-chain alkyl nitrates associated with oil and natural gas VOCs exceed the turnover time (24 hrs) of the model, suggesting that the measured ANs are mostly lost to dilution and do not recycle $NO_x$ and $HO_x$ within the NFRMA [*A Abeleira et al.*, 2018]. Photolysis occurs on longer time scales, making these molecules a local sink for $NO_x$ – but a potential reservoir species for transport of ozone precursors on regional and global scales.

*Summer $NO_z$*

The $NO_z$ budget during the summer is more evenly split across nitric acid, organic nitrates, and peroxy nitrates. The model output and measurement $NO_z$ agree well throughout much of the day. Similar to spring comparisons, slight model-measurement disagreement occurs in the late-evening. The model captures the $HNO_3$ diel cycle well, suggesting that depositional losses for organic nitrates are underestimated with respect to the fixed boundary layer parameterizations.

Peroxy nitrates are quite similar in the spring and summer, and are dominated by PAN and other compounds associated with oil and natural gas emissions. In contrast to spring, the model predicts MPAN production from biogenic precursors, although at low levels (10-20 pptv). Modeled peroxy nitrate lifetimes in the spring are typically longer than in summertime, 5 hrs compared to <1 hr and suggests that peroxy nitrates are more effective reservoirs to transport $NO_x$ out of the region in the spring. PAN follows a similar trend, if slightly exaggerated with spring to summer lifetimes of ~15 hrs vs ~2 hrs relative to peroxy nitrates.

The model predicts that secondary organic nitrates are a substantial fraction of the $NO_z$ budget, with comparable concentrations to nitric acid. Oil and natural gas emission oxidation products account for 20% of the total modeled organic nitrates. The bulk of the modeled organic nitrates are isoprene oxidation products. We note that isoprene-derived organic nitrates originate from both daytime OH and nighttime $NO_3$ chemistry. The lifetimes of these species in the model are longer than for peroxy nitrates, but are still predicted to be relatively short (<12 hrs on average). The model thus suggests that organic nitrates are not an effective $NO_x$ sink and are capable of transporting $NO_x$ locally or even to areas outside the NFRMA – but this ignores the likely partitioning of multifunctional organic nitrates to the particle phase, which can lengthen their lifetime in the atmosphere and potential for permanent removal from the atmosphere by wet or dry deposition. However, the model is limited by the available VOC data, and highlights the need for

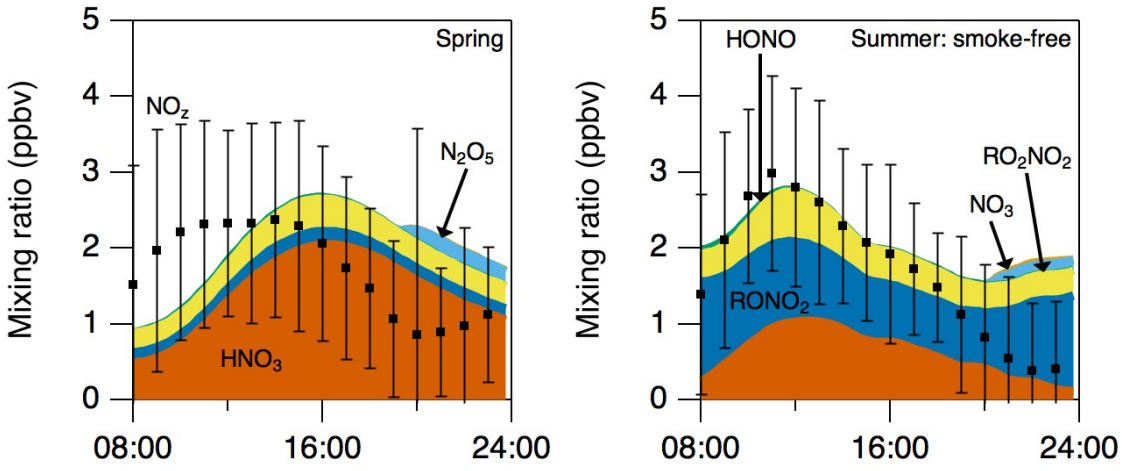


**Figure 1.4**: Model outputs from a constrained model run for spring and summer: smoke free periods. Black square are observations with standard deviation of observations shown.

more comprehensive VOC measurements in the NFRMA. Overall, the model results from the summer suggest that large and/or multifunctional organic nitrates represent a substantial fraction (15%) of the $NO_y$ budget, and may account for some of the missing $NO_y$ that is observed during the summer campaign. The model is not limited to providing insight on $NO_y$ partitioning at BAO. $NO_z$ species represent chain termination steps for the $HO_x$-$NO_x$ cycle, and their production inherently suppresses $O_3$ production. Below we investigate the link between the BAO VOC budget, $NO_z$ budget and $O_3$ production.

**Ozone**

*Modeling Perturbations to Ozone*

Ozone isopleths are a classic depiction of the non-linear behavior of ozone production. Isopleths are typically presented for a single time period to use for interpretation around a given VOC mixture and $NO_x$ loading. Lines indicate constant ozone (or ozone production) for different VOC loads and $NO_x$ loads. For the observations collected in the spring and summer of 2015 at the BAO site, we employed a spun-up model and subsequently unconstrained 16 hrs to understand how a perturbed NMVOC and/or $NO_x$ loading impacts ozone relative to the average day. These ozone-mosaics (Figure 5) suggest that there is a changing environment throughout the day surrounding ozone production and that the isopleth is dynamic as it depends on the NMVOC mixture, which changes throughout the day.

Ozone sensitivity to $NO_x$ and VOC loading change over the course of the day in different ways between spring and summer. Figure 1.5 shows a base case run and eight different VOC and $NO_x$ loadings. In the spring, which has negligible biogenic influence and a slightly different oil and gas signature due to suppressed photochemistry, the model suggests that the VOC mixture at BAO results in a $NO_x$-saturated system that is moving towards peak ozone over the course of the

day. In the summer, the $NO_x$ and NMVOC mixture produce a system in which ozone production is maximized, and the system shifts towards $NO_x$-limited as the day progresses. These differences might initially appear to be due to the higher summer NMVOC reactivity. Even equivalent (in reactivity) concentrations of different NMVOC precursors result in different ozone production rates [*Lindaas et al.*, 2019]. suggested that the hydrocarbons associated with ONG were more efficient at producing ozone than isoprene. Here, we pursue this analysis from an ozone isopleth perspective to investigate how changing VOC concentrations in the NFRMA can influence the $NO_x$ sensitivity of an air mass. These isopleths provide a useful tool to understand when the chemical environment is most sensitive to $NO_x$ changes. Below, we show how the NMVOCs used to constrain the model conditions are a strong lever on not only ozone production, but also the $NO_x$ sensitivity of ozone production.

Observed springtime NMVOCs have only a weak influence on ozone (Figure 1.6), with the bulk of the ozone profile being driven by background ozone and boundary layer dynamics. That is, providing the model with background ozone (38 ppb, consistent with literature precedents (e.g. [*McDuffie et al.*, 2016]) above the nocturnal boundary layer, and allowing it to mix in to the boundary layer and evolve throughout the day accounts for much of the average spring diel ozone pattern. We attribute this limited effect of NMVOCs on the average spring diel ozone to suppressed photochemistry and lower overall reactivity in the spring relative to the summer. However, considering only the chemical component of ozone production and ignoring the background influence, oil and natural gas associated PMF emission factors contribute ~40% to modeled ozone production. However, we emphasize that this analysis focuses on average diel cycles, and that individual days may have strong chemical influence, and greater or weaker influence from different NMVOC sources.

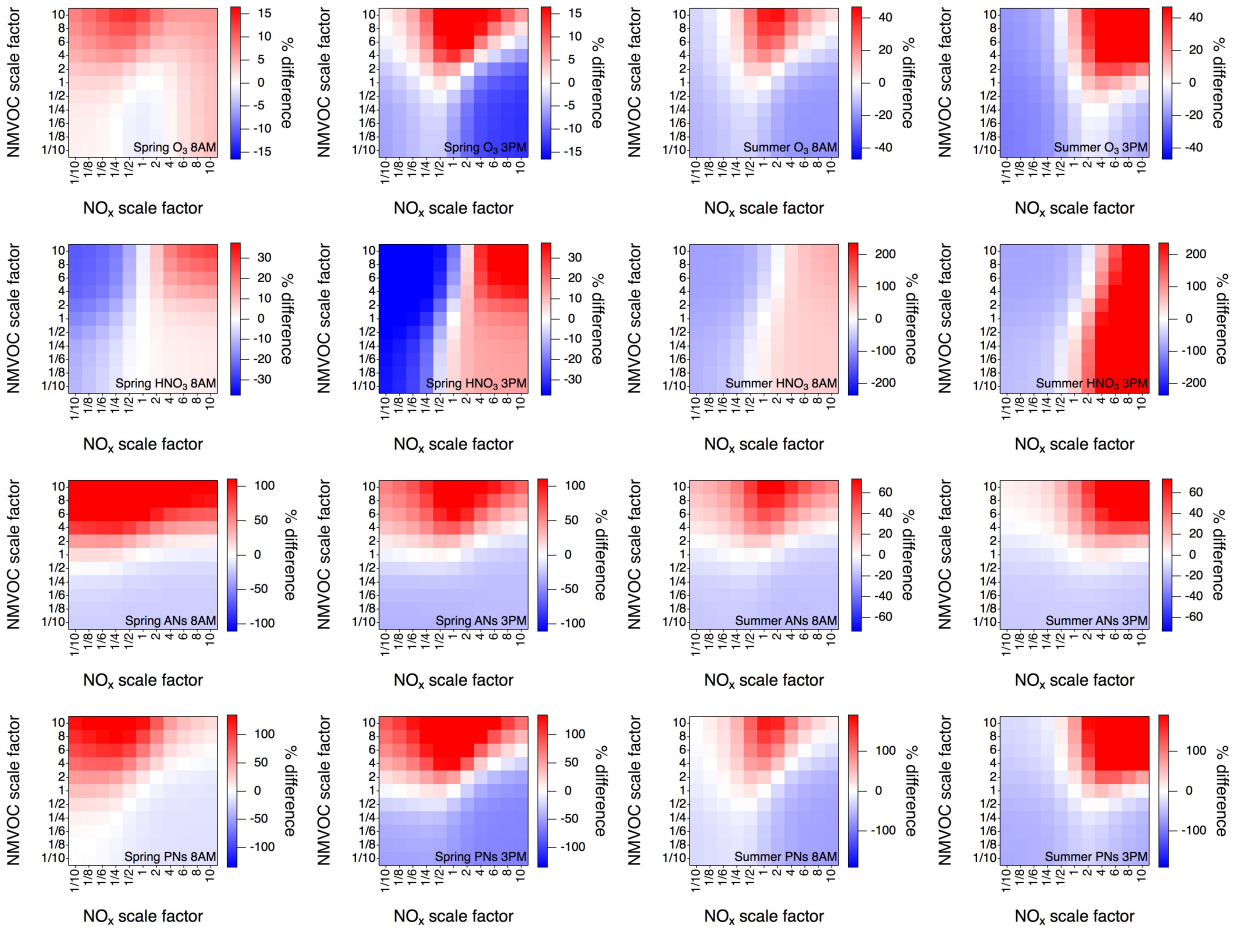


**Figure 1.5**: Isopleth mosaics of $O_3$, $HNO_3$, ANs, and PNs for spring and summer (smoke-free) periods. Both 8AM and 3PM are shown to illustrate the diel sensitivity changes to $NO_x$ and NMVOC loading.

NMVOCs play a powerful role in driving summer time ozone production. Our model suggests that on an average summer day, NMVOCs contribute ~20 ppb to daytime ozone. This initially seems surprising, but the remaining ~40 ppb daytime ozone is driven by background (i.e. pre-existing ozone that is transported to the region, or left over from the night before). The NMVOCs are broken down into six different PMF emission factors. Testing each emission factor individually in our zero-dimensional box model by removing them from the mix and examining the resulting ozone profile suggests that 30% of the chemically produced ozone comes from primary anthropogenic emissions, including oil and natural gas and traffic related emissions. The biogenic emission factor is also a substantial lever on ozone, while the secondary and background emission factors are limited in their impact. The removal of individual anthropogenic factors do not substantially decrease ozone; removing the biogenic NMVOC does cause a more substantial decrease in ozone, but one that is neither controllable (e.g. through anthropogenic activities or policy actions), nor proportional to its reactivity. Average ozone is thus robust with respect to anthropogenic NMVOC sources, and driven by biogenic or other factors that influence background ozone (e.g., transport from other regions). However, we emphasize that this analysis represents base ozone, which does not exceed regulatory levels. Exceedances occur because of other influences such as meteorology, stratospheric intrusion events, or substantial short-term changes in NMVOC or $NO_x$ emissions [*M Lin et al.*, 2015; *Lindaas et al.*, 2019; *Reddy and Pfister*, 2016].

While changing the NMVOCs has little effect on average ozone, changing $NO_x$ can have a dramatic effect. Figure 1.7 explores $NO_x$ impacts on three NMVOC scenarios. Under observed NMVOC conditions, increasing $NO_x$ increases ozone. In contrast, under the same $NO_x$ conditions, the same scale increase of NMVOCs does not substantially increase ozone. However, for increased NMVOC loads, the impact of a decrease is more substantial than for observed NMVOC loads.

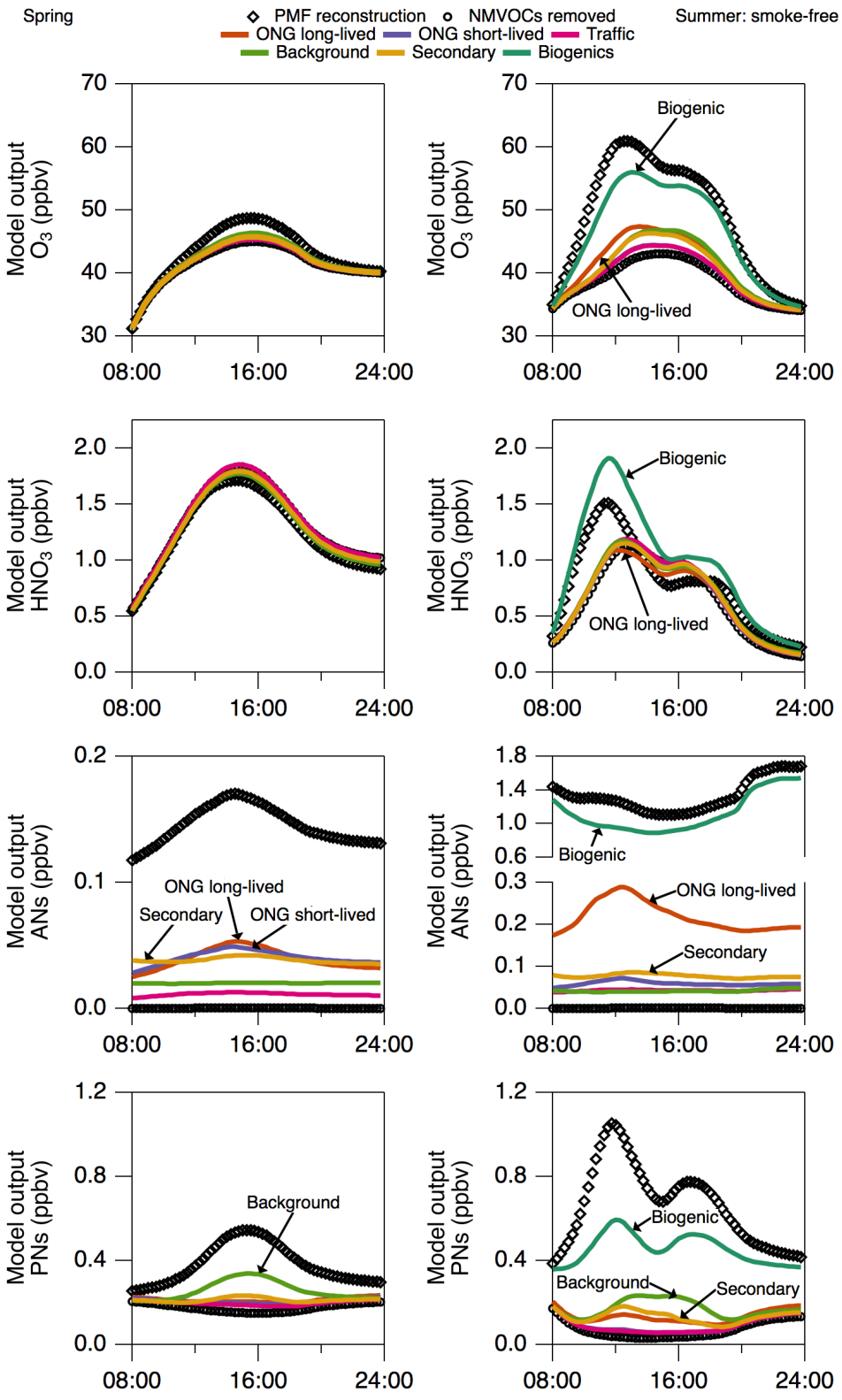


**Figure 1.6**: Diel profiles of $O_3$, $HNO_3$, ANs, and PNs for different PMF source factors along with model runs with the PMF reconstruction and NMVOCs removed.

Modeled decreases in NMVOCs results in a significant lessening of the $NO_x$ sensitivity and efficiently reduces the diel profile of ozone. While these suggest observations are indicative of effective ozone mitigation strategies, the negative impact is that nitric acid may increase under particular scenarios.

This analysis is limited by three components: (1) the reactivity and NMVOC factors are derived only from Abeleira et al.'s observations, and thus ignore the potential contribution from volatile chemical products such as D5-siloxanes and complex solvents, or more complex NMVOCs. *McDonald et al.* [2018] noted that these compounds can contribute substantially to SOA formation in urban environments, and measured siloxanes in Boulder and identified a diurnal pattern similar to traffic related emissions *Coggon et al.* [2018]. Furthermore, emission rates of D5-siloxanes are identified as comparable to benzene emission rates from traffic *Coggon et al.* [2018]. These observations and others have identified compounds that are becoming increasingly important to consider. However, the measurements used herein do include acetone and methyl ethyl ketone, two important volatile chemical products. (2) The measurements were derived from a single year and at a single location. While there have been substantial observations of NMVOCs in the NFRMA, isoprene is rarely quantified and the importance and loading of this compound is not well established. Inter-annual measurement discrepancies are likely due to meteorology and drought effects[*A J Abeleira and Farmer*, 2017]. (3) The model only represents an average smoke-free day under the prescribed conditions. Ozone does not exceed regulatory maxima of 70 ppb over 8 hours on the average day – nor does it on most summer days. This analysis investigates the average day as a thought experiment to investigate the relative importance of NMVOCs on $NO_y$ and ozone – not to provide feedback on individual days. However, Lindaas et al. found that the individual highest ozone days were associated with days of high oil and natural gas NMVOC

factors. These results focus on the average NMVOC mixture, but these model results suggest that substantial perturbations to a single PMF factor or particularly stagnant meteorological conditions will push ozone over the regulatory limit.

**NMVOC Influence on $NO_z$**

*Nitric Acid*

Ozone typically dominate the discussion of NFRMA pollutants, however it is important to consider other chain termination products. Nitric acid is an important precursor to particulate formation [*Womack et al.*, 2019]. Nitric acid is a chain termination step, and is dominantly formed in the troposphere from OH reacting with $NO_2$. Nitric acid has a very long chemical lifetime, but depositional losses substantially shorten the lifetime to less than several days [*Kley et al.*, 1981; *Liu et al.*, 1983; *Liu et al.*, 1987a; *Parrish et al.*, 1986]. Nitric acid is not only a mechanism for $NO_x$ removal from the atmosphere: nitric acid deposition to ecosystems can cause acidification and is a mechanism for nitrogen addition. As nitrogen is typically a limiting nutrient in temperature terrestrial ecosystems, the effects include stream acidification and reduced species richness [*Benedict et al.*, 2013; *Thompson et al.*, 2015]. Rocky Mountain National Park, considered downwind of the NFRMA on 'upslope flow' days, contains particularly sensitive alpine ecosystems with short growing seasons.

Using the same approach of removing individual NMVOC factors from the model as described above for ozone, we find that $NO_x$ and NMVOC impact nitric acid production. Obviously, adding $NO_x$ increases nitric acid production as OH + $NO_2$ is the dominant source of nitric acid. More surprising is the role of NMVOCs in controlling nitric acid production and its sensitivity to NOx. The model suggests that increasing NMVOC decreases nitric acid at current $NO_x$ levels due to suppression of OH. PMF factors have little influence on nitric acid because they

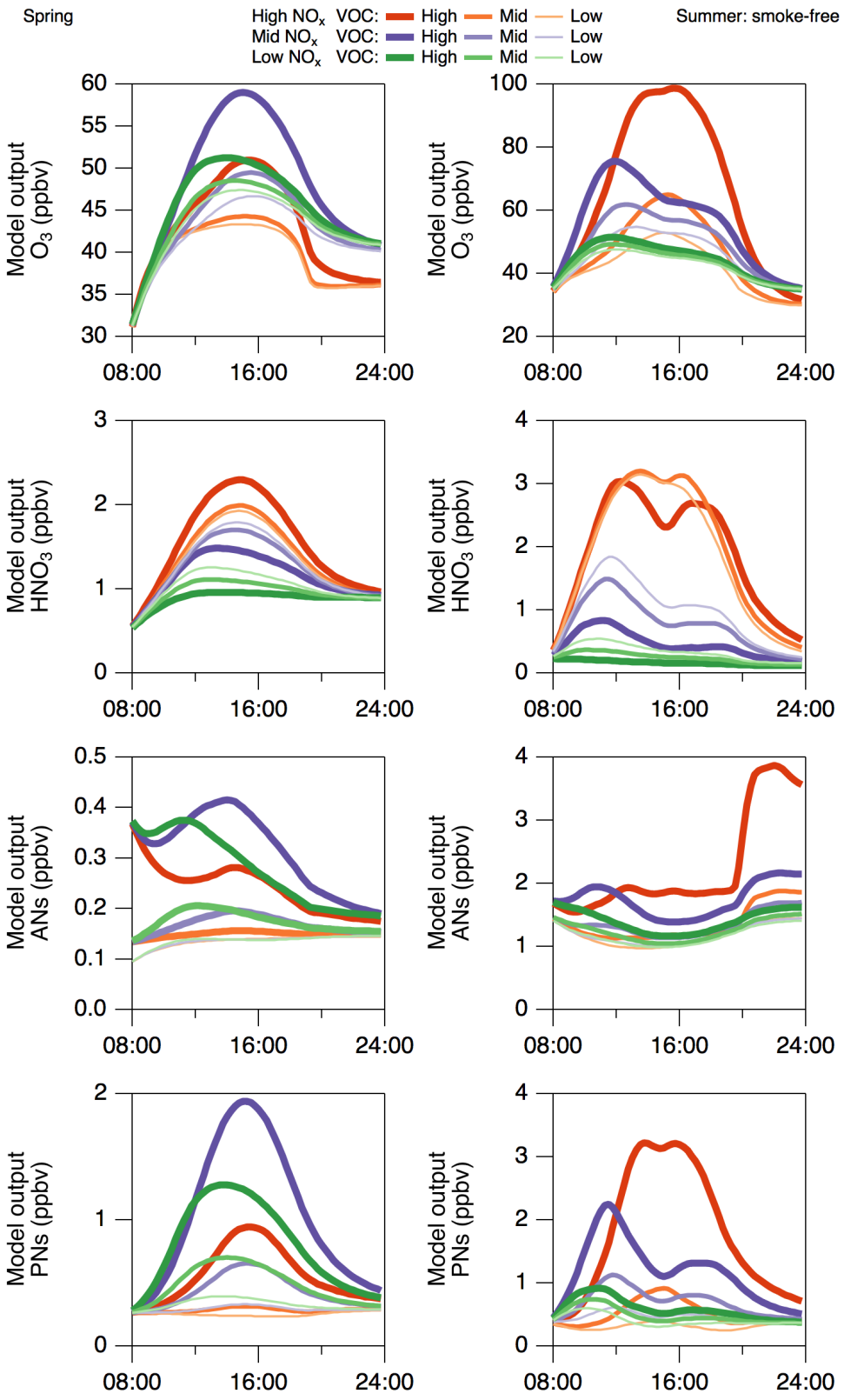


**Figure 1.7**: Diel profiles of $O_3$, $HNO_3$, ANs, and PNs for different NOx and VOC loadings.

do not substantially impact the OH mixing ratios. Nitric acid is not solely dependent on $NO_x$ loading: the NMVOC loading and mixture influences the OH abundance and thus dictates the production of nitric acid.

The modeled nitric acid highlights how VOCs influence $NO_x$ fate through the $HO_x$ cycle – and that coupled nitric acid and $NO_2$ measurements may be useful marker of long-term changes in OH. However, as described above in the *$NO_z$ budget*, organic nitrates are produced through the coupling of the $HO_x$-$NO_x$ cycles through $RO_2$+NO reactions, and the $RONO_2$ chain reaction step is far more sensitive to changes in NMVOCs than $NO_x$.

*The Role of Biogenic Emissions*

The role of biogenic VOCs on ozone in the NFRMA has been contentious. It has been suggested that the role of biogenics is minimal [*Gilman et al.*, 2013]. However, more recent studies have indicated that the role of isoprene is tied to drought conditions in the NFRMA [*A J Abeleira and Farmer*, 2017]. Furthermore, despite the high reactivity, isoprene may not produce as many $RO_2$ radicals as anthropogenic precursors [*Lindaas et al.*, 2019]. This model continually identifies the biogenic PMF emission factor as influencing the $NO_z$ budget and ozone in the summer. The biogenic source factor input to the model has less total OH reactivity than oil and natural gas emission factors, but the diversity of oxidation products results in an overall greater reactivity after model spin up compared with the oil and natural gas emission factors. The diversity of multigenerational oxidation products associated with isoprene drives the high model concentrations of peroxy and organic nitrates. Alone, the biogenic PMF factor constitutes up to 80% of the ozone produced by the observed NMVOCs and enough OH that there is more nitric acid in the biogenic-only model than in any of the other PMF reconstruction model outputs.

While this biogenic factor has a strong influence on modeled ozone and $NO_z$, we do not suggest that they are responsible for air quality concerns. Background ozone always occurs, and exceedances are driven by conditions that elevate this base case ozone above regulatory limits. Biogenic emissions are challenging to change, particularly in the arid environment of the NFRMA. However, drought conditions suppress isoprene, which the model suggests may suppress ozone and organic nitrate production but enhance nitric acid [*A J Abeleira and Farmer*, 2017; *Demetillo et al.*, 2019]. While anthropogenic factors do not drive base ozone or nitric acid, these emission factors contribute to the base ozone – and slight changes in these factors are key drivers for exceedance days that make the NFRMA a non-attainment region.

**Conclusions**

Observations during the summer at BAO indicate a deficit in the $NO_z$ budget. The summer time deficit could be explained by instrument interference from particulate ammonium nitrate and smaller interferences from $NH_3$ and HCN. However, using an observationally constrain zero-dimensional box model, we identify that organic nitrates may make up a substantial fraction of the budget deficit. It is likely that both factors contribute to close the budget and both warrant further investigation to better understand how changing NMVOC mixtures will influence gas-particle partitioning and $PM_{2.5}$.

Using observations and a partially constrained zero-dimensional box model, we demonstrate that NMVOCs influence both ozone and the $NO_z$ budget. Changes to NMVOC and $NO_x$ loading will affect ozone and $NO_z$ sinks: (1) increasing decreasing NMVOC loads will help reduce ozone, but may increase nitric acid, (2) decreasing $NO_x$ will generally reduce all criteria pollutants, but may impact the timing of NMVOC sensitivity. Ozone is sensitive to both NMVOC and $NO_x$ through changes in both the $HO_x$ budget and the subsequent $NO_z$ termination steps.

Additionally, model results suggest that spring and summer ozone have distinct sensitivities to VOC mixture and load, while remaining sensitive to changes in $NO_x$. Spring time ozone is not significantly perturbed by changes to the NMVOCs and no individual PMF source factor has a substantial impact on ozone, while summer time ozone is heavily influenced by the NMVOC budget with oil and natural gas and biogenic factors being key players. We find that anthropogenic PMF factors contribute 30% to the NMVOC driven ozone production in the summer time. More generally for spring and summer, the environment is $NO_x$-limited, but we stress that interpreting ozone as one regime or another is limiting as the sensitivity changes throughout the day from $NO_x$ limited to near peak ozone.

While ozone dominates the conversation in the NFRMA, nitric acid is another key pollutant. These model results also suggest that changes to VOC mixtures and loading will impact nitric acid. Model results suggest that nitric acid is sensitive to NMVOC mixture changes that drive OH mixing ratios. As NMVOC loads decrease, OH availability tends to increase which enhances nitric acid production.

Biogenic emissions play a more important role in summer photochemistry than in spring. The bulk of organic nitrates are isoprene derivatives, but are unlikely to serve as a long-term NOx sink unless they partition to the particle phase. The combined anthropogenic and biogenic summer NMVOC mixture results in higher average daytime ozone than spring, providing an environment near peak ozone in which relatively small increases in NMVOC reactivity or changes in NOx may cause ozone exceedance events.

**Funding Sources, Site Staff, and Data Access**

We acknowledge the National Oceanic and Atmospheric Administration for funding (Award# NA14OAR4310148). We thank Dan Wolfe, Bruce Bartram, and Gerhard Hübler for

support at the BAO site, and Frank Flocke for useful discussions. We also thank Steve Brown and Erin McDuffie for providing $N_2O_5$ data from the 2014 FRAPPE campaign. The data used herein can be found in a repository hosted by the National Oceanic and Atmospheric Administration (http://esrl.noaa.gov/csd/groups/csd7/measurements/2015songnex/).

**Chapter 1: Supplemental Information**

*Model Sensitivity Tests*

Model sensitivity tests were carried out on a variety of parameters to the robustness of our approach. We report the parameters tested in Table 2 and provide Table 3 and 4 which report the average diel change for the constrained and unconstrained cases for each season tested. Spring and summer were sensitive to the date selected as that significantly impacted photolysis rates. Temperature impacted compounds that are known to be temperature sensitive (e.g. PNs).

*$NO_y$ Budget Comparisons to BAO Region*

Downtown Houston, TX provides an interesting comparison with the NFRMA. While meteorology and measurement techniques are different, both regions have large emissions associated with oil and natural gas production or refining, substantial traffic sources, and less biogenic influence than other urban regions such as Atlanta. While the site locations of Houston measurements differ significantly from BAO, they provide some context for observations at BAO. Houston and Denver encompass similar area, Houston is twice as populous and has the addition of a major shipping channel. $NO_y$ mixing ratios in Houston are ~2-4 times larger than observed at BAO. Peak $NO_y$ mixing ratios during TexAQS (summer 2000) and TexAQS-II (summer 2006) in Houston occur near sunrise (6:00) because the nitrogen budget is dominated by fresh $NO_x$ emissions [*Luke et al.*, 2010; *Rosen*, 2004].

The diel profile of NO exhibits a morning rush hour rise typical of a traffic-influenced site. Growth of the convective boundary layer in the mid- to late-morning, coupled with enhanced photochemistry and depositional losses decrease $NO_x$ mixing ratios after ~10:00. $NO_2$ mixing ratios (Figure 1.2) increase at night as late-day and nighttime emissions are injected into the compressed nocturnal boundary layer. The $NO/NO_2$ ratio is <0.05 in the early morning; near sunrise this ratio rapidly increases to 0.25-0.35 and remains in that range until 16:00 when the ratio decreases to <0.05 over ~4 hrs. NO mixing ratios are near zero at night due to rapid oxidation by $O_3$ to $NO_2$ [*Steven S. Brown et al.*, 2003]. Again, the $NO_x$ diel profiles are consistent with measurements from TexAQS-II 2006, although $NO_x$ mixing ratios were approximately half at BAO [*Luke et al.*, 2010].

The diel cycle for PAN and PPN are consistent with local photochemical production followed by nighttime deposition [*Fahey et al.*, 1986; *Shepson et al.*, 1992]. Lifetimes of PAN and PPN are sufficiently long that they persist overnight in the residual layer; some of the morning mixing ratio rise (06:00-12:00) may be due to down-mixing. Median mid-day (11:00-13:00) mixing ratios of PAN and PPN were 0.28 ppb and 0.04 ppb which is ~25% of measurements made in Houston during TexAQS-II 2006 [*Luke et al.*, 2010]. While the mixing ratios differ, the diel profile at BAO is consistent with other urban and suburban ground sites (e.g. Houston, TX: TexAQS-I 2000 and TexAQS-II 2006; Granite Bay, CA: summer 2001) [*Luke et al.*, 2010; *Murphy et al.*, 2006; *Perring et al.*, 2013; *Rosen*, 2004].

$HNO_3$ follows a clear photochemically-driven cycle (Figure 1.2) with a mid-day maximum and near-zero (<LOD) nighttime minima due to deposition and other losses consistent with Granite Bay (summer 2001) and Houston (TexAQS-I and II) [*Luke et al.*, 2010; *Murphy et al.*, 2006; *Perring et al.*, 2013; *Rosen*, 2004]. While we observed significant variability in observed $HNO_3$ at

BAO, median mixing ratios nominally increase 5-fold from 6:00 to 12:00. Mixing ratios of $HNO_3$ at BAO are approximately half of measurements made in Houston during TexAQS-II 2006, but constitute a similar fraction of the total $NO_y$ budget [*Luke et al.*, 2010].

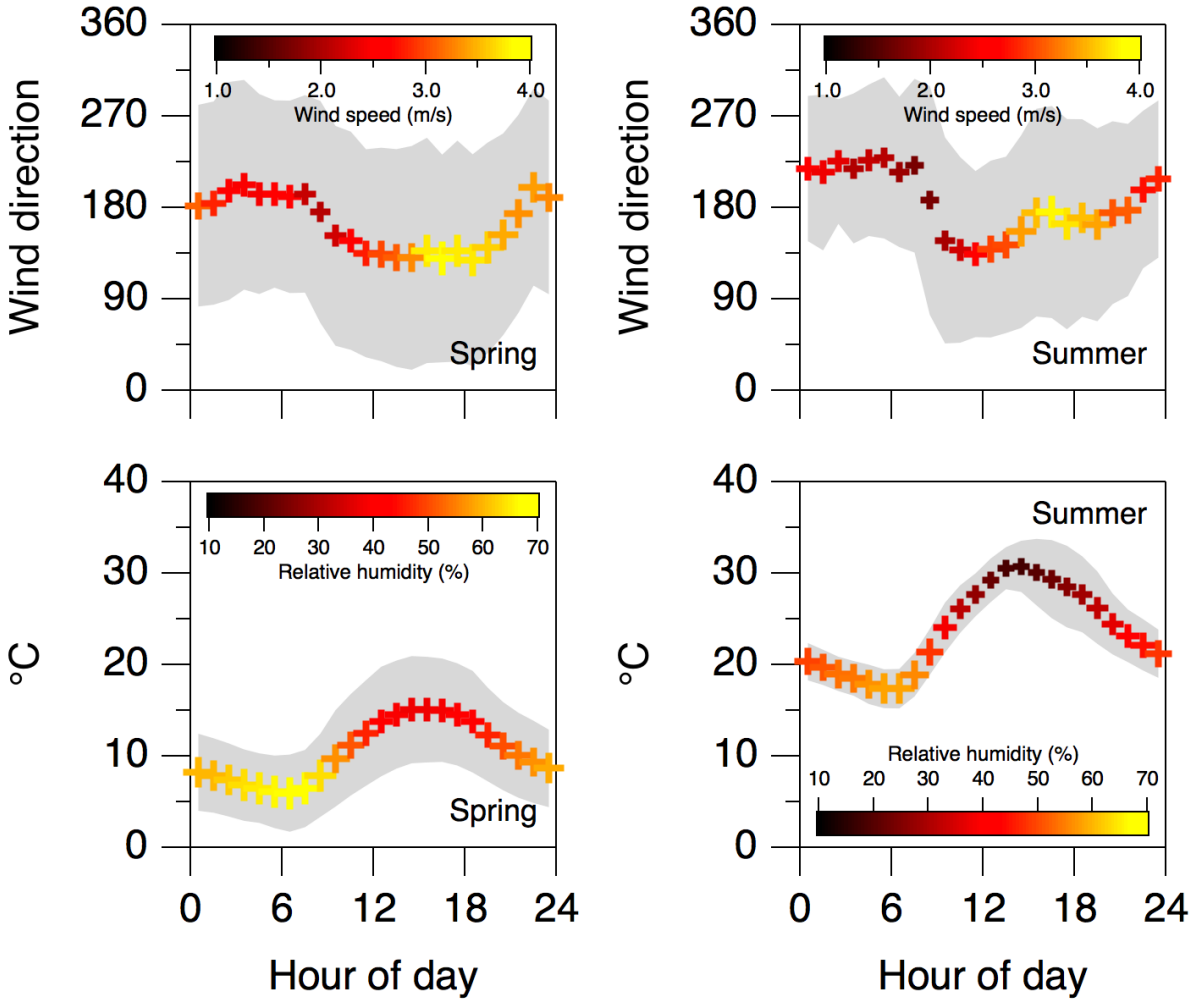


**Figure 1.8**: Diel average of wind direction colored by speed and diel average of temperature colored by relative humidity.

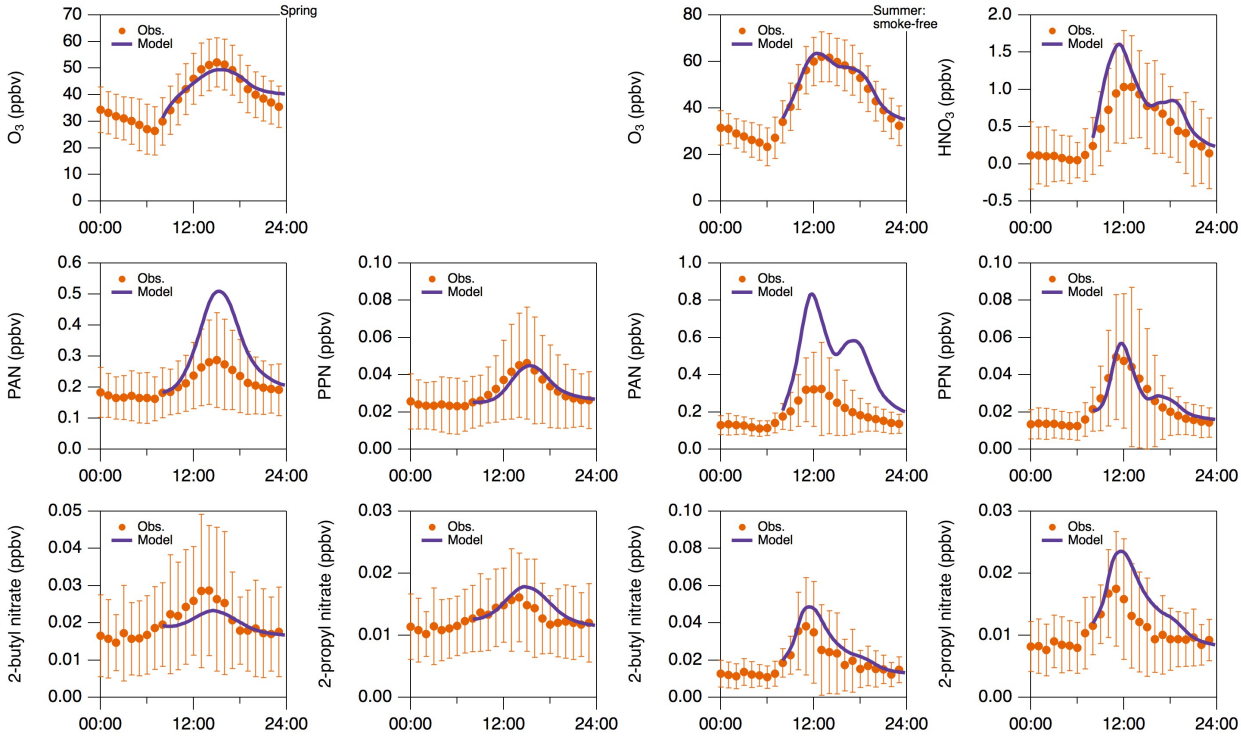


**Figure 1.9:** Model measurement comparison for the unconstrained case after 4 days of spin-up time.

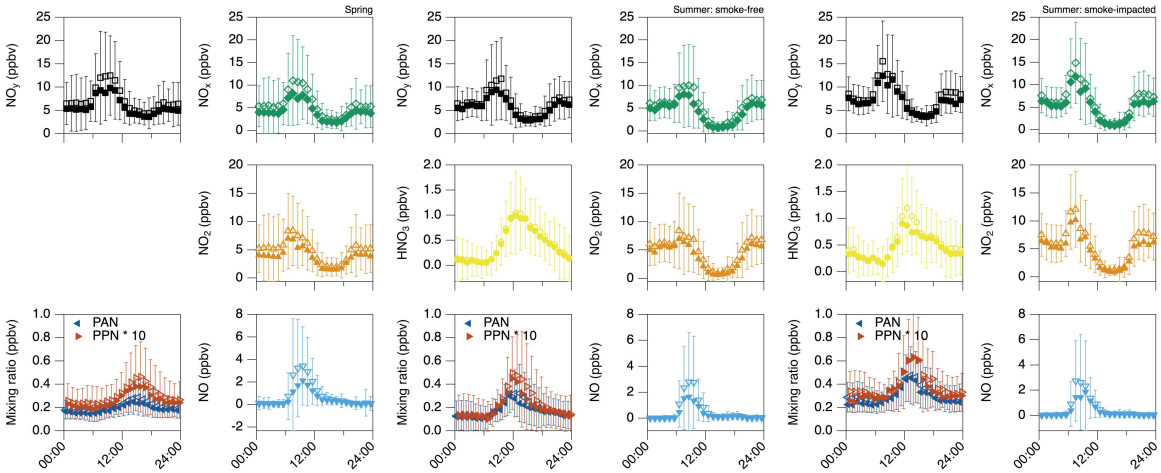


**Figure 1.10**: Diel average and medians with standard deviation of observations show for $NO_y$ species for spring, summer: smoke-free, and summer: smoke-impacted.

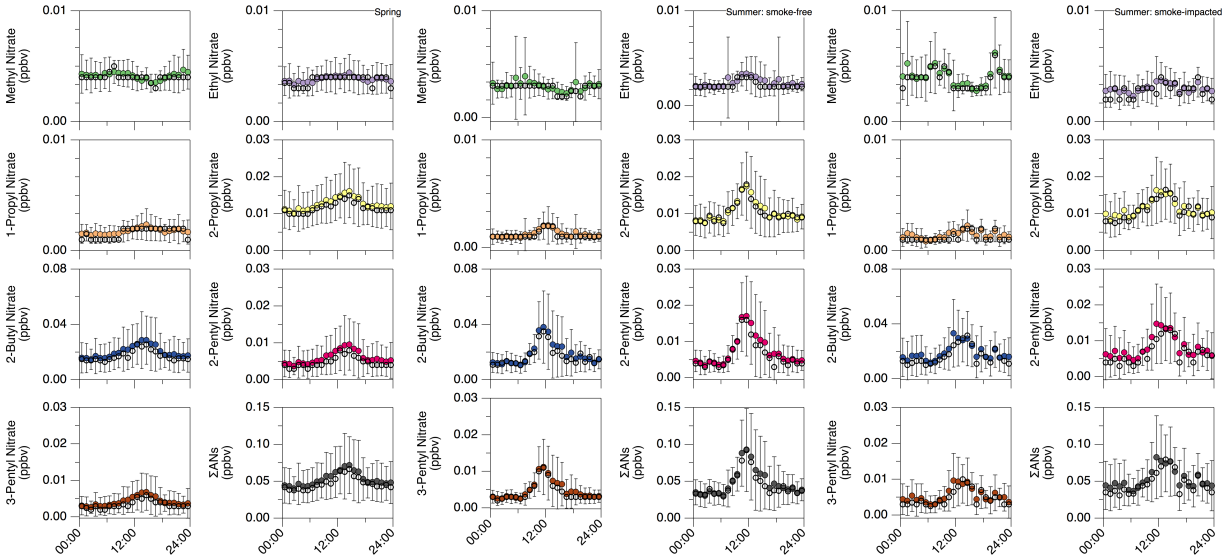


**Figure 1.11**: Diel averages and medians of measured organic nitrates for each distinct measurement period.

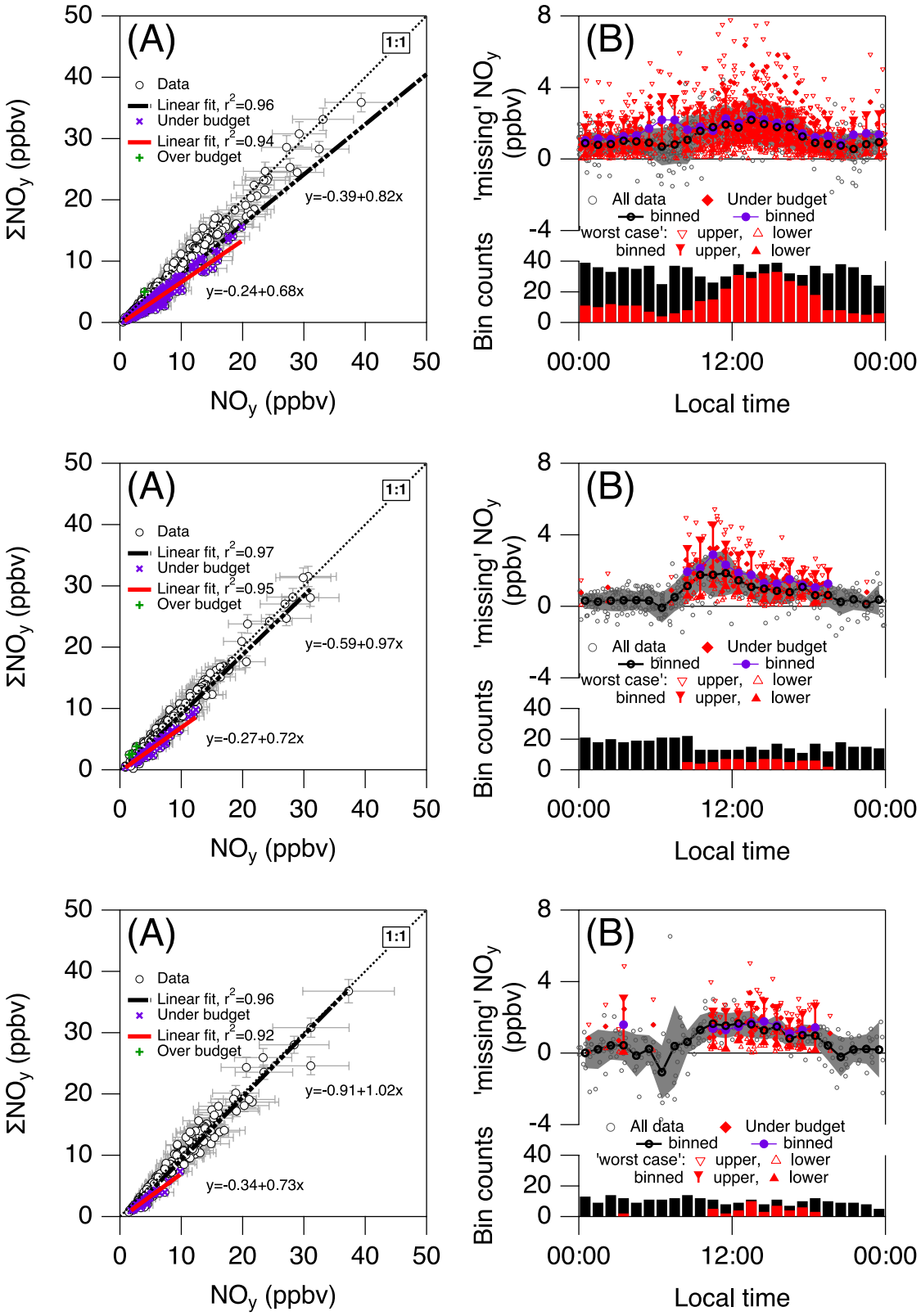


**Figure 1.12**: top is spring, middle is summer (smoke-free), bottom is smoke-impacted.

**Table 1.2:** Sensitivity parameters tested

| Parameter | Spring | Summer - Smoke free | Sensitivity | |
|---|---|---|---|---|
| ***Options*** | | | Low | High |
| **Date** | mid-campaign | mid-campaign | beginning of campaign | end of campaign |
| **Pressure (hPa)** | 835 | 835 | -10% | 10% |
| **Temperature (˚C)** | observations | observations | -10% | 10% |
| **Relative Humidity** | observations | observations | -10% | 10% |
| **Dilution** | 2.5 | 2 | -10% | 10% |
| **jCorr** | 1 | 1 | -20% | n/a |
| **Albedo** | 0.067 | 0.067 | -10% | 10% |
| **Boundary Layer Height (m)** | 2350 | 2750 | -10% | 10% |
| ***Other*** | | | | |
| **Deposition** | Literature | Literature | -25% | 25% |

**Table 1.3**: Constrained case for spring and summer: smoke-free model outputs. All values are reported as percent changed relative to the base case.

**Spring: constrained**

| | ANs | PNs | HNO3 | O3 | Notes |
|---|---|---|---|---|---|
| Early date | -13 | -7 | -33 | n/a | |
| Late date | 8 | 5 | 22 | n/a | |
| High Temp. | 4 | 0 | 7 | n/a | changes are pronounced during the day |
| Low Temp | -4 | 0 | 7 | n/a | changes are pronounced during the day |
| High Pres. | -4 | -2 | -5 | n/a | changes are more pronounced at night |
| Low Pres. | 5 | 2 | 5 | n/a | changes are more pronounced at night |
| High RH | 2 | 2 | 5 | n/a | |
| Low RH | -2 | -2 | -5 | n/a | |
| High albedo | 0 | 0 | 0 | n/a | |
| Low albedo | 0 | 0 | 0 | n/a | |
| High BLH | 0 | 0 | 5 | n/a | |
| Low BLH | 0 | 0 | 5 | n/a | |
| High dep. | -2 | -2 | -5 | n/a | |
| Low dep. | 2 | 2 | 5 | n/a | |
| Low Jcorr | -5 | -2 | -10 | n/a | |
| High Dil | n/a | n/a | n/a | n/a | |
| Low Dil | n/a | n/a | n/a | n/a | |

**Summer: smoke-free, constrained**

| | ANs | PNs | HNO3 | O3 | Notes |
|---|---|---|---|---|---|
| Early date | -7 | 1 | n/a | n/a | |
| Late date | 18 | 2 | n/a | n/a | |
| High Temp. | 11 | -5 | n/a | n/a | |
| Low Temp | -11 | 7 | n/a | n/a | |
| High Pres. | 5 | 2 | n/a | n/a | |
| Low Pres. | -5 | -2 | n/a | n/a | |
| High RH | 0 | 0 | n/a | n/a | |
| Low RH | 0 | 0 | n/a | n/a | |
| High albedo | 0 | 0 | n/a | n/a | |
| Low albedo | 0 | 0 | n/a | n/a | |
| High BLH | n/a | n/a | n/a | n/a | |
| Low BLH | n/a | n/a | n/a | n/a | |
| High dep. | n/a | n/a | n/a | n/a | |
| Low dep. | n/a | n/a | n/a | n/a | |
| Low Jcorr | 0 | -2 | n/a | n/a | |
| High Dil | n/a | n/a | n/a | n/a | |
| Low Dil | n/a | n/a | n/a | n/a | |

**Table 1.4**: Unconstrained case for spring and summer: smoke-free model outputs. All values are reported as percent changed relative to the base case.

**Spring: unconstrained**

| | ANs | PNs | HNO3 | O3 | Notes |
|---|---|---|---|---|---|
| Early date | -4 | -10 | -10 | -3 | |
| Late date | 3 | 7 | 7 | 2 | |
| High Temp. | 1 | 0 | 2 | 1 | |
| Low Temp | -1 | 0 | -2 | -1 | |
| High Pres. | -1 | -2 | -1 | -1 | |
| Low Pres. | 2 | 2 | 1 | 1 | |
| High RH | 1 | 2 | 1 | 0 | |
| Low RH | -1 | 2 | -1 | 0 | |
| High albedo | 0 | 0 | 0 | 0 | |
| Low albedo | 0 | 0 | 0 | 0 | |
| High BLH | 0 | 0 | 1 | 0 | more pronounced in the evening for $HNO_3$ |
| Low BLH | 0 | 0 | -1 | 0 | more pronounced in the evening for $HNO_3$ |
| High dep. | 0 | 0 | -2 | -1 | more pronounced in the evening for $HNO_3$ |
| Low dep. | 0 | 0 | 2 | 1 | more pronounced in the evening for $HNO_3$ |
| Low Jcorr | -2 | -3 | -3 | -1 | |
| High Dil | 1 | 2 | 1 | 0 | |
| Low Dil | -1 | -3 | -1 | 0 | |

**Summer: smoke-free, unconstrained**

| | ANs | PNs | HNO3 | O3 | Notes |
|---|---|---|---|---|---|
| Early date | -1 | 6 | 10 | 3 | pronounced early morning and late evening |
| Late date | 3 | -10 | -17 | -5 | pronounced early morning and late evening |
| High Temp. | 1 | -14 | 6 | 2 | effects on PNs are pronounced at midday |
| Low Temp | 2 | 14 | -5 | -2 | effects on PNs are pronounced at midday |
| High Pres. | 0 | 1 | 1 | -1 | |
| Low Pres. | 0 | -1 | -2 | 1 | |
| High RH | 0 | 1 | 1 | 0 | |
| Low RH | 0 | -1 | -1 | 0 | |
| High albedo | 0 | 0 | 0 | 0 | |
| Low albedo | 0 | 0 | 0 | 0 | |
| High BLH | 0 | 0 | 1 | 0 | more pronounced in the evening for $HNO_3$ |
| Low BLH | 0 | 0 | -1 | 0 | more pronounced in the evening for $HNO_3$ |
| High dep. | 0 | 0 | -2 | 0 | more pronounced in the evening for $HNO_3$ |
| Low dep. | 0 | 0 | 2 | 0 | more pronounced in the evening for $HNO_3$ |
| Low Jcorr | 0 | -4 | -7 | -3 | |
| High Dil | 0 | 3 | 7 | 2 | |
| Low Dil | 0 | -3 | -7 | -2 | |

**Table 1.5**: Average reactive nitrogen oxide species' mixing ratios during spring and the smoke-impacted period with mathematical comparisons to summer mixing ratios. Color scales indicate increases (red) or decreases (blue) relative to summer, magnitude scales with color intensity up to a fixed value (0.1 ppb for Δ and 50 % for % Δ). Average reported mixing ratios are for either spring or smoke-impacted periods, average summer mixing ratios can be extracted by subtracting Δ.

| | Day | | | Night | | |
|---|---|---|---|---|---|---|
| Spring relative to summer | Mixing ratio (ppb) | Δ (ppb) | % Δ | Mixing ratio (ppb) | Δ (ppb) | % Δ |
| $NO_y$ | 7.80 | 0.98 | 14 | 6.98 | 0.35 | 5 |
| NO | 1.50 | 0.65 | 76 | 0.15 | 0.13 | 623 |
| $NO_2$ | 4.39 | 0.42 | 11 | 5.80 | -0.16 | -3 |
| $HNO_3$ | | | | | | |
| PAN | 0.23 | -0.01 | -5 | 0.18 | 0.04 | 30 |
| PPN | 0.03 | 0.00 | 1 | 0.02 | 0.01 | 50 |
| ΣANs | 0.06 | 0.00 | 4 | 0.05 | 0.01 | 30 |

**Table 1.6**: Average reactive nitrogen oxide species' mixing ratios during spring and the smoke-impacted period with mathematical comparisons to summer mixing ratios. Color scales indicate increases (red) or decreases (blue) relative to summer, magnitude scales with color intensity up to a fixed value (0.1 ppb for Δ and 50 % for % Δ). Average reported mixing ratios are for either spring or smoke-impacted periods, average summer mixing ratios can be extracted by subtracting Δ.

| | Day | | | Night | | |
|---|---|---|---|---|---|---|
| Smoke-impacted relative to summer | Mixing ratio (ppb) | Δ (ppb) | % Δ | Mixing ratio (ppb) | Mixing ratio (ppb) | Δ (ppb) |
| $NO_y$ | 8.26 | 1.43 | 21 | 7.88 | 1.25 | 19 |
| NO | 1.00 | 0.14 | 16 | 0.05 | 0.03 | 140 |
| $NO_2$ | 5.18 | 1.20 | 30 | 7.00 | 1.04 | 17 |
| $HNO_3$ | 0.63 | -0.04 | -7 | 0.37 | 0.20 | 116 |
| PAN | 0.36 | 0.12 | 51 | 0.31 | 0.17 | 124 |
| PPN | 0.04 | 0.01 | 32 | 0.04 | 0.02 | 116 |
| ΣANs | 0.06 | 0.00 | 3 | 0.04 | 0.01 | 27 |

# CHAPTER 1 REFERENCES


Abeleira, A., I. B. Pollack, B. Sive, Y. Zhou, E. V. Fischer, and D. K. Farmer (2017), Source characterization of volatile organic compounds in the Colorado Northern Front Range Metropolitan Area during spring and summer 2015, *Journal of Geophysical Research: Atmospheres*, *122*(6), 3595-3613, doi:10.1002/2016jd026227.

Abeleira, A., B. Sive, R. F. Swarthout, E. V. Fischer, Y. Zhou, and D. K. Farmer (2018), Seasonality, sources and sinks of $C_1$–$C_5$ alkyl nitrates in the Colorado Front Range, *Elem Sci Anth*, *6*(1), doi:10.1525/elementa.299.

Abeleira, A. J., and D. K. Farmer (2017), Summer ozone in the northern Front Range metropolitan area: weekend–weekday effects, temperature dependences, and the impact of drought, *Atmospheric Chemistry and Physics*, *17*(11), 6517-6529, doi:10.5194/acp-17-6517-2017.

Aschmann, S. M., E. C. Tuazon, J. Arey, and R. Atkinson (2011), Products of the OH radical-initiated reactions of 2-propyl nitrate, 3-methyl-2-butyl nitrate and 3-methyl-2-pentyl nitrate, *Atmospheric Environment*, *45*(9), 1695-1701, doi:10.1016/j.atmosenv.2010.12.061.

Bell, M. L., F. Dominici, and J. M. Samet (2005), A Meta-Analysis of Time-Series Studies of Ozone and Mortality With Comparison to the National Morbidity, Mortality, and Air Pollution Study, *Epidemiology*, *16*(4), 436-445, doi:10.1097/01.ede.0000165817.40152.85.

Benedict, K. B., C. M. Carrico, S. M. Kreidenweis, B. Schichtel, W. C. Malm, and J. L. Collett (2013), A seasonal nitrogen deposition budget for Rocky Mountain National Park, *Ecol Appl*, *23*(5), 1156-1169, doi:10.1890/12-1624.1.

Booker, F., R. Muntifering, M. McGrath, K. Burkey, D. Decoteau, E. Fiscus, W. Manning, S. Krupa, A. Chappelka, and D. Grantz (2009), The Ozone Component of Global Change: Potential Effects on Agricultural and Horticultural Plant Yield, Product Quality and Interactions with Invasive Species, *Journal of Integrative Plant Biology*, *51*(4), 337-351, doi:10.1111/j.1744-7909.2008.00805.x.

Brey, S. J., and E. V. Fischer (2016), Smoke in the City: How Often and Where Does Smoke Impact Summertime Ozone in the United States?, *Environ Sci Technol*, *50*(3), 1288-1294, doi:10.1021/acs.est.5b05218.

Brown, S. S., W. P. Dubé, H. D. Osthoff, D. E. Wolfe, W. M. Angevine, and A. R. Ravishankara (2007), High resolution vertical distributions of NO<sub>3</sub> and N<sub>2</sub>O<sub>5</sub> through the nocturnal boundary layer, *Atmospheric Chemistry and Physics*, *7*(1), 139-149, doi:10.5194/acp-7-139-2007.

Brown, S. S., H. Stark, T. B. Ryerson, E. J. Williams, D. K. Nicks, M. Trainer, F. C. Fehsenfeld, and A. R. Ravishankara (2003), Nitrogen oxides in the nocturnal boundary layer: Simultaneous in situ measurements of NO3, N2O5, NO2, NO, and O3, *Journal of Geophysical Research: Atmospheres*, *108*(D9), n/a-n/a, doi:10.1029/2002jd002917.

Butler, T. J., F. M. Vermeylen, M. Rury, G. E. Likens, B. Lee, G. E. Bowker, and L. McCluney (2011), Response of ozone and nitrate to stationary source NOx emission reductions in the eastern USA, *Atmospheric Environment*, *45*(5), 1084-1094, doi:10.1016/j.atmosenv.2010.11.040.

Change, I. P. o. C. (2014), *Climate Change 2013 – The Physical Science Basis: Working Group I Contribution to the Fifth Assessment Report of the Intergovernmental Panel on Climate Change*, Cambridge University Press, Cambridge, doi:DOI: 10.1017/CBO9781107415324.

Cheadle, L. C., S. J. Oltmans, G. Petron, R. C. Schnell, E. J. Mattson, S. C. Herndon, A. M. Thompson, D. R. Blake, and A. McClure-Begley (2017), Surface ozone in the Colorado northern Front Range and the influence of

oil and gas development during FRAPPE/DISCOVER-AQ in summer 2014, *Elem Sci Anth*, *5*(0), doi:10.1525/elementa.254.

Cleary, P. A., P. J. Wooldridge, D. B. Millet, M. McKay, A. H. Goldstein, and R. C. Cohen (2007), Observations of total peroxy nitrates and aldehydes: measurement interpretation and inference of OH radical concentrations, *Atmospheric Chemistry and Physics*, *7*(8), 1947-1960, doi:10.5194/acp-7-1947-2007.

Coggon, M. M., et al. (2018), Diurnal Variability and Emission Pattern of Decamethylcyclopentasiloxane (D-5) from the Application of Personal Care Products in Two North American Cities, *Environmental Science & Technology*, *52*(10), 5610-5618, doi:10.1021/acs.est.8b00506.

Cooper, O. R., R.-S. Gao, D. Tarasick, T. Leblanc, and C. Sweeney (2012), Long-term ozone trends at rural ozone monitoring sites across the United States, 1990-2010, *Journal of Geophysical Research: Atmospheres*, *117*(D22), n/a-n/a, doi:10.1029/2012jd018261.

Cooper, O. R., A. O. Langford, D. D. Parrish, and D. W. Fahey (2015), Atmosphere. Challenges of a lowered U.S. ozone standard, *Science*, *348*(6239), 1096-1097, doi:10.1126/science.aaa5748.

Day, D. A. (2003), On alkyl nitrates, O3, and the "missing NOy", *Journal of Geophysical Research*, *108*(D16), doi:10.1029/2003jd003685.

Day, D. A., D. K. Farmer, A. H. Goldstein, P. J. Wooldridge, C. Minejima, and R. C. Cohen (2009), Observations of NO<sub>x</sub>, ΣPNs, ΣANs, and HNO<sub>3</sub> at a Rural Site in the California Sierra Nevada Mountains: summertime diurnal cycles, *Atmospheric Chemistry and Physics*, *9*(14), 4879-4896, doi:10.5194/acp-9-4879-2009.

Demetillo, M. A. G., J. F. Anderson, J. A. Geddes, X. Yang, E. Y. Najacht, S. A. Herrera, K. M. Kabasares, A. E. Kotsakis, M. T. Lerdau, and S. E. Pusede (2019), Observing Severe Drought Influences on Ozone Air Pollution in California, *Environ Sci Technol*, *53*(9), 4695-4706, doi:10.1021/acs.est.8b04852.

Ellis, R. A., J. G. Murphy, E. Pattey, R. van Haarlem, J. M. O'Brien, and S. C. Herndon (2010), Characterizing a Quantum Cascade Tunable Infrared Laser Differential Absorption Spectrometer (QC-TILDAS) for measurements of atmospheric ammonia, *Atmospheric Measurement Techniques*, *3*(2), 397-406, doi:10.5194/amt-3-397-2010.

Fahey, D. W., G. Hübler, D. D. Parrish, E. J. Williams, R. B. Norton, B. A. Ridley, H. B. Singh, S. C. Liu, and F. C. Fehsenfeld (1986), Reactive nitrogen species in the troposphere: Measurements of NO, NO2, HNO3, particulate nitrate, peroxyacetyl nitrate (PAN), O3, and total reactive odd nitrogen (NOy) at Niwot Ridge, Colorado, *Journal of Geophysical Research*, *91*(D9), doi:10.1029/JD091iD09p09781.

Farmer, D. K., A. E. Perring, P. J. Wooldridge, D. R. Blake, A. Baker, S. Meinardi, L. G. Huey, D. Tanner, O. Vargas, and R. C. Cohen (2011), Impact of organic nitrates on urban ozone

production, *Atmospheric Chemistry and Physics*, *11*(9), 4085-4094, doi:10.5194/acp-11-4085-2011.

Fehsenfeld, F. C., et al. (1987), A ground-based intercomparison of NO, NOx, and NOymeasurement techniques, *Journal of Geophysical Research*, *92*(D12), doi:10.1029/JD092iD12p14710.

Flocke, F. M., A. J. Weinheimer, A. L. Swanson, J. M. Roberts, R. Schmitt, and S. Shertz (2005), On the Measurement of PANs by Gas Chromatography and Electron Capture Detection, *Journal of Atmospheric Chemistry*, *52*(1), 19-43, doi:10.1007/s10874-005-6772-0.

Gilman, J. B., B. M. Lerner, W. C. Kuster, and J. A. de Gouw (2013), Source signature of volatile organic compounds from oil and natural gas operations in northeastern Colorado, *Environ Sci Technol*, *47*(3), 1297-1305, doi:10.1021/es304119a.

Heald, C. L., et al. (2003), Asian outflow and trans-Pacific transport of carbon monoxide and ozone pollution: An integrated satellite, aircraft, and model perspective, *Journal of Geophysical Research: Atmospheres*, *108*(D24), n/a-n/a, doi:10.1029/2003jd003507.

Horowitz, L. W., A. M. Fiore, G. P. Milly, R. C. Cohen, A. Perring, P. J. Wooldridge, P. G. Hess, L. K. Emmons, and J.-F. Lamarque (2007), Observational constraints on the chemistry of isoprene nitrates over the eastern United States, *Journal of Geophysical Research*, *112*(D12), doi:10.1029/2006jd007747.

Hudman, R. C., et al. (2004), Ozone production in transpacific Asian pollution plumes and implications for ozone air quality in California, *Journal of Geophysical Research: Atmospheres*, *109*(D23), doi:10.1029/2004jd004974.

Ito, A., S. Sillman, and J. E. Penner (2009), Global chemical transport model study of ozone response to changes in chemical kinetics and biogenic volatile organic compounds emissions due to increasing temperatures: Sensitivities to isoprene nitrate chemistry and grid resolution, *Journal of Geophysical Research*, *114*(D9), doi:10.1029/2008jd011254.

Kaimal, J. C., and J. E. Gaynor (1983), The Boulder Atmospheric Observatory, *Journal of Climate and Applied Meteorology*, *22*(5), 863-880, doi:10.1175/1520-0450(1983)022<0863:Tbao>2.0.Co;2.

Kim, S., et al. (2014), The primary and recycling sources of OH during the NACHTT-2011 campaign: HONO as an important OH primary source in the wintertime, *Journal of Geophysical Research: Atmospheres*, *119*(11), 6886-6896, doi:10.1002/2013jd019784.

Kleinman, L. I. (2005), The dependence of tropospheric ozone production rate on ozone precursors, *Atmospheric Environment*, *39*(3), 575-586, doi:10.1016/j.atmosenv.2004.08.047.

Kley, D., J. W. Drummond, M. Mcfarland, and S. C. Liu (1981), Tropospheric Profiles of Nox, *J Geophys Res-Oceans*, *86*(Nc4), 3153-3161, doi:DOI 10.1029/JC086iC04p03153.

Koppmann, R. (2007), Volatile organic compounds in the atmosphere, 269-291.

Lin, M., A. M. Fiore, L. W. Horowitz, A. O. Langford, S. J. Oltmans, D. Tarasick, and H. E. Rieder (2015), Climate variability modulates western US ozone air quality in spring via deep stratospheric intrusions, *Nat Commun*, *6*, 7105, doi:10.1038/ncomms8105.

Lin, X., M. Trainer, and S. C. Liu (1988), On the nonlinearity of the tropospheric ozone production, *Journal of Geophysical Research*, *93*(D12), doi:10.1029/JD093iD12p15879.

Lindaas, J., D. K. Farmer, I. B. Pollack, A. Abeleira, F. Flocke, and E. V. Fischer (2019), Acyl Peroxy Nitrates Link Oil and Natural Gas Emissions to High Ozone Abundances in the Colorado Front Range During Summer 2015, *J Geophys Res-Atmos*, *124*(4), 2336-2350, doi:10.1029/2018jd028825.

Lindaas, J., D. K. Farmer, I. B. Pollack, A. Abeleira, F. Flocke, R. Roscioli, S. Herndon, and E. V. Fischer (2017), Changes in ozone and precursors during two aged wildfire smoke events in the Colorado Front Range in summer 2015, *Atmospheric Chemistry and Physics*, *17*(17), 10691-10707, doi:10.5194/acp-17-10691-2017.

Liu, S. C., M. Mcfarland, D. Kley, O. Zafiriou, and B. Huebert (1983), Tropospheric Nox and O3 Budgets in the Equatorial Pacific, *J Geophys Res-Oceans*, *88*(Nc2), 1360-1368, doi:DOI 10.1029/JC088iC02p01360.

Liu, S. C., and M. Trainer (1988), Responses of the tropospheric ozone and odd hydrogen radicals to column ozone change, *Journal of Atmospheric Chemistry*, *6*(3), 221-233, doi:10.1007/bf00053857.

Liu, S. C., M. Trainer, F. C. Fehsenfeld, D. D. Parrish, E. J. Williams, D. W. Fahey, G. Hubler, and P. C. Murphy (1987a), Ozone Production in the Rural Troposphere and the Implications for Regional and Global Ozone Distributions, *J Geophys Res-Atmos*, *92*(D4), 4191-4207, doi:DOI 10.1029/JD092iD04p04191.

Liu, S. C., M. Trainer, F. C. Fehsenfeld, D. D. Parrish, E. J. Williams, D. W. Fahey, G. Hübler, and P. C. Murphy (1987b), Ozone production in the rural troposphere and the implications for regional and global ozone distributions, *Journal of Geophysical Research*, *92*(D4), doi:10.1029/JD092iD04p04191.

Luke, W. T., P. Kelley, B. L. Lefer, J. Flynn, B. Rappenglück, M. Leuchner, J. E. Dibb, L. D. Ziemba, C. H. Anderson, and M. Buhr (2010), Measurements of primary trace gases and NOY composition in Houston, Texas, *Atmospheric Environment*, *44*(33), 4068-4080, doi:10.1016/j.atmosenv.2009.08.014.

May, P. T., and J. M. Wilczak (1993), Diurnal and Seasonal Variations of Boundary-Layer Structure Observed with a Radar Wind Profiler and RASS, *Monthly Weather Review*, *121*(3), 673-682, doi:10.1175/1520-0493(1993)121<0673:Dasvob>2.0.Co;2.

McDonald, B. C., et al. (2018), Volatile chemical products emerging as largest petrochemical source of urban organic emissions, *Science*, *359*(6377), 760-764, doi:ARTN aaq052410.1126/science.aaq0524.

McDuffie, E. E., et al. (2016), Influence of oil and gas emissions on summertime ozone in the Colorado Northern Front Range, *Journal of Geophysical Research: Atmospheres*, *121*(14), 8712-8729, doi:10.1002/2016jd025265.

McManus, J. B., M. S. Zahniser, and D. D. Nelson (2011), Dual quantum cascade laser trace gas instrument with astigmatic Herriott cell at high pass number, *Appl Opt*, *50*(4), A74-85, doi:10.1364/AO.50.000A74.

Millet, D. B., M. Baasandorj, L. Hu, D. Mitroo, J. Turner, and B. J. Williams (2016), Nighttime Chemistry and Morning Isoprene Can Drive Urban Ozone Downwind of a Major Deciduous Forest, *Environ Sci Technol*, *50*(8), 4335-4342, doi:10.1021/acs.est.5b06367.

Moxim, W. J., H. Levy, and P. S. Kasibhatla (1996), Simulated global tropospheric PAN: Its transport and impact on NOx, *Journal of Geophysical Research: Atmospheres*, *101*(D7), 12621-12638, doi:10.1029/96jd00338.

Murphy, J. G., D. A. Day, P. A. Cleary, P. J. Wooldridge, and R. C. Cohen (2006), Observations of the diurnal and seasonal trends in nitrogen oxides in the western Sierra Nevada, *Atmospheric Chemistry and Physics*, *6*(12), 5321-5338, doi:10.5194/acp-6-5321-2006.

Murphy, J. G., D. A. Day, P. A. Cleary, P. J. Wooldridge, D. B. Millet, A. H. Goldstein, and R. C. Cohen (2007), The weekend effect within and downwind of Sacramento – Part 1:

Observations of ozone, nitrogen oxides, and VOC reactivity, *Atmospheric Chemistry and Physics*, *7*(20), 5327-5339, doi:10.5194/acp-7-5327-2007.

Nunnermacker, L. J. (1990), Calibration and Detection of Reactive Nitrogen Compounds in the Atmosphere, Ph.D. thesis, University of Maryland, College Park, MD.

Parrish, D. D., R. B. Norton, M. J. Bollinger, S. C. Liu, P. C. Murphy, D. L. Albritton, F. C. Fehsenfeld, and B. J. Huebert (1986), Measurements of Hno3 and No3- Particulates at a Rural Site in the Colorado Mountains, *J Geophys Res-Atmos*, *91*(D5), 5379-5393, doi:DOI 10.1029/JD091iD05p05379.

Perring, A. E., et al. (2010), The production and persistence of ΣRONO<sub>2</sub> in the Mexico City plume, *Atmospheric Chemistry and Physics*, *10*(15), 7215-7229, doi:10.5194/acp-10-7215-2010.

Perring, A. E., et al. (2009), Airborne observations of total RONO<sub>2</sub>: new constraints on the yield and lifetime of isoprene nitrates, *Atmospheric Chemistry and Physics*, *9*(4), 1451-1463, doi:10.5194/acp-9-1451-2009.

Perring, A. E., S. E. Pusede, and R. C. Cohen (2013), An observational perspective on the atmospheric impacts of alkyl and multifunctional nitrates on ozone and secondary organic aerosol, *Chem Rev*, *113*(8), 5848-5870, doi:10.1021/cr300520x.

Pétron, G., et al. (2012), Hydrocarbon emissions characterization in the Colorado Front Range: A pilot study, *Journal of Geophysical Research: Atmospheres*, *117*(D4), n/a-n/a, doi:10.1029/2011jd016360.

Pétron, G., et al. (2014), A new look at methane and nonmethane hydrocarbon emissions from oil and natural gas operations in the Colorado Denver-Julesburg Basin, *Journal of Geophysical Research: Atmospheres*, *119*(11), 6836-6852, doi:10.1002/2013jd021272.

Pollack, I. B., T. B. Ryerson, M. Trainer, J. A. Neuman, J. M. Roberts, and D. D. Parrish (2013), Trends in ozone, its precursors, and related secondary oxidation products in Los Angeles, California: A synthesis of measurements from 1960 to 2010, *Journal of Geophysical Research: Atmospheres*, *118*(11), 5893-5911, doi:10.1002/jgrd.50472.

Pope, C. A., and D. W. Dockery (2006), Health effects of fine particulate air pollution: Lines that connect, *Journal of the Air & Waste Management Association*, *56*(6), 709-742, doi:Doi 10.1080/10473289.2006.10464485.

Reddy, P. J., and G. G. Pfister (2016), Meteorological factors contributing to the interannual variability of midsummer surface ozone in Colorado, Utah, and other western U.S. states, *Journal of Geophysical Research: Atmospheres*, *121*(5), 2434-2456, doi:10.1002/2015jd023840.

Ridley, B. A. (1991), Recent measurements of oxidized nitrogen compounds in the troposphere, *Atmospheric Environment. Part A. General Topics*, *25*(9), 1905-1926, doi:10.1016/0960-1686(91)90273-a.

Roscioli, J. R., M. S. Zahniser, D. D. Nelson, S. C. Herndon, and C. E. Kolb (2016), New Approaches to Measuring Sticky Molecules: Improvement of Instrumental Response Times Using Active Passivation, *J Phys Chem A*, *120*(9), 1347-1357, doi:10.1021/acs.jpca.5b04395.

Rosen, R. S. (2004), Observations of total alkyl nitrates during Texas Air Quality Study 2000: Implications for O3and alkyl nitrate photochemistry, *Journal of Geophysical Research*, *109*(D7), doi:10.1029/2003jd004227.

Selin, N. E., S. Wu, K. M. Nam, J. M. Reilly, S. Paltsev, R. G. Prinn, and M. D. Webster (2009), Global health and economic impacts of future ozone pollution, *Environmental Research Letters*, *4*(4), doi:Artn 04401410.1088/1748-9326/4/4/044014.

Shepson, P. B., K. G. Anlauf, J. W. Bottenheim, H. A. Wiebe, N. Gao, K. Muthuramu, and G. I. Mackay (1993), Alkyl nitrates and their contribution to reactive nitrogen at a rural site in Ontario, *Atmospheric Environment. Part A. General Topics*, *27*(5), 749-757, doi:10.1016/0960-1686(93)90192-2.

Shepson, P. B., J. W. Bottenheim, D. R. Hastie, and A. Venkatram (1992), Determination of the relative ozone and PAN deposition velocities at night, *Geophysical Research Letters*, *19*(11), 1121-1124, doi:10.1029/92gl01118.

Sillman, S., D. He, C. Cardelino, and R. E. Imhoff (1997), The Use of Photochemical Indicators to Evaluate Ozone-NOx-Hydrocarbon Sensitivity: Case Studies from Atlanta, New York, and Los Angeles, *J Air Waste Manag Assoc*, *47*(10), 1030-1040, doi:10.1080/10962247.1997.11877500.

Sillman, S., and P. J. Samson (1995), Impact of temperature on oxidant photochemistry in urban, polluted rural and remote environments, *Journal of Geophysical Research*, *100*(D6), doi:10.1029/94jd02146.

Silverman, R. A., and K. Ito (2009), Age Related Associations of Fine Particles and Ozone with Severe Acute Asthma in New York City, *Am J Resp Crit Care*, *179*.

Singh, H. B., and P. L. Hanst (1981), Peroxyacetyl nitrate (PAN) in the unpolluted atmosphere: An important reservoir for nitrogen oxides, *Geophysical Research Letters*, *8*(8), 941-944, doi:10.1029/GL008i008p00941.

Sive, B. C., Y. Zhou, D. Troop, Y. Wang, W. C. Little, O. W. Wingenter, R. S. Russo, R. K. Varner, and R. Talbot (2005), Development of a cryogen-free concentration system for measurements of volatile organic compounds, *Anal Chem*, *77*(21), 6989-6998, doi:10.1021/ac0506231.

Strode, S. A., J. M. Rodriguez, J. A. Logan, O. R. Cooper, J. C. Witte, L. N. Lamsal, M. Damon, B. Van Aartsen, S. D. Steenrod, and S. E. Strahan (2015), Trends and variability in surface ozone over the United States, *Journal of Geophysical Research: Atmospheres*, *120*(17), 9020-9042, doi:10.1002/2014jd022784.

Tevlin, A. G., Y. Li, J. L. Collett, E. E. McDuffie, E. V. Fischer, and J. G. Murphy (2017), Tall Tower Vertical Profiles and Diurnal Trends of Ammonia in the Colorado Front Range, *J Geophys Res-Atmos*, *122*(22), 12468-12487, doi:10.1002/2017jd026534.

Thompson, T. M., M. A. Rodriguez, M. G. Barna, K. A. Gebhart, J. L. Hand, D. E. Day, W. C. Malm, K. B. Benedict, J. L. Collett, and B. A. Schichtel (2015), Rocky Mountain National Park reduced nitrogen source apportionment, *Journal of Geophysical Research: Atmospheres*, *120*(9), 4370-4384, doi:10.1002/2014jd022675.

Thornton, J. A. (2002), Ozone production rates as a function of NOxabundances and HOxproduction rates in the Nashville urban plume, *Journal of Geophysical Research*, *107*(D12), doi:10.1029/2001jd000932.

Thornton, J. A., et al. (2010), A large atomic chlorine source inferred from mid-continental reactive nitrogen chemistry, *Nature*, *464*(7286), 271-274, doi:10.1038/nature08905.

Ulbrich, I. M., M. R. Canagaratna, Q. Zhang, D. R. Worsnop, and J. L. Jimenez (2009), Interpretation of organic components from Positive Matrix Factorization of aerosol mass spectrometric data, *Atmospheric Chemistry and Physics*, *9*(9), 2891-2918, doi:10.5194/acp-9-2891-2009.

Vu, K. T., et al. (2016), Impacts of the Denver Cyclone on regional air quality and aerosol formation in the Colorado Front Range during FRAPPÉ 2014, *Atmospheric Chemistry and Physics*, *16*(18), 12039-12058, doi:10.5194/acp-16-12039-2016.

Wagner, N. L., et al. (2013), N2O5uptake coefficients and nocturnal NO2removal rates determined from ambient wintertime measurements, *Journal of Geophysical Research: Atmospheres*, *118*(16), 9331-9350, doi:10.1002/jgrd.50653.

Warneck, P., and T. Zerbach (1992), Synthesis of peroxyacetyl nitrate in air by acetone photolysis, *Environmental Science & Technology*, *26*(1), 74-79, doi:10.1021/es00025a005.

Wild, R. J., et al. (2016), Reactive nitrogen partitioning and its relationship to winter ozone events in Utah, *Atmospheric Chemistry and Physics*, *16*(2), 573-583, doi:10.5194/acp-16-573-2016.

Williams, E. J., et al. (1998), Intercomparison of ground-based NOymeasurement techniques, *Journal of Geophysical Research: Atmospheres*, *103*(D17), 22261-22280, doi:10.1029/98jd00074.

Wolfe, G. M., M. R. Marvin, S. J. Roberts, K. R. Travis, and J. Liao (2016), The Framework for 0-D Atmospheric Modeling (F0AM) v3.1, *Geoscientific Model Development*, *9*(9), 3309-3319, doi:10.5194/gmd-9-3309-2016.

Womack, C. C., et al. (2019), An Odd Oxygen Framework for Wintertime Ammonium Nitrate Aerosol Pollution in Urban Areas: NOx and VOC Control as Mitigation Strategies, *Geophysical Research Letters*, *46*(9), 4971-4979, doi:10.1029/2019gl082028.

Wood, E. C., et al. (2009), A case study of ozone production, nitrogen oxides, and the radical budget in Mexico City, *Atmospheric Chemistry and Physics*, *9*(7), 2499-2516, doi:10.5194/acp-9-2499-2009.

Zaragoza, J., et al. (2017), Observations of Acyl Peroxy Nitrates During the Front Range Air Pollution and Photochemistry Experiment (FRAPPE), *J Geophys Res-Atmos*, *122*(22), 12416-12432, doi:10.1002/2017jd027337.

Zhou, Y., H. Mao, R. S. Russo, D. R. Blake, O. W. Wingenter, K. B. Haase, J. Ambrose, R. K. Varner, R. Talbot, and B. C. Sive (2008), Bromoform and dibromomethane measurements in the seacoast region of New Hampshire, 2002–2004, *Journal of Geophysical Research*, *113*(D8), doi:10.1029/2007jd009103.

Zhou, Y., R. K. Varner, R. S. Russo, O. W. Wingenter, K. B. Haase, R. Talbot, and B. C. Sive (2005), Coastal water source of short-lived halocarbons in New England, *Journal of Geophysical Research*, *110*(D21), doi:10.1029/2004jd005603.

# CHAPTER 2 – DIRECT MEASUREMENTS OF DRY AND WET DEPOSITION OF BLACK CARBON OVER A GRASSLAND[2]

## Overview

The atmospheric lifetime of black carbon (BC) is controlled by wet and dry deposition, which are poorly constrained by observations. We show that the single particle soot photometer (SP2) can measure surface-atmosphere exchange fluxes of refractory BC (rBC) particle mass ($m_{rBC}$) and number ($N_{rBC}$) by eddy covariance. We report field measurements of rBC dry and wet deposition rates during summer 2017 at the Southern Great Plains site in Oklahoma. On average, dry deposition of rBC is 0.3 ± 0.2 mm $s^{-1}$, but can be as high as 3.7 ± 0.3 mm $s^{-1}$ in periods where deposition is dominant. We estimate a wet deposition flux of 2600 ng $m^{-2}$ $hr^{-1}$ over the 148.5 mm of rainfall observed. Using a variety of approaches, these data indicate a composite rBC lifetime of 3-5 days with respect to wet and dry deposition.

## Introduction

Black carbon (BC) absorbs incident solar radiation, perturbs temperature gradients in the atmosphere, and indirectly impacts cloud formation and optical properties [*Koch and Del Genio*, 2010]. Deposition of BC to snow and ice surfaces alters their albedo, and enhances melt [*Hansen and Nazarenko*, 2004; *Flanner et al.*, 2007]. The impact of BC on regional and global climates through these processes depends on its atmospheric concentration, and thus on the relative rates of emission and loss. Combustion of fossil fuels and biofuel, biomass burning, and wildfires are major sources of BC [*Bond et al.*, 2004]. The only atmospheric sinks for BC aerosol are wet and dry deposition. Wet deposition occurs through scavenging by cloud droplets, ice crystals, and

[2] This chapter is published (**Journal of Geophysical Research: Atmospheres, 2018, 123, 12277**) with Ethan W. Emerson, Joseph M. Katich, Joshua P. Schwarz, Gavin R. McMeeking, Delphine K. Farmer as authors. With exception of the liquid sample analysis performed by Joseph M. Katich, all of the experimental work was performed and the paper written by Ethan W. Emerson with guidance from Delphine K. Farmer.

precipitation, while dry deposition refers to the direct removal of particles in the atmosphere to planetary surfaces (e.g. plant, soil, ocean, ice surfaces) by gravitational settling, impaction, interception, and diffusion. The relative importance of these loss processes depends on particle size, with gravitational settling affecting larger (>1 μm in diameter) particles and diffusion impacting the smaller (<300 nm) particles [*Ruijrok et al.*, 1995]. *Bond et al.* [2013] and references therein demonstrate clear constraints on the sources, aging, and optical properties of BC, yet direct constraints on deposition losses are still needed. Removal rates of refractory and non-refractory sub-micron aerosol by wet and dry deposition are one of the most uncertain aspects of modelling cloud condensation nuclei (CCN; *Lee et al.,* [2013]). BC is an ideal tracer for particle deposition because it is non-volatile and effectively chemically inert, although it becomes internally mixed with other aerosol species in the atmosphere; still, BC is insoluble in water and has no confounding gas-phase contribution to precipitation measurements, enabling its use to examine the relative importance of wet and dry deposition. Thus, measurements of BC deposition are not only essential for constraining BC sinks and atmospheric lifetime, but also useful for investigating aerosol deposition more broadly.

The accuracy of BC dry deposition in climate simulations is particularly important in regions with high snow and ice cover due to its albedo impacts. BC deposition to snowpacks is linked to accelerated snowmelt in the Himalaya, Cascades, and Sierra Nevada mountains – thus affecting water supplies for agriculture and population centers [*Menon et al.*, 2010; *Yasunari et al.*, 2013; *Kaspari et al.*, 2015]. The current inability of climate researchers to accurately predict BC concentrations in or on snow surfaces, and subsequent impacts on albedo, temperature, and snowmelt, are directly linked to poor parameterizations of BC dry deposition and a lack of deposition measurements. For example, *Huang et al.* [2010] showed that alterations for dry

deposition over the base model is essential to correctly model surface BC concentrations. Furthermore, the use of an unaltered dry deposition simulation underestimated surface BC by a factor of at least 2, and more often >5 [*Huang et al.,* 2010] using the size-resolved resistance-in series approach developed by *Zhang et al.* [2001]. This dry deposition parameterization has never been tested against BC deposition measurements.

Current methods can quantify wet deposition of BC (e.g. [*Ohata et al.*, 2013]), but there is a lack of methodology to directly measure dry deposition of BC with adequate time or size resolution to evaluate parameterization schemes. Indirect measurements [*Spackman et al.*, 2010], including those made by collecting particles on artificial surfaces, do not necessarily represent terrestrial surfaces and may not accurately capture surface-atmosphere exchange properties [*Ogren et al.*, 1984; *Dasch and Cadle*, 1989]. Bulk measurement of deposition on snow surfaces approximates dry deposition but lacks the aerosol size resolution to fully evaluate parameterizations. Furthermore, both methods lack sufficient time resolution to capture changes in atmosphere turbulence parameters (e.g. friction velocity), which are key components in dry deposition parameterizations. Micrometeorological techniques show more promise for surface-atmosphere exchange measurements. Here, we extend established eddy covariance flux techniques [*Lee et al.*, 2005] by using a single particle soot photometer (SP2) to measure fluxes of refractory black carbon over a grassland in the United States, and compare these exchange measurements with wet deposition collected simultaneously from precipitation.

## Methods

### *Site & Instrumentation*

The Black Carbon Aerosol Deposition Study (BCADS 2017) took place at the Department of Energy Atmospheric Radiation Measurement Southern Great Plains (SGP) site in

Lamont, Oklahoma, USA, (36° 36’ 18’’ N, 97° 29’ 6’’ W; 312 m above sea level) from 12 June to 19 July 2017. SGP is a well-known site, and has been described elsewhere [*Fischer et al.*, 2007; *Riley et al.*, 2009; *Sisterson et al.*, 2016]. The fields to the south and west of the site were planted with alfalfa (*medicago sativa*) which was swathed 5 June and 18 June, and grew to a height of 36 cm at the time of the second swathing. Thus, our canopy varied from near zero to 36 cm over the course of the campaign and had an estimated roughness length of 0.01to 0.04 m. No direct measurements of leaf area index were collected, but they typically range from 1-5 depending on the crop, season, and year [*Fischer et al.*, 2007].

Figure 2.1 shows relevant meteorological parameters; temperatures varied between 25 °C and 35 °C and the total precipitation recorded during the campaign was 148.5 mm over 8 events. A sonic anemometer (Gill Instruments, WindMaster Pro) and inlet were located 2.7 m above ground level on the SGP ECOR 14 ($CO_2$ flux) tower. Instruments were housed in a temperature controlled enclosure at the base of the tower. Despite the temperature control, the enclosure temperature would exceed the threshold for the SP2 and the laser would occasionally shut off during the hottest parts of the day, limiting data collection during these periods. The inlet was aligned downward (45°±15º angle) and located below the center of the sonic anemometer (~40 cm vertical and ~20 cm horizontal displacement). The inlet was 4.5 m of 4.3 mm inner diameter stainless steel with a wire mesh screen to exclude insect and debris contamination and insulated from direct sunlight with pipe foam. Bends were minimized to reduce line losses. A bypass pump coupled to a mass flow controller maintained turbulent flow (~12 L $min^{-1}$; Re≈3000; residence time of 0.9 s). Particle transport losses in the bypass system are estimated to be <5% for the size range measured by the SP2 (70-600 nm), laminar flow within the internal SP2 tubing was maintained.

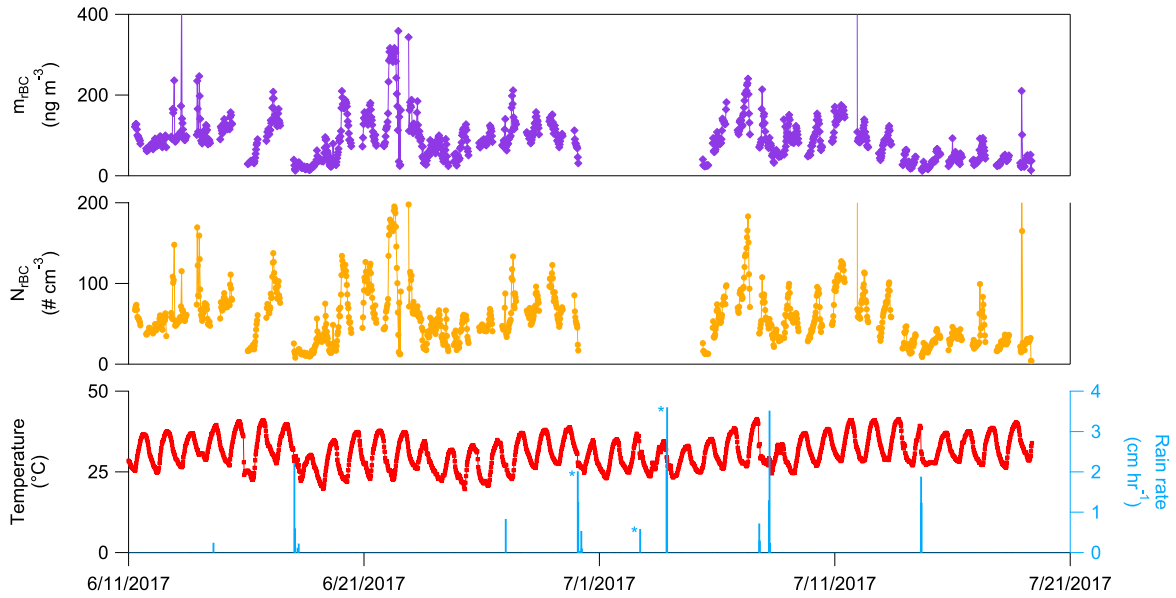


**Figure 2.1**: Campaign overview of rBC mass ($m_{rBC}$), particle counts ($N_{rBC}$), and meteorological parameters. rBC mass and particle counts represent 30-minute averages. Precipitation was collected during rain periods marked with an (*).

*Single Particle Soot Photometer*

rBC was measured with a SP2 (8 Channel, Model D, Droplet Measurement Technologies, Inc., Longmont, CO) [*Stephens et al.*, 2003; *Schwarz et al.*, 2006]), which measures rBC in individual particles by quantifying the thermal visible radiation they emit after being heated to vaporization by a 1064 nm continuous intracavity laser beam. rBC, the accepted term for SP2's data products, is experimentally equivalent to elemental carbon at the level of 15% [*Kondo et al.*, 2012; *Petzold et al.*, 2013]. The SP2 was calibrated by measuring the instrument response to mobility-selected fullerene soot (Alfa Aesar 40971, Lot: W08A039) converted to mass values using effective density data provided by [*Gysel et al.*, 2011]. We related the W08A039 lot to the previously characterized FS12S011 lot (e.g. *Moteki and Kondo*, 2010; *Gysel et al.*, 2011; *Laborde et al.*, 2012) using a linear parameterization. The SP2 is extremely sensitive and selective to a single particle's rBC mass ($m_{rBC}$), but insensitive to particle mixing state and morphology [*Cross et al.*, 2010]. High frequency variability in particle concentrations can be detected by the SP2, allowing for eddy covariance flux calculation [*Lee et al.*, 2005; *Burba and D.J.*, 2010].

Here we calibrate rBC in the mass range 0.3-50 fg, corresponding to 70-600 nm mobility diameter (70-380 nm volume equivalent diameter). This covered 95% and 45% of the accumulation mode of $m_{rBC}$ and $N_{rBC}$, respectively, in this one mode, based on a lognormal fit to the distributions (Figure 2.11). Volume equivalent diameters over the 70-600 nm range are considered viable. Significant deviation from a lognormal distribution is observed for $m_{rBC}$ below 60 nm, indicating a loss of counting efficiency. Thus, we consider particles above 70 nm to be appropriately quantified for $m_{rBC}$ and infer $N_{rBC}$ based on the number of detection events with the 70-600 nm volume equivalent diameter.

*Wet Deposition*

Three wet deposition samples were collected using an N-Con Systems Co. Inc. Atmospheric Deposition Sampler. Rain rates were measured using a weighing bucket precipitation gauge [ARM Climate Research Facility, Weighing Bucket Precipitation Gauge]. Following a rain event, samples were collected in glass vials and stored at 4 °C. Liquid samples were sonicated briefly, which increased measured concentrations by ~50%, and aerosolized with a carefully characterized nebulizer (a CETAC Marin-5, as described in Katich et al., 2017), before sampling the resulting aerosol with an SP2. This technique has been applied to rain, snow, and ice samples [*Ohata et al.*, 2011; *Schwarz et al.*, 2012].

*Eddy Covariance Measurements*

The eddy covariance flux technique directly measures a species' surface-atmosphere exchange. The eddy covariance vertical flux ($F_c$) for a given scalar crossing the measurement plane of a horizontally homogenous area (e.g. prairie grassland) is determined by the covariance of the vertical windspeed (w) and scalar (*c;* e.g. species mixing ratio or particle concentration) [*Baldocchi et al.*, 1988]

$$F_c = \overline{\langle w'c' \rangle} = \frac{1}{n}\sum_{i=0}^{n}(c_i - \bar{c})\ (w_i - \overline{w}) \tag{2.1}$$

where $n$ is the number of points used in the calculation, $w_i$ and $c_i$ are instantaneous measurements of vertical windspeed and scalar (e.g., $m_{rBC}$) respectively, and $\overline{w}$ and $\overline{c}$ are the mean vertical windspeed and scalar measurement. Eddy covariance flux measurements are typically calculated over 30-minute intervals. The exchange velocity ($V_{ex}$) is determined from the flux and mean concentration over the flux period as:

$$V_{ex} = \frac{F_c}{\bar{c}} \tag{2.2}$$

A negative $V_{ex}$ (or $F_c$) indicates deposition and a positive $V_{ex}$ (or $F_c$) indicates emission. Furthermore, we note that deposition velocity is described by $V_{dep}$=-$V_{ex}$.

*Data Treatment*

High resolution particle-by-particle data is aggregated to a 0.1 s time grid spanning the campaign. Particle number ($N_{rBC}$) is simply the total counts and particle mass ($m_{rBC}$) is the sum of masses occurring within 0.05 s before and after the grid point. Concentrations are determined using 1 s averaged flow rates measured by a differential pressure transducer and then converted to standard units using the on-board pressure and temperature measurements. Sonic anemometer data was recorded at 10 Hz on the same computer as rBC data eliminating the need to adjust digital clocks. These data are gridded to the same particle time grid.

*Flux Approach & Calculations*

Flux periods are determined based on the flow controller set point changes, which occurred every 30 minutes throughout the campaign. Preliminary data control excluded periods when laser power was changing (typically laser power scans) and times when the measured flow rates varied significantly (3x set point). A total of 905, 30-minute flux periods are determined to meet data control standards.

We calculate eddy covariance fluxes of both $m_{rBC}$ and $N_{rBC}$, including corrections to temporally align the wind to account for sonic rotation, rBC concentration in standard units, and storage term. consider the effects of sensor separation and attenuation. Data are filtered for stationarity (±30%), friction velocity ($u_*$ > 0.15 m $s^{-1}$), wind direction (exclude tower and building impacts) and precipitation (exclude rain events) using the following procedure:

1. Calibration of SP2 for particle mass; described above Methods (I) and correction of vertical windspeed per technical note KN1509v3.
2. Timelag correction: We adjust the data for the timelag between the sonic and SP2 instrument. We compare two approaches to timelag correction: (1) a calculated timelag using the flow rate through the inlet tubing (Fix or Fixed), and (2) using an autocorrelation analysis (Max; [*Farmer et al.*, 2006; *Nemitz et al.*, 2008]). Fixed lag times typically underestimate flux measurements because lag times are not always constant (due to variations in pumping speed and changes in air density; [*Langford et al.*, 2015]). However, autocorrelation analysis of noisy data is limited by counting statistics, and can lead to flux overestimation because it systematically maximizes the flux [*Taipale et al.*, 2010; *Langford et al.*, 2015]. We use both approaches (Fix and Max) to determine a lower and upper bound for flux (and thus $V_{ex}$) measurements. During BCADS 2017, the calculated lag time is 0.9 s.
3. Sonic rotation: We applied a two-dimensional rotation to windspeed in three axes to account for the sonic anemometer not being precisely level with the ground, and for slope effects in the surrounding area [*Massman*, 2000; *Wilczak et al.*, 2001; *Lee et al.*, 2005].
4. Flux calculation (Equation 1)

*Quality Control*

(a) Stationarity test, (b) wind direction, (c) U*, and (d) precipitation events. Quality filters resulted in N=398 and N=271 flux periods for mass and particle counts, respectively.

(a) The stationarity test is applied to meet the requirement that calculated fluxes do not vary within the time-scales of analysis and is computed by comparing 5-minute fluxes

to the overall flux [*Foken and Wichura*, 1996]. During BCADS 2017, we found N=524 stationary periods for $m_{\mathrm{rBC}}$ and N=338 for $N_{\mathrm{rBC}}$.

$$0.7 < \frac{\overline{\langle w'c' \rangle}_{5\ min}}{\overline{\langle w'c' \rangle}_{30\ min}} < 1.3 \tag{2.3}$$

(b) Flux periods where the average wind direction is obstructed by the sampling tower or passes through the SGP ARM site are excluded (N=38).

(c) Periods with low friction velocity ($U^* < 0.15$ m s$^{-1}$; N=243) are excluded [*Papale et al.*, 2006].

(d) Precipitation events (8 in total; impacting N=5 flux periods) are excluded from the general analysis, but fluxes during periods of rain are considered and discussed.

*Corrections*

We consider the following corrections that can be applied to eddy covariance particle data: (a) storage (b) time response, (c) sensor separation, (d) tube attenuation, (e) Webb-Pearman-Leuning (WPL), (f) de-spiking, (g) de-trending. The storage correction is found to be significant and is thus included in our analysis. All remaining corrections are neglected from presented data, but we note the magnitude of error these could contribute.

(a) Under horizontally homogenous conditions the turbulent flux below the measurement height can differ. Using a 1-point storage term developed by Rannik et al. [2009]:

$$F_{storage} = \int_0^{z_r} \frac{\partial \bar{c}}{\partial t} dz \approx z_r \frac{\overline{c(t+\Delta T)} - \overline{c(t)}}{\Delta T} \tag{2.4}$$

where $c$ is the concentration and $t$=2 min with $\Delta T$=30 min. These values were calculated for all flux periods that ended within 10 seconds of the next one starting (N = 862). we estimate the storage contribution for $m_{rBC}$ and $N_{rBC}$ and to be 15% and 30% respectively, on average. This correction is included in our analysis.

(b) Time response corrections are necessary to compensate for insufficient sensor response time [*Moore*, 1986; *Massman*, 2000; *Lee et al.*, 2005]. This correction is neglected as the SP2 measures on a particle-by-particle basis and within the calibrated range the SP2 has a counting efficiency near 100%. Errors associated with missed particles are expected to be random.

(c) Sensor separation corrections are used to correct for the inability of most closed-path systems that draw from an inlet to sample from the same volume as vertical wind speed. Using formulations developed by *Kristensen et al.* [1997] we estimate the losses to be <5%. As evidenced in Figure 2.3, high frequency losses are not observed.

(d) Tube attenuation corrects for flux losses within the inlet that dampens small fluctuations. Spectral Analysis (see below) show that attenuation does not occur substantially at high frequencies, and thus we neglect this correction.

(e) WPL correction is neglected as flow rates through the system are measured in volume, but converted to standard units using high-speed on-board measurements of temperature and pressure.

(f) De-spiking is neglected because a small number of particles are sampled over 100 ms and are also not necessarily continuous; thus particle flux measurements are usually limited by counting statistics [*Nemitz et al.*, 2008; *Pryor et al.*, 2008a]. Furthermore, particle size impacts the flux measurement as larger particles carry the bulk of the particle mass but

are limited in number. *Nemitz et al.* [2008] describe how these large particles appear as spikes in 100 ms resolution time series and contribute a real flux and should not be removed by a de-spiking routine.

(g) No de-trending method is applied to this dataset because de-trending techniques typically result in a loss of flux and are usually required for situations where the meteorology is changing rapidly [*Moncrieff et al.*, 2004]. Periods of distinct meteorology (rain events) and non-stationary flux periods are already removed and this correction would be minimal.

*Flux Uncertainty*

We examine two sources of uncertainty affecting our flux measurements, and report data for only flux periods meeting quality control metrics. Uncertainty can be associated with counting discrete particles ($N_{\mathrm{rBC}}$), measurement of particle mass ($m_{\mathrm{rBC}}$), instrument noise, and the measurement of covariance. Flux uncertainty $\Delta F_{N_{rBC}}$ caused by counting statistics for a single 30-minute period is expressed as:

$$\Delta F_{N_{rBC}} = \frac{\sigma_w \bar{c}}{\sqrt{N}} \tag{2.5}$$

where N is the cumulative number of particles counted in the 30-minute period [*Fairall*, 1984; *Nemitz et al.*, 2008]. For these data, $\Delta F_{N_{rBC}} = 0.02 \ \#\ cm^{-2}s^{-1}$.

Various methods exist that quantify the uncertainty of covariance between vertical wind speed and scalar (e.g. *Wyngaard*, 1973; *Lenschow and Kristensen*, 1985; *Wienhold*, 1995; *Mahrt*, 1998; *Finkelstein and Sims*, 2001) and we find them to be comparable for these data. We report the random flux errors using properties of the cross covariance function of a single flux

measurement from the baseline fluctuation (standard deviation; $\sigma_{f(w'c')}$) in a cross covariance function (f) between vertical windspeed (w) and scalar (c) at lag times significantly longer than the delay time (±Γ where Γ= 50 s to 80 s) [*Wienhold*, 1995; *Spirig et al.*, 2005]. We calculate the detection limit of a single flux measurement ($LOD_\sigma$) as $3 \times \sigma_{f(w'c')\,[-\Gamma,+\Gamma]}$ [*Langford et al.*, 2015]. For these data, $\sigma_{f(w'N'_{rBC})} = 0.08\ \#\ cm^{-2}s^{-1}$ and $\sigma_{f(w'm'_{rBC})} = 0.25\ ng\ m^{-2}s^{-1}$.

We further estimate the flux uncertainty due to instrument noise $\delta F_{noise}$ as described by [*Billesbach*, 2011]:

$$\delta F_{noise} = \frac{1}{M}\sum_{j,k=1}^{M} w'(t_j)c'(t_k) \tag{2.6}$$

where w' and c' are deviations from the mean of vertical windspeed (w) and scalar (c) normalized by the number of measurements (M) within the averaging interval, and the time indices j and k, where k is the index of the randomized time series. For these data, $\delta F_{N_{rBC},noise} = 0.05\ \#\ cm^{-2}s^{-1}$ and $\delta F_{m_{rBC},noise} = 0.2\ ng\ m^{-2}s^{-1}$.

Lastly, we calculate the signal to noise ratio (SNR) of $m_{rBC}$ or $N_{rBC}$ collected by the SP2 during a flux period using the following equation:

$$SNR_i = \frac{\mu_i}{\sigma_{i,zero}} \tag{2.7}$$

where $i$ is either $m_{rBC}$ or $N_{rBC}$ and μ is the mean concentration during a measurement period and $\sigma_{zero}$ is the standard deviation of that signal when air is sampled through a HEPA filter placed at the inlet of the system (system zero). For these data, $SNR_{N_{rBC}} = 60000$ and $SNR_{m_{rBC}} = 130$.

*Flux Limit of Detection*

We determine a limit of detection of a given flux period ($LOD_i$) as described by Langford et al., 2015:

$$LOD_i = \alpha * RE_i \tag{2.8}$$

where α is a specified confidence interval (α = 3 for the 99$^{th}$ percentile) and $RE_i$ is the random error for the flux period (described above). We aggregate the $LOD_i$ data (of quality controlled data) to determine an average campaign limit of detection ($\overline{LOD}$).

$$\overline{LOD} = \frac{1}{N}\sqrt{\sum_{i=1}^{N} LOD_i^2} \tag{2.9}$$

Averaged over the entire field project, $\overline{LOD}_{N_{rBC},F} = 0.06\ \#\ cm^{-2}s^{-1}$ and $\overline{LOD}_{m_{rBC},\ F} = 0.06\ ng\ m^{-2}s^{-1}$, although we note that the LOD for individual flux periods at 1σ ranges from 0-0.5 $ng\ m^{-2}s^{-1}$ and 0-0.43 $\#\ cm^{-2}s^{-1}$. The same method was applied to determine a $V_{ex}$ limit of detection $\overline{LOD}_{N_{rBC},V_{ex}} = 0.5\ mm^{-2}s^{-1}$ and $\overline{LOD}_{m_{rBC},V_{ex}} = 0.6\ mm^{-2}s^{-1}$. These $\overline{LOD}$ values result in N=312/374 for $m_{rBC}$ and N=93/256 for $N_{rBC}$

Table 2.1: All flux data is in units of ng $m^{-2}s^{-1}$ and # $m^{-2}s^{-1}$ for $m_{rBC}$ and $N_{rBC}$, respectively. Units for all other data is specified.

| | SNR | $\Delta F_{N_{rBC}}$ | $\delta F_{noise}$ | $\sigma_f$ | $\overline{LOD}_F$ | beyond $\overline{LOD}_F$ | $\overline{LOD}_{V_{ex}}$ | beyond $\overline{LOD}_{V_{ex}}$ |
|---|---|---|---|---|---|---|---|---|
| units | a.u. | [ng or #] $m^{-2}s^{-1}$ | | | | # | $mm^{-2}s^{-1}$ | # |
| $m_{rBC}$ | 130 | n/a | 0.2 | 0.25 | 0.06 | 312/374 | 0.6 | 334/374 |
| $N_{rBC}$ | 60000 | 0.02 | 0.05 | 0.08 | 0.06 | 93/256 | 0.5 | 193/256 |

*Wet Deposition Flux*

The rBC concentration of three rain collected rain events is determined and based on the rainfall during the event. A wet deposition flux is determined following *Mori et al.* [2014]. For each event, the concentration of rBC $C_{rBC_{precip}}$ is determined in $ng_{rBC}\ g_{H2O}^{-1}$. This mass loading is scaled by the amount of precipitation collected ($P_e$) in the event (mm) to calculate the flux per event ($ng\ m^{-2}\ event^{-1}$).

$$F_{rBC_{precip}} = C_{rBC_{precip}} \times P_e \tag{2.10}$$

Each event flux is weighted by *R*, the fractional contribution of the measured rain (in the event) to the total rain during the campaign (= $P_e/P_{total}$). An average flux is derived by averaging the weighted event flux of the 3 rain events by the campaign duration (h) (details in Table 1.1). This method effectively represents the flux if each rain event represented the entire campaign. The Mori et al. (2014) method results in a value that is within the standard deviation of the 3 rain events.

**Method Validation**

To demonstrate the ability of the SP2 to measure $m_{rBC}$ and $N_{rBC}$ fluxes, we use three approaches: (1) spectral analysis to demonstrate that the SP2 meets the instrumental requirements for eddy covariance flux measurements; (2) quantitative constraints on uncertainty and detection limits; and (3) internal comparison of $m_{rBC}$ and $N_{rBC}$ fluxes.

*Instrument Response Time*

As described previously, instruments used for eddy covariance flux analysis must be both fast and sensitive on the timescale of turbulent eddies. Figure 2.2 shows a signal that is clearly distinguishable over the system background. System background is determined by a 30-minute period where air is drawn through a HEPA filter placed at the inlet of the entire system. As

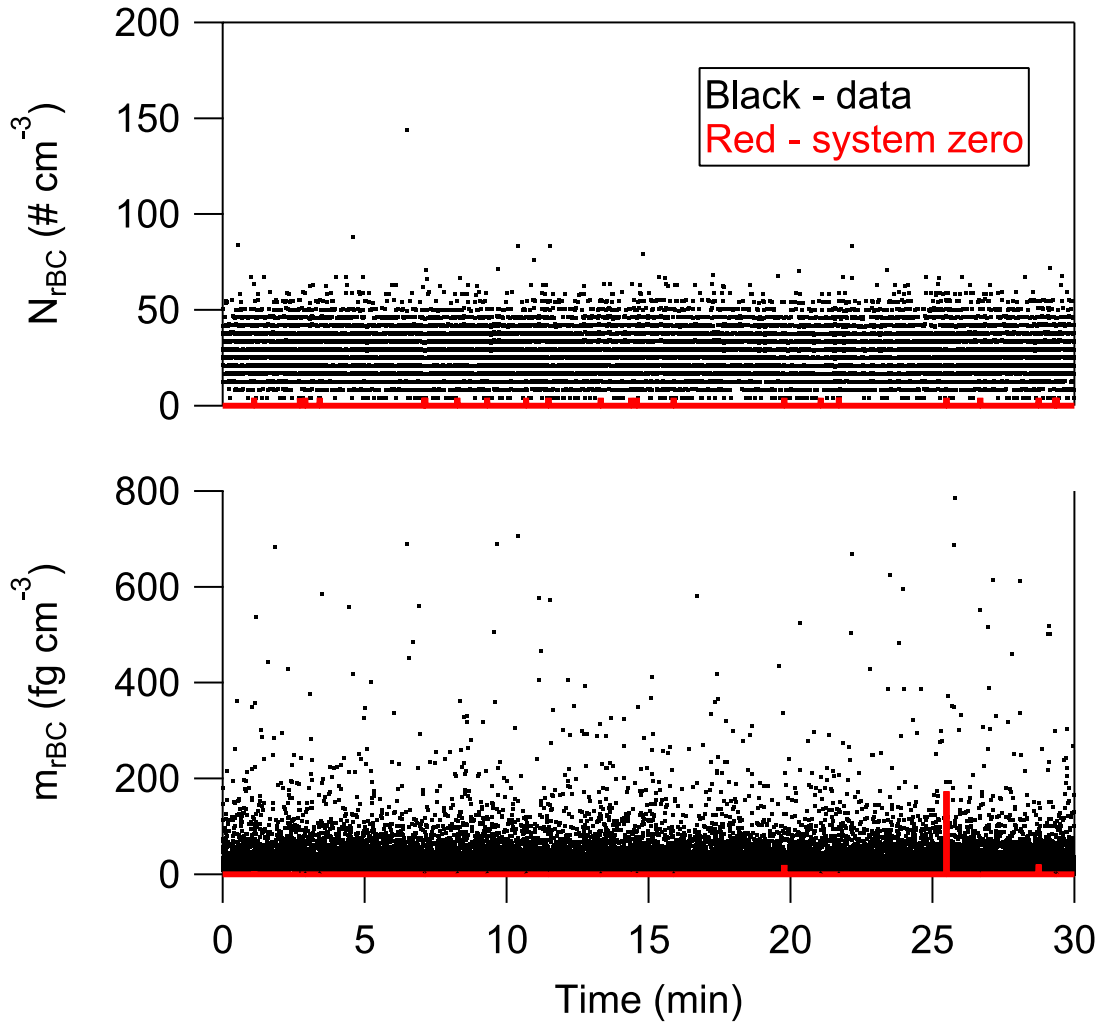


**Figure 2.2**: An example 30-minute high time-resolution $m_{rBC}$ and $N_{rBC}$ particle data (black) with 30-minute system zero data from the adjacent half-hour.

mentioned previously, the average SNR for $m_{rBC}$ and $N_{rBC}$ are is more than 100. Concentrations have a strong diel trend, but did not typically vary significantly over the course of 30 minutes. However, an instrument with a good signal to noise ratio is not necessarily inherently suitable for eddy covariance flux analysis.

*Spectral Analysis*

The eddy covariance method requires sufficiently fast sensor response, adequate integration time, and sensitive measurements. These requirements are validated by spectral analysis (Figure 2.3), in which the cospectra of vertical wind speed and rBC measurement ($m_{rBC}$ or $N_{rBC}$) are compared to the simultaneously measured sensible heat flux. Ensemble flux data for quality controlled data show a $(f)^{-7/3}$ response between 0.3 Hz and 3 Hz, characteristic of the inertial sub-range predicted from Kolmogorov theory [*Kaimal and Finnigan*, 1994] and demonstrates a sufficiently fast senor response time to measure eddy covariance fluxes [*Baldocchi et al.*, 1988]. Both $m_{rBC}$ and $N_{rBC}$ follow the sensible heat cospectrum, implying that scalar transport occurs by the energy-transporting eddies. The lack of spectral attenuation (i.e. steeper slope at high frequencies) indicates no flux underestimation due to high-frequency damping within inlet lines, and that the instrument has a sufficiently fast response for eddy covariance flux measurements.

Cumulative cospectra (Figure 2.3b) show which frequencies contribute to the total flux and demonstrates sufficiently long integration times. At low frequencies cumulative cospectra for all measured scalars are near unity, implying a sufficiently long integration time. Cospectra of sensible heat show a clear leveling off at the highest frequencies measured indicating that the measurement is fast enough to capture the smallest energy transporting eddies. Both $m_{rBC}$ and

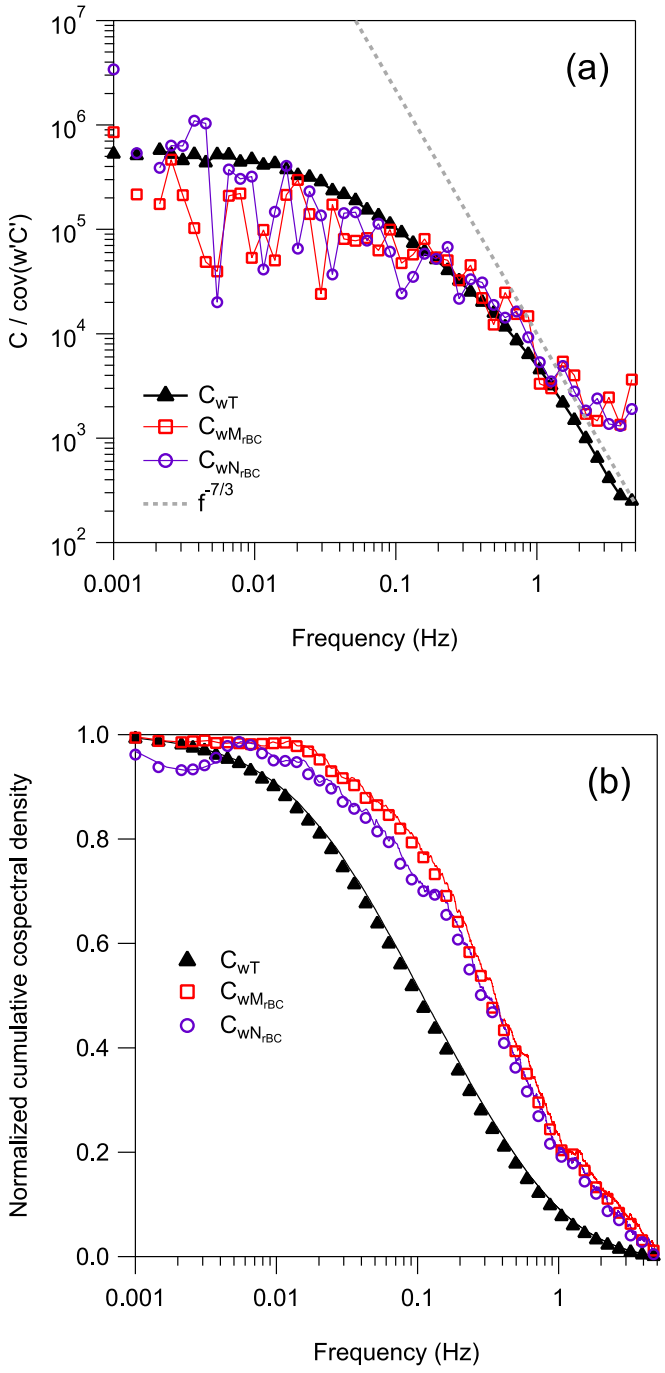


**Figure 2.3**: (a) covariance normalized cospectral density of $m_{rBC}$ (red open squares)) $N_{rBC}$ (purple open circles) and temperature (black closed triangles). Data represents ensemble medians of quality controlled flux periods binned into 35 evenly-space logarithmic bins. Any negative values are shown as positive after all manipulations. (b) cumulative cospectral density plot for data presented in (a).

$N_{rBC}$ trend with sensible heat, but do not flatten at the highest frequencies. Fitting these curves to a Hill function, we estimate 5-10% loss occurring at high frequencies.

*Quantitative Constraints on Uncertainty and Detection Limits*

Various sources contribute to uncertainty for particle eddy covariance measurements. The number of particles sampled in 100 ms is typically small; as such, particle measurements are typically limited by counting statistics [*Nemitz et al.*, 2008; *Pryor et al.*, 2008b]. Additionally, particle size impacts the uncertainty as larger particles carry most of the measured mass [*Jimenez*, 2003]. De-spiking routines are typically omitted due to the inherent noise observed in particle measurements. As mentioned above, we employed a method developed by Wienhold et al. (1995) to determine the uncertainty of a flux measurement from baseline fluctuations at time lags significantly longer than the prescribed lagtime. The uncertainty for neither $m_{rBC}$ nor $N_{rBC}$ fluxes is constant across the campaign and increase quadratically with the flux magnitude. Furthermore, these errors follow a power law relationship with higher friction velocity, and are consistent previous observations [*Farmer et al.*, 2011] and theoretical considerations showing that concentration measurement precision must be higher during more turbulent conditions [*Fairall*, 1984; *Rowe et al.*, 2011]. These behaviors suggest increased mixing or inefficient scavenging by terrestrial surfaces. Because of these observations, it is necessary to consider ensemble averages for scientific interpretation. Specifically, we interpret data that is beyond the $\overline{LOD}_F$ or $\overline{LOD}_{V_{ex}}$ despite that the singular data may not be above the $LOD_i$ for that specific data point (i.e. the uncertainty for that $i^{th}$ point includes zero).

*Internal Comparisons*

Fluxes of $m_{rBC}$ and $N_{rBC}$ are not always consistent, and bifurcate (i.e. $m_{rBC}$ and $N_{rBC}$ fluxes in opposite directions) 43% of the time. The remaining 57% behave consistently. No statistically

significant trend between deviating fluxes and any measured external parameter (i.e. wind direction, $u_*$, rBC concentration, etc.). Upwards particle fluxes are not an uncommon observation (e.g. [*Pryor et al.*, 2008c]) however, bifurcated fluxes of particle counts vs particle mass is novel. Quadrant analysis indicates that different micrometerological events coupled with changes in particle concentrations lead to apparent upward fluxes. Bifurcated fluxes are more surprising, however, considering that particle mass and particle number concentration can be decoupled. For example, a gradient with more smaller particles near the ground than above the sensor, but fewer larger particles near the ground than above the sensor could cause an apparent upward flux in particle number and an apparent downward flux in particle mass. In contrast, consistent $m_{rBC}$ and $N_{rBC}$ fluxes indicate both small and large particles have consistent vertical gradients. An eddy can thus carry $m_{rBC}$ fluxes upwards while simultaneously having a downward $N_{rBC}$ flux.

**Observations and Discussion**

*Refractory Black Carbon Fluxes*

Concentrations of $m_{rBC}$ and $N_{rBC}$ (Figure 2.1) are representative of a remote North American field site away from major anthropogenic influences [*Koch et al.*, 2009]. During BCADS 2017 the geometric mean ($\mu_g$) with a geometric standard deviation ($\sigma_g$) for $m_{rBC}$ and $N_{rBC}$ concentrations are $\mu_g$ = 56 ($\sigma_g$= 3.0) ng $sm^{-3}$ and $\mu_g$ = 46 ($\sigma_g$= 2.2) # $sccm^{-3}$. These concentrations follow a diel cycle (Figure 2.4) consistent with regular boundary layer expansion observed at the site (Figure 2.8). $m_{rBC}$ and $N_{rBC}$ concentrations hade a consistent daily range throughout the campaign until the last week (11-July to 19-July), when concentrations decreased. Complete campaign data of $m_{rBC}$ and $N_{rBC}$ fluxes is shown in Figure 2.5. Variability in these data is clearly observed. While the magnitude of a single flux measurement does not always exceed

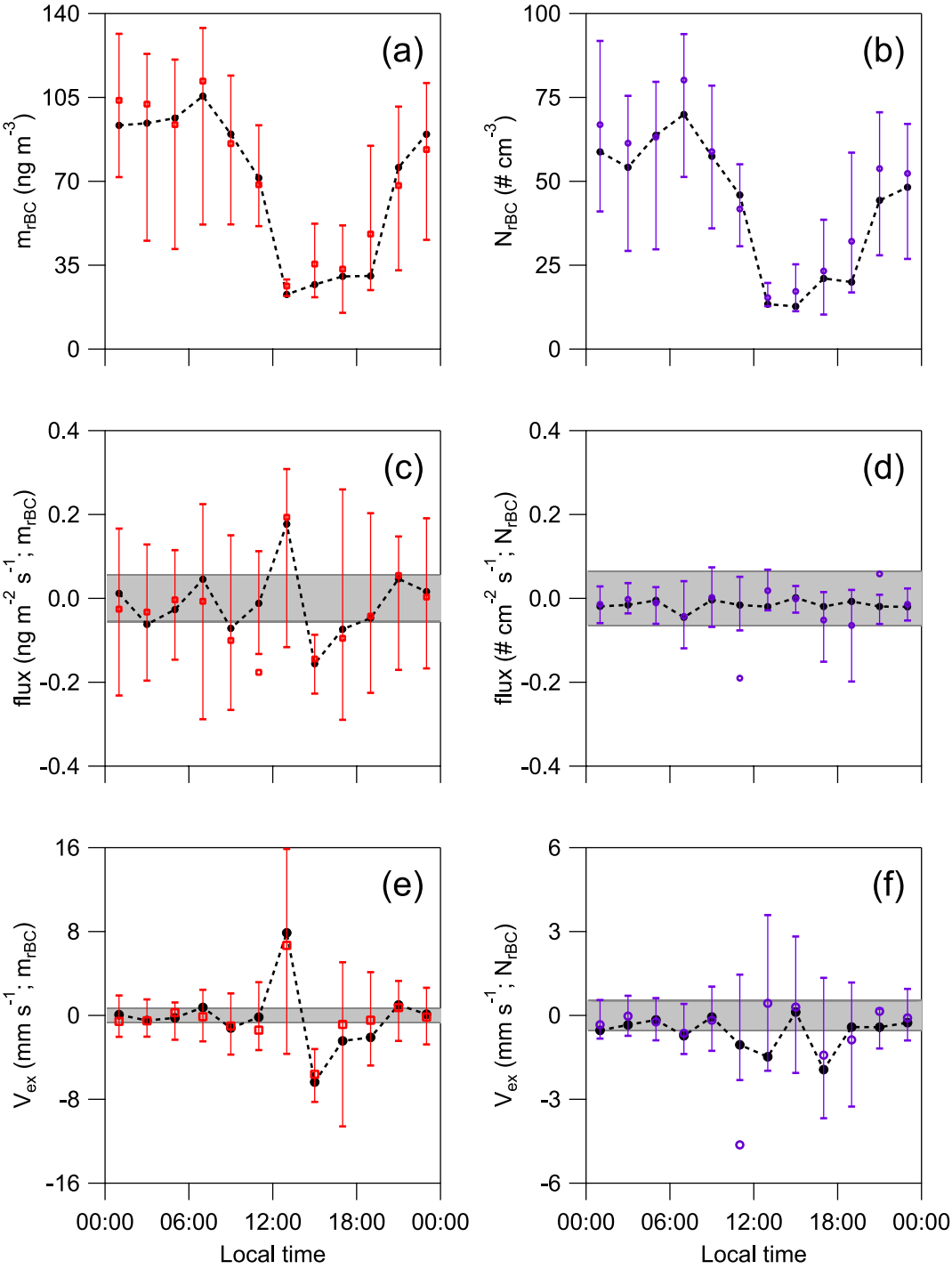


**Figure 2.4**: Bi-hourly binned data of $m_{rBC}$ (left) and $N_{rBC}$ (right). Plots of concentration (top), flux (middle), and $V_{ex}$ (bottom). Open symbols are averages for the bin and closed symbols with dashed lines connecting are medians. The whiskers denote the range (25$^{th}$ to 75$^{th}$ percentile) of values for a particular metric. The shaded grey denotes the limit of detection (calculation described in Methods).

the $LOD_i$ (i.e. the uncertainty of a single flux measurement encompasses zero), we include all data that meets the filtering criteria in the analysis to accurately derive the aggregate statistics. The histogram in Figure 2.5 shows the propensity for deposition occurring at the field site. The regular diel cycle of $m_{rBC}$ and $N_{rBC}$ flux (Figure 2.4c & 2.4d) corresponds to dilution caused by regular boundary layer expansion observed at the site (Figure 2.8). No daily trends associated with emission could be discerned. Moreover, as there are no direct sources within the flux footprint, observations should represent loss processes only. However, as noted above, upwards fluxes are observed and occur around noon. While boundary layer height does not drive fluxes, in-mixing of lower loadings from the free troposphere could create an apparent upward flux. Thus, a flux period in which downdrafts containing particle depleted air (i.e. entrainment processes) would have an upward flux. Such effects have been noticed for particle fluxes [*Pryor et al.*, 2008c; *Nilsson et al.*, 2016]. Enhanced downward fluxes in the mid-afternoon are likely a result of increased atmospheric turbulence and friction velocity (Figure 2.9). $V_{dep}$ increases with $u_*$, but the correlation is inadequate to establish a parameterization ($r^2 \approx 0.2$ for both mass and counts). Nighttime fluxes are relatively small and bi-directional because of a relatively shallow and stagnant nocturnal boundary layer. Because these measurements approach the limit of detection for eddy covariance flux analysis, the analysis is very sensitive to minor changes in concentration that are associated with boundary layer dynamics.

The net flux and thus exchange velocity for $m_{rBC}$ and $N_{rBC}$ is near zero; $-0.3 \pm 0.2$ mm $s^{-1}$ and $-0.4 \pm 0.2$ mm $s^{-1}$ for $m_{rBC}$ and $N_{rBC}$, respectively. For the average horizontal windspeed and rBC particle diameter at SGP, the implied net deposition is slower than size resolved parameterizations developed by Zhang et al. (2001). These values imply a longer lifetime than

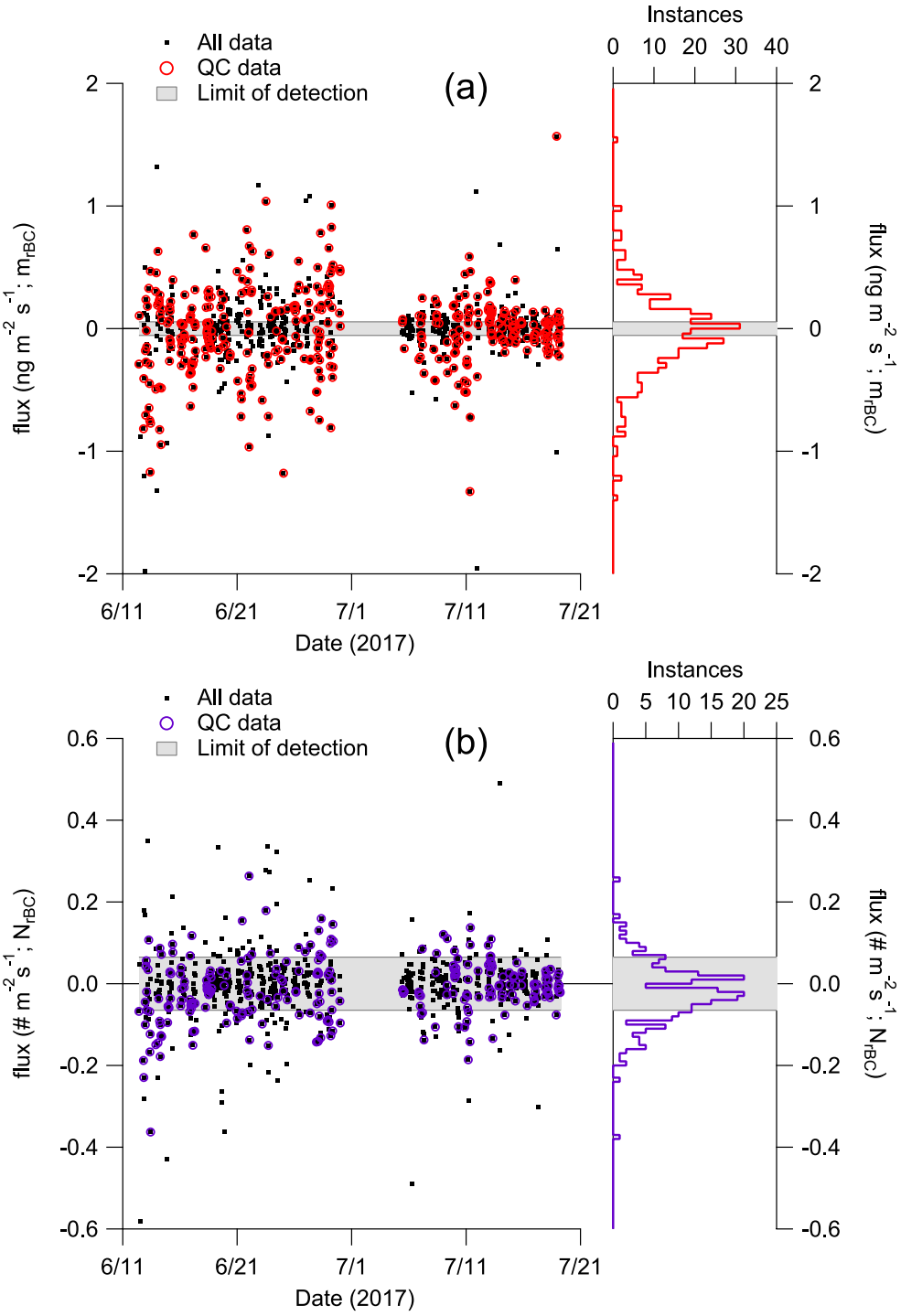


**Figure 2.5**: Campaign time series of $m_{rBC}$ (a) and $N_{rBC}$ (b) fluxes for all data (solid symbols) and quality controlled data (open symbols) with the associated uncertainty for each measurement. Binned data is shown on the right panel for each plot with the associated LOD shown in grey across the entire time series.

current understanding. However, it is likely that a different process is causing the apparent upward fluxes for rBC, as no known sources exist within the footprint sectors. Considering periods of time when deposition is dominant, the $V_{ex}$ is -3.7 ± 0.3 mm $s^{-1}$ ($m_{rBC}$) and -1.5 ± 0.3 mm $s^{-1}$ ($N_{rBC}$). Comparisons to the Zhang et al. (2001) model finds these values to be more similar. Figure 2.5 shows the diel trends of concentration, flux and $V_{ex}$. Generally, there is bidirectional exchange occurring throughout the nighttime hours, followed by an apparent upward exchange around noon. Deposition is more pronounced in the afternoon for $m_{rBC}$ than $N_{rBC}$, but the afternoon hours correspond to more deposition periods than other times of day.

Two distinct modes are apparent in the histogram of $V_{ex}$ and imply a loss process (deposition) and emission process (Figure 2.6). The observable dip at zero exchange velocity further suggests that despite being near the limit of detection these fluxes are real and not simply noise. Deposition of $N_{rBC}$ is a tighter distribution than $m_{rBC}$, and this discrepancy suggests that particles of different masses deposit and different rates. This observation is consistent with larger particles carrying the bulk of the total measured mass.

*Wet and Dry rBC Deposition*

Eight major precipitation events were observed during BCADS 2017 totaling 148.5 mm of rain [ARM Climate Research Facility, Weighing Bucket Precipitation Gauge]. This period was climatologically representative of historical averages for June and July in this region. It is expected that rBC washout occurs during or immediately following a rain event. However, only three precipitation events (of six with corresponding SP2 data) show a decrease of ambient $N_{rBC}$ and $m_{rBC}$ concentrations. Below-cloud washout of rBC may not be efficient, and the loss mechanism may be dominated by in-cloud scavenging. This further implies that rBC measured in

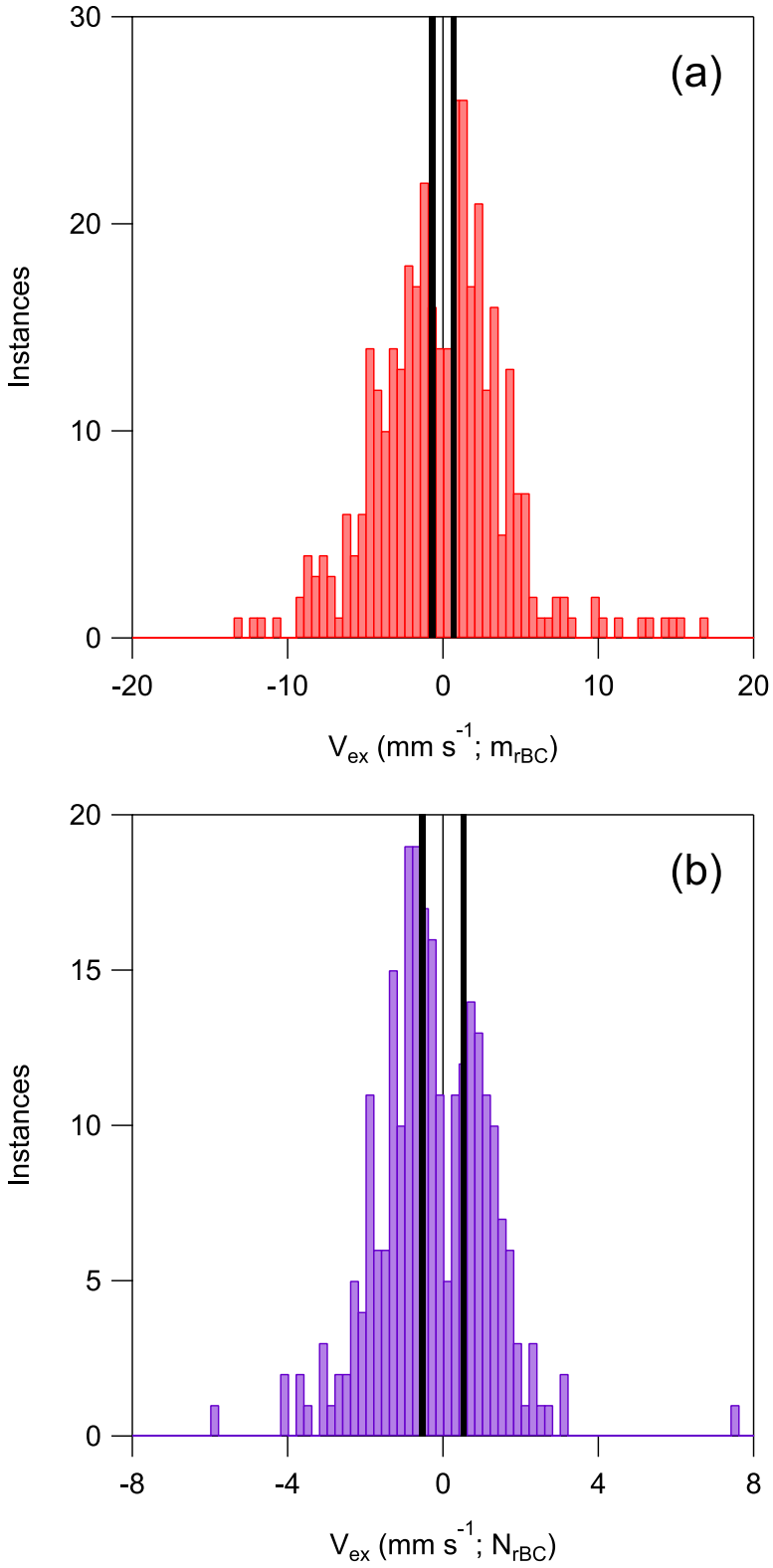


**Figure 2.6**: Histogram of $m_{rBC}$ (a) and $N_{rBC}$ (b) $V_{ex}$ in mm $s^{-1}$. The limits of detection are shown as thick black lines.

precipitation is not necessarily representative of ambient rBC concentrations, as in-cloud scavenging could occur far from the measurement site. From three rain events (marked with an * in Figure 2.2), we estimate a campaign average wet deposition flux ($\bar{F}$) of 0.05 ± 0.02 mg $m^{-2}$ $day^{-1}$.

Considering all quality controlled flux periods, wet deposition dominates the overall $m_{rBC}$ flux and we find that dry deposition constitutes 5 ± 3% of total deposition. These values are on the low end of the typical 5-20% assumed in global climate models [*Koch et al.*, 2009]. As mentioned previously, upward fluxes may be a measurement artifact or driven by a different process (e.g. vertical gradients in size distributions). Omitting the upwards flux periods, we find that dry deposition may be more significant, comprising 35 ± 5% of total deposition, though we acknowledge that this value must be an upper limit as it systematically removes upward fluxes that are part of the flux uncertainty. These values are highly dependent on precipitation rates and amount. This also assumes that dry and wet deposition are loss process from the same air mass. If particles are scavenged by cloud droplets in the free troposphere, the rBC particles observed in precipitation may differ from those in the boundary layer.

Deposition velocities describe the efficiency of the loss process and allow us to estimate the lifetime of rBC with respect to wet and dry deposition (Figure 2.7). We approximate lifetimes as the time it takes a particle to deposit from the top of the boundary layer. The wet deposition velocity (10 ± 3 mm $s^{-1}$) represents a loss efficiency of rBC and assumes that the rate of loss is invariant with position within the boundary layer and other factors that influence where and the process of loss. For the net flux observed we find a much longer lifetime of 30-90 days for dry deposition for $m_{rBC}$ and $N_{rBC}$. Considering only instances of deposition we calculate lifetimes of 1-3 days for wet and 4-6 days for dry deposition (of $m_{rBC}$). These lifetimes are

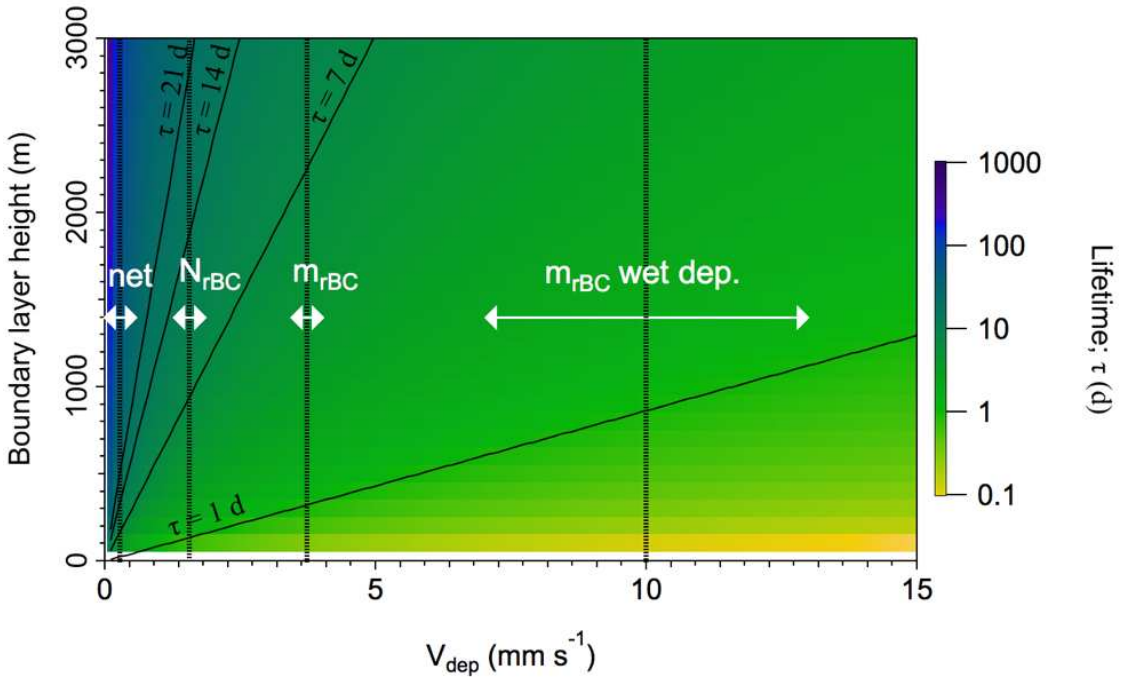


**Figure 2.7**: Comparison of rBC lifetimes for dry deposition (by mass and particle counts) and wet deposition as a function of boundary layer height and observed $V_{dep}$. We note that wet $V_{dep}$ are not true velocities, but an expression of scavenging efficiency observed during BCADS. White arrows indicate the $V_{dep}$ range and the vertical offset is the typical boundary layer height observed at SGP.

slightly shorter than the composite 5-11 days typically described in the literature [*Koch et al.*, 2009]. These observations suggest that either dry deposition is faster than model predictions, or wet deposition is less efficient than expected. While dry deposition rates are assumed to be invariant, wet deposition processes may be first order with respect to rBC burden.

Two distinct interpretations for these data exist. If we consider the upwards flux as a real process affecting rBC lifetimes, the $V_{dep}$ is 0.3 ± 0.2 mm $s^{-1}$. This average value is consistent with Wesely [1989] and more recent Arctic BC simulations with deposition velocities of 0.1 to 0.7 mm $s^{-1}$ [*Liu et al.*, 2011]. These deposition velocities correspond to an approximate 60 and 2 day lifetime to dry and wet deposition, respectively. The flux-weighted average lifetime is 5 days, where flux-weighted refers to the fractional contribution of either the dry or wet flux to the overall flux. If the upwards flux is a result of entrainment or other meteorological processes that are not representative of surface-atmosphere exchange, the deposition velocity of rBC is much faster, dry deposition represents a larger fraction of the total deposition process, and is consistent with the size resolved model developed by Zhang et al. (2001). The resulting, flux-weighted, lifetime is 3 days. Including or excluding upwards fluxes indicates the lifetime is shorter than the current understanding and is in the range of 3-5 days.

**Conclusion**

The relative importance of wet versus dry deposition depends on the amount of precipitation at a given site location and atmospheric burden. While wet deposition controls rBC lifetime, dry deposition can significantly extend the lifetime of rBC in the absence of precipitation. Furthermore, the analysis assumes wet deposition occurs throughout the boundary layer, and could vary if in-cloud scavenging dominates over below cloud impaction. In regions

or time periods of limited precipitation, the relative importance of dry deposition to aerosol lifetime will be higher.

Observed deposition velocities ($m_{rBC}$ 3.7 ± 0.3 mm $s^{-1}$ and $N_{rBC}$ 1.5 ± 0.3 mm $s^{-1}$) are consistent with current global model approaches and, to our knowledge, represent the first *in situ* measurements of rBC deposition velocities. However, we acknowledge that these observations were made at a single site over a short timeframe, and the role of surface properties, precipitation and mass loading on $V_{dep}$ warrants further investigation. *Huang et al.* [2010] and *Reddy and Boucher* [2004] employed a global annual mean BC and organic aerosol deposition velocity of 1 mm $s^{-1}$ for particle numbers in the submicron mode. Wesely [1989] used a particle number deposition velocity of 0.8 mm $s^{-1}$ over snow and ice surfaces and *Liu et al.* [2011] improved their Arctic BC simulations with number deposition velocities of 0.1 to 0.7 mm $s^{-1}$. The discrepancy in values used in cryosphere / Arctic simulations may be due to surface properties, suggesting a need for further rBC flux measurements over the cryosphere and other terrestrial or hydrological surfaces.

Additionally, these measurements represent total particle number for particles with diameter 70-600 nm. However, several widely-used particle deposition parameterizations are size-dependent, requiring size-resolved fluxes for constraint. In sufficient signal to noise environments, size-resolved measurements with the SP2 should be possible as these data show the SP2 to be adequately fast and sensitive enough for eddy covariance flux analysis of $m_{rBC}$ and $N_{rBC}$. While the total $m_{rBC}$ and $N_{rBC}$ flux is unaffected by internal mixing, size resolved measurements will require considering particle coating thickness. On the timescale of turbulent eddies (<30 minutes) $m_{rBC}$ will be unaffected by atmospheric chemistry, but coating thickness may vary due to gas-particle partitioning and in-canopy oxidation and would impact the particle

deposition rate. Size-resolved measurements will improve climate model parameterizations, but this study suggests that current models capture black carbon lifetimes and deposition rates reasonably well.

**Funding Sources, Site Staff, and Data Access**

We thank the staff at the Southern Great Plains Atmospheric and Radiation Measurement site including John Schatz, Chris Martin, Ken Teske, and Mark Smith. We also thank the DOE Office of Biological and Environmental Research for funding (grant DE-SC0016259). We would also like to thank the two anonymous reviewers whose thoughts and questions helped bring clarity to this manuscript. Data from this field campaign can be found here: https://www.archive.arm.gov/discovery/

**Chapter 2: Supplemental Information**

Table 2.1.1: Rain event data [ARM Climate Research Facility, Weighing Bucket Precipitation Gauge]. Total hours in the campaign are 1032 h and the average mass concentration is 53 ng $m^{-3}$.

| Event | Rain (mm) | rBC (ng $g^{-1}$) |
|---|---|---|
| 27-June | 5.2 | 12.8 |
| 30-June | 24.1 | 20.5 |
| 3-July | 3.6 | 11.8 |
| Total | 148.5 | - |

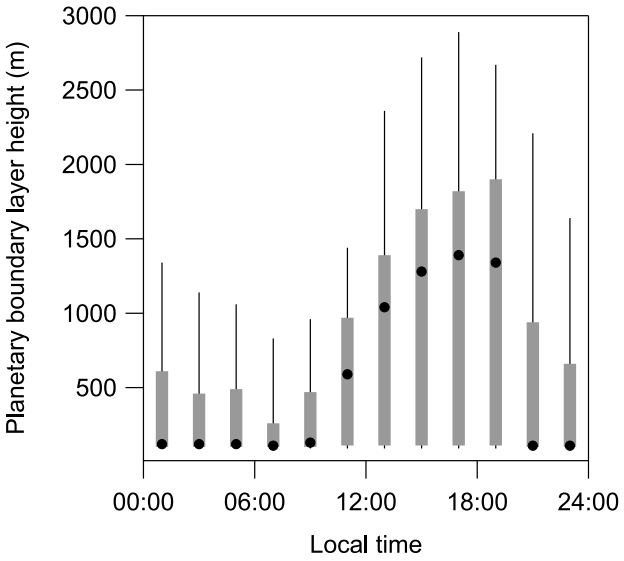


**Figure 2.8**: Diel profile of planetary boundary layer height binned bi-hourly [ARM Climate Research Facility, Ceilometer]. Symbols are medians, boxes are 25$^{th}$ and 75$^{th}$ percentiles, and whiskers are 5$^{th}$ and 95$^{th}$ percentiles.

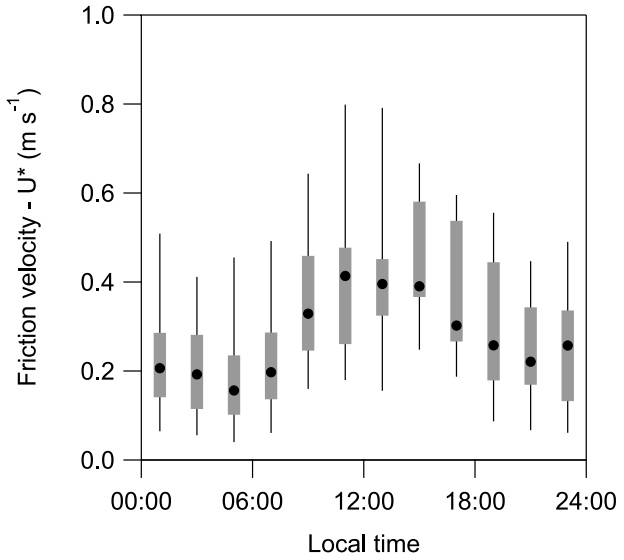


**Figure 2.9**: Diel profile of friction velocity (U*) binned bi-hourly for all possible flux periods. Symbols are medians, boxes are 25$^{th}$ and 75$^{th}$ percentiles, and whiskers are 5$^{th}$ and 95$^{th}$ percentiles.

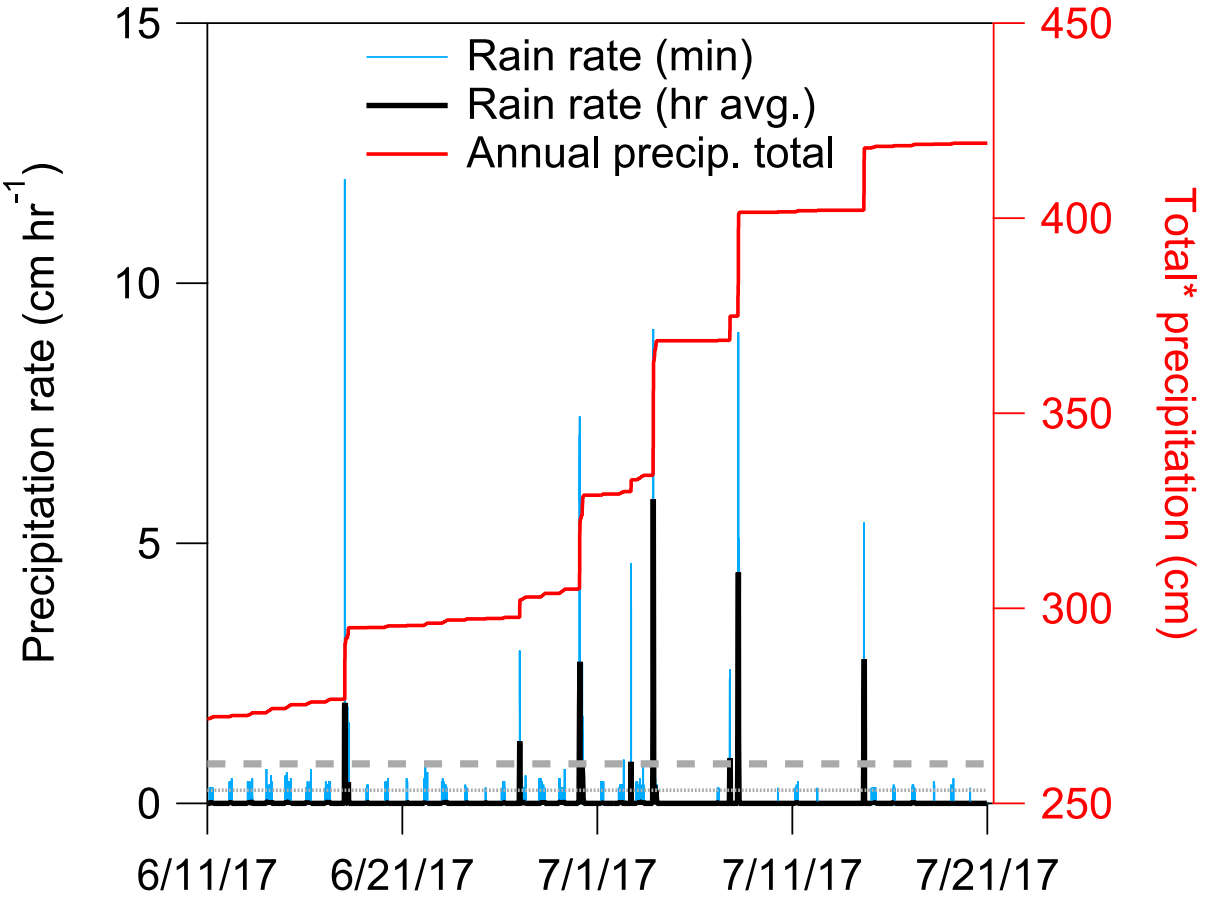


**Figure 2.10**: Precipitation data collected at the SGP field site [ARM Climate Research Facility, Weighing Bucket Precipitation Gauge]. Rain rate data are minute resolution (light blue line) and thus there are very brief instances of very intense rain. Also shown are hourly average rain rates (black line) and demarcations of heavy, moderate, and light rain [heavy rain (above thick dashed line; rate>0.76 cm $hr^{-1}$), moderate rain (between thin and thick dashed lines; 0.26 cm $hr^{-1}$<rate<0.76 cm $hr^{-1}$), and light rain (below thin dashed line; rate<0.26 cm $hr^{-1}$)]. (*) Total precipitation is defined as the start of the year and thus the amount of precipitation at the beginning of the campaign is above zero.

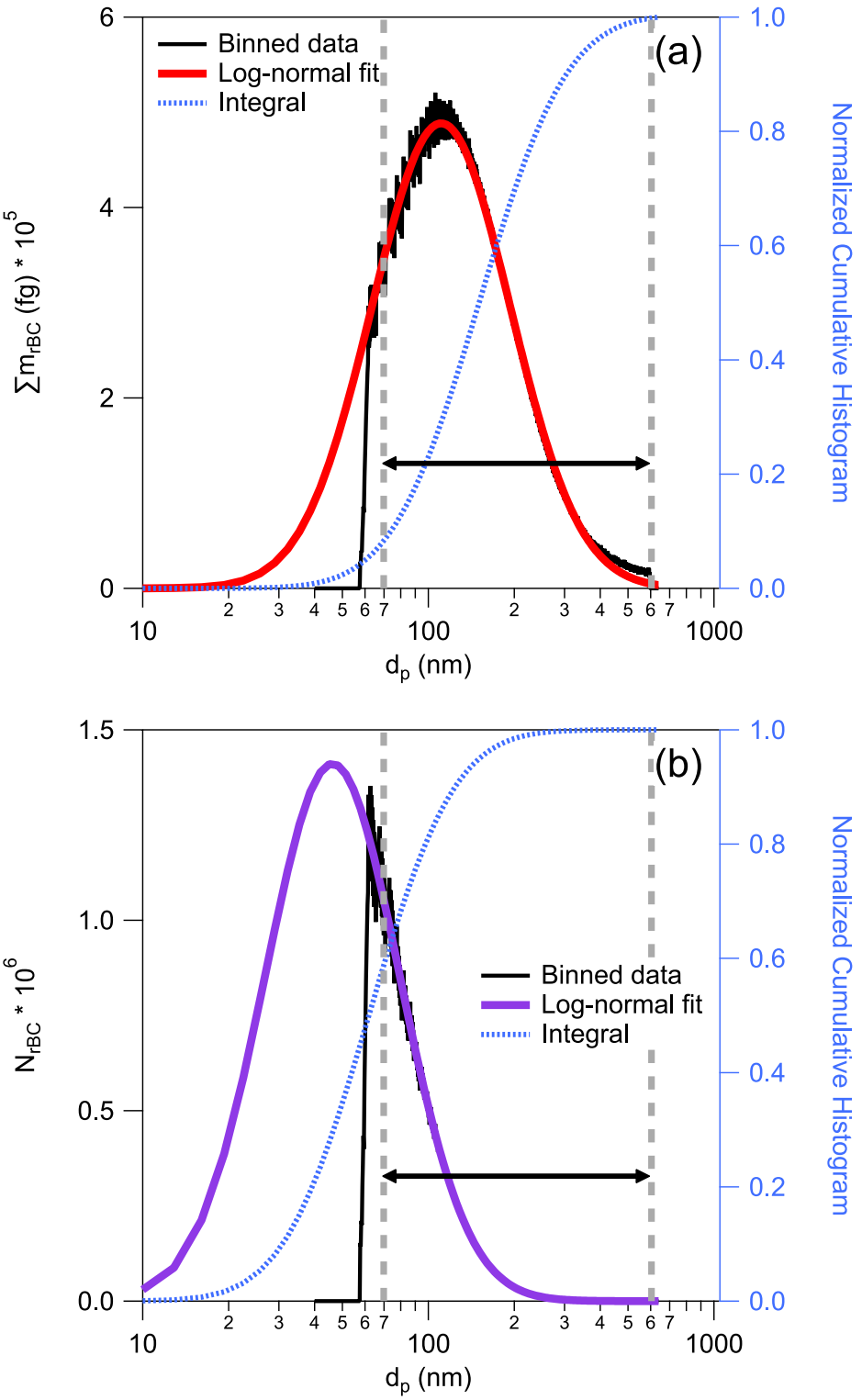


**Figure 2.11**: Histograms of the $\Sigma m_{rBC}$ (a) and $N_{rBC}$ (b) per $d_p$ bin (nm; volume equivalent diameter) for the entire campaign.

# CHAPTER 2 REFERENCES


Atmospheric Radiation Measurement (ARM) Climate Research Facility. 2011, updated hourly. Ceilometer (CEILPBLHT). 2017-06-01 to 2017-07-30, Southern Great Plains (SGP) Central Facility, Lamont, OK (C1). Compiled by B. Ermold and V. Morris. Atmospheric Radiation Measurement (ARM) Climate Research Facility Data Archive: Oak Ridge, Tennessee, USA. Data set accessed 2017-09-20 at http://dx.doi.org/10.5439/1095593

Atmospheric Radiation Measurement (ARM) Climate Research Facility. 2016, updated hourly. Weighing Bucket Precipitation Gauge (WBPLUVIO2). 2017-06-01 to 2017-07-31, Southern Great Plains (SGP) Central Facility, Lamont, OK (C1). Compiled by E. Cromwell, J. Delamere and M. Bartholomew. Atmospheric Radiation Measurement (ARM) Climate Research Facility Data Archive: Oak Ridge, Tennessee, USA. Data set accessed 2017-12-08.

Baldocchi, D. D., B. B. Hincks, and T. P. Meyers (1988), Measuring Biosphere-Atmosphere Exchanges of Biologically Related Gases with Micrometeorological Methods, *Ecology*, *69*(5), 1331–1340, doi:10.2307/1941631.

Billesbach, D. P. (2011), Estimating uncertainties in individual eddy covariance flux measurements: A comparison of methods and a proposed new method, *Agric. For. Meteorol.*, *151*(3), 394–405, doi:10.1016/j.agrformet.2010.12.001.

Bond, T. C., D. G. Streets, K. F. Yarber, S. M. Nelson, J. H. Woo, and Z. Klimont (2004), A technology-based global inventory of black and organic carbon emissions from combustion, *J. Geophys. Res. D Atmos.*, *109*(14), 1–43, doi:10.1029/2003JD003697.

Bond, T. C. et al. (2013), Bounding the role of black carbon in the climate system: A scientific assessment, *J. Geophys. Res. Atmos.*, *118*(11), 5380–5552, doi:10.1002/jgrd.50171.

Burba, G., and A. D.J. (2010), *A Brief Practical Guide to Eddy Covariance Flux Measurements: Principles and Workflow Examples for Scientific and Industrial Applications*.

Cross, E. S. et al. (2010), Soot particle studies-instrument inter-comparison-project overview, *Aerosol Sci. Technol.*, *44*(8), 592–611, doi:10.1080/02786826.2010.482113.

Dasch, J. M., and S. H. Cadle (1989), Atmospheric Carbon Particles in the Detroit Urban Area: Wintertime Sources and Sinks, *Aerosol Sci. Technol.*, *10*(2), 236–248, doi:10.1080/02786828908600508.

Fairall, C. . (1984), Interpretation of eddy-correlation measurements of particulate deposition and aerosol flux, *Atmos. Environ.*, *18*(7), 1329–1337, doi:10.1016/0004-6981(84)90041-6.

Farmer, D. K., P. J. Wooldridge, and R. C. Cohen (2006), Application of thermal-dissociation laser induced fluorescence (TD-LIF) to measurement of HNO3, Σalkyl nitrates, Σperoxy nitrates, and NO2 fluxes using eddy covariance, *Atmos. Chem. Phys.*, *6*(11), 3471–3486, doi:10.5194/acp-6-3471-2006.

Farmer, D. K., J. R. Kimmel, G. Phillips, K. S. Docherty, D. R. Worsnop, D. Sueper, E. Nemitz, and J. L. Jimenez (2011), Eddy covariance measurements with high-resolution time-of-flight aerosol mass spectrometry: a new approach to chemically resolved aerosol fluxes, *Atmos. Meas. Tech.*, *4*(6), 1275–1289, doi:10.5194/amt-4-1275-2011.

Finkelstein, P. L., and P. F. Sims (2001), Sampling error in eddy correlation flux measurements, *J. Geophys. Res. Atmos.*, *106*(D4), 3503–3509, doi:10.1029/2000JD900731.

Fischer, M. L., D. P. Billesbach, J. A. Berry, W. J. Riley, and M. S. Torn (2007), Spatiotemporal

variations in growing season exchanges of CO2, H2O, and sensible heat in agricultural fields of the Southern Great Plains, *Earth Interact.*, *11*(17), doi:10.1175/EI231.1.
Flanner, M. G., C. S. Zender, J. T. Randerson, and P. J. Rasch (2007), Present-day climate forcing and response from black carbon in snow, *J. Geophys. Res. Atmos.*, *112*(11), 1–17, doi:10.1029/2006JD008003.
Foken, T., and B. Wichura (1996), Tools for quality assessment of surface-based flux measurements, *Agric. For. Meteorol.*, *78*(1–2), 83–105, doi:10.1016/0168-1923(95)02248-1.
Gysel, M., M. Laborde, J. S. Olfert, R. Subramanian, and A. J. Gréhn (2011), Effective density of Aquadag and fullerene soot black carbon reference materials used for SP2 calibration, *Atmos. Meas. Tech.*, *4*(12), 2851–2858, doi:10.5194/amt-4-2851-2011.
Hansen, J., and L. Nazarenko (2004), Soot climate forcing via snow and ice albedos, *Proc. Natl. Acad. Sci.*, *101*(2), 423–428, doi:10.1073/pnas.2237157100.
Huang, L., S. L. Gong, C. Q. Jia, and D. Lavoué (2010), Importance of deposition processes in simulating the seasonality of the Arctic black carbon aerosol, *J. Geophys. Res. Atmos.*, *115*(17), 1–15, doi:10.1029/2009JD013478.
Jimenez, J. L. (2003), Ambient aerosol sampling using the Aerodyne Aerosol Mass Spectrometer, *J. Geophys. Res.*, *108*(D7), 8425, doi:10.1029/2001JD001213.
Kaimal, J. C., and J. J. Finnigan (1994), *Atmospheric boundary layer flows: their structure and measurement*, Oxford university press.
Kaspari, S., S. McKenzie Skiles, I. Delaney, D. Dixon, and T. H. Painter (2015), Accelerated glacier melt on Snow Dome, Mount Olympus, Washington, USA, due to deposition of black carbon and mineral dust from wildfire, *J. Geophys. Res. Atmos.*, *120*(7), 2793–2807, doi:10.1002/2014JD022676.
Koch, D., and A. D. Del Genio (2010), Black carbon semi-direct effects on cloud cover: Review and synthesis, *Atmos. Chem. Phys.*, *10*(16), 7685–7696, doi:10.5194/acp-10-7685-2010.
Koch, D. et al. (2009), Evaluation of black carbon estimations in global aerosol models, *Atmos. Chem. Phys.*, *9*(22), 9001–9026, doi:10.5194/acp-9-9001-2009.
Kondo, Y., K. Ram, N. Takegawa, L. Sahu, Y. Morino, X. Liu, and T. Ohara (2012), Reduction of black carbon aerosols in Tokyo: Comparison of real-time observations with emission estimates, *Atmos. Environ.*, *54*, 242–249, doi:10.1016/j.atmosenv.2012.02.003.
Kristensen, L., J. Mann, S. P. Oncley, and J. C. Wyngaard (1997), How Close is Close Enough When Measuring Scalar Fluxes with Displaced Sensors?, *J. Atmos. Ocean. Technol.*, *14*(4), 814–821, doi:10.1175/1520-0426(1997)014<0814:HCICEW>2.0.CO;2.
Laborde, M., P. Mertes, P. Zieger, J. Dommen, U. Baltensperger, and M. Gysel (2012), Sensitivity of the Single Particle Soot Photometer to different black carbon types, *Atmos. Meas. Tech.*, *5*(5), 1031–1043, doi:10.5194/amt-5-1031-2012.
Langford, B., W. Acton, C. Ammann, A. Valach, and E. Nemitz (2015), Eddy-covariance data with low signal-to-noise ratio: time-lag determination, uncertainties and limit of detection, *Atmos. Meas. Tech.*, *8*(10), 4197–4213, doi:10.5194/amt-8-4197-2015.
Lee, L. A., K. J. Pringle, C. L. Reddington, G. W. Mann, P. Stier, D. V. Spracklen, J. R. Pierce, and K. S. Carslaw (2013), The magnitude and causes of uncertainty in global model simulations of cloud condensation nuclei, *Atmos. Chem. Phys.*, *13*(17), 8879–8914, doi:10.5194/acp-13-8879-2013.
Lee, X., W. Massman, and B. Law (2005), *Handbook of Micrometeorology*, Atmospheric and Oceanographic Sciences Library, edited by X. Lee, W. Massman, and B. Law, Springer

Netherlands, Dordrecht.
Lenschow, D. H., and L. Kristensen (1985), Uncorrelated Noise in Turbulence Measurements, *J. Atmos. Ocean. Technol.*, *2*(1), 68–81, doi:10.1175/1520-0426(1985)002<0068:UNITM>2.0.CO;2.
Liu, J., S. Fan, L. W. Horowitz, and H. Levy (2011), Evaluation of factors controlling long-range transport of black carbon to the Arctic, *J. Geophys. Res.*, *116*(D4), D04307, doi:10.1029/2010JD015145.
Mahrt, L. (1998), Flux Sampling Errors for Aircraft and Towers, *J. Atmos. Ocean. Technol.*, *15*(2), 416–429, doi:10.1175/1520-0426(1998)015<0416:FSEFAA>2.0.CO;2.
Massman, W. J. (2000), A simple method for estimating frequency response corrections for eddy covariance systems, *Agric. For. Meteorol.*, *104*(3), 185–198, doi:10.1016/S0168-1923(00)00164-7.
Menon, S., D. Koch, G. Beig, S. Sahu, J. Fasullo, and D. Orlikowski (2010), Black carbon aerosols and the third polar ice cap, *Atmos. Chem. Phys.*, *10*(10), 4559–4571, doi:10.5194/acp-10-4559-2010.
Moncrieff, J., R. Clement, J. Finnigan, and T. Meyers (2004), Averaging, Detrending, and Filtering of Eddy Covariance Time Series, in *Handbook of Micrometeorology*, pp. 7–31, Kluwer Academic Publishers, Dordrecht.
Moore, C. J. (1986), Frequency response corrections for eddy correlation systems, *Boundary-Layer Meteorol.*, *37*(1–2), 17–35, doi:10.1007/BF00122754.
Mori, T., Y. Kondo, S. Ohata, N. Moteki, H. Matsui, N. Oshima, and A. Iwasaki (2014), Wet deposition of black carbon at a remote site in the East China Sea, *J. Geophys. Res. Atmos.*, *119*(17), 10485–10498, doi:10.1002/2014JD022103.
Moteki, N., and Y. Kondo (2010), Dependence of Laser-Induced Incandescence on Physical Properties of Black Carbon Aerosols: Measurements and Theoretical Interpretation, *Aerosol Sci. Technol.*, *44*(8), 663–675, doi:10.1080/02786826.2010.484450.
Nemitz, E., J. L. Jimenez, J. A. Huffman, I. M. Ulbrich, M. R. Canagaratna, D. R. Worsnop, and A. B. Guenther (2008), An Eddy-Covariance System for the Measurement of Surface / Atmosphere Exchange Fluxes of Submicron Aerosol Chemical Species — First Application Above an Urban Area, *Aerosol Sci. Technol.*, *42*(8), 636–657, doi:10.1080/02786820802227352.
Nilsson, E. D., Ü. Rannik, M. Kumala, G. Buzorius, C. D. O, Ü. Rannik, M. Kumala, G. Buzorius, and C. D. O (2016), Tellus B : Chemical and Physical Meteorology Effects of continental boundary layer evolution , convection , turbulence and entrainment , on aerosol formation E ff ects of continental boundary layer evolution , convection , turbulence and entrainment , on , , *889*(July 2017), 441–461, doi:10.3402/tellusb.v53i4.16617.
Ogren, J. A., P. J. Groblicki, and R. J. Charlson (1984), Measurement of the removal rate of elemental carbon from the atmosphere, *Sci. Total Environ.*, *36*, 329–338, doi:10.1016/0048-9697(84)90284-5.
Ohata, S., N. Moteki, and Y. Kondo (2011), Evaluation of a Method for Measurement of the Concentration and Size Distribution of Black Carbon Particles Suspended in Rainwater, *Aerosol Sci. Technol.*, *45*(11), 1326–1336, doi:10.1080/02786826.2011.593590.
Ohata, S., N. Moteki, J. P. Schwarz, D. W. Fahey, and Y. Kondo (2013), Evaluation of a Method to Measure Black Carbon Particles Suspended in Rainwater and Snow Samples, *Aerosol Sci. Technol.*, *47*(10), 1073–1082, doi:10.1080/02786826.2013.824067.

Papale, D. et al. (2006), Towards a standardized processing of Net Ecosystem Exchange\rmeasured with eddy covariance technique: algorithms and\runcertainty estimation, *Biogeosciences*, *3*, 571–583.

Petzold, A. et al. (2013), Recommendations for reporting black carbon measurements, *Atmos. Chem. Phys.*, *13*(16), 8365–8379, doi:10.5194/acp-13-8365-2013.

Pryor, S. C. et al. (2008a), A review of measurement and modelling results of particle atmosphere–surface exchange, *Tellus B Chem. Phys. Meteorol.*, *60*(1), 42–75, doi:10.1111/j.1600-0889.2007.00298.x.

Pryor, S. C., S. E. Larsen, L. L. Sørensen, and R. J. Barthelmie (2008b), Particle fluxes above forests: Observations, methodological considerations and method comparisons, *Environ. Pollut.*, *152*(3), 667–678, doi:10.1016/j.envpol.2007.06.068.

Pryor, S. C., R. J. Barthelmie, L. L. SØrensen, S. E. Larsen, A. M. Sempreviva, T. Grönholm, Ü. Rannik, M. Kulmala, and T. Vesala (2008c), Upward fluxes of particles over forests: when, where, why?, *Tellus B Chem. Phys. Meteorol.*, *60*(3), 372–380, doi:10.1111/j.1600-0889.2008.00341.x.

Reddy, M. S., and O. Boucher (2004), A study of the global cycle of carbonaceous aerosols in the LMDZT general circulation model, *J. Geophys. Res.*, *109*(D14), D14202, doi:10.1029/2003JD004048.

Riley, W. J., S. C. Biraud, M. S. Torn, M. L. Fischer, D. P. Billesbach, and J. A. Berry (2009), Regional CO2 and latent heat surface fluxes in the Southern Great Plains: Measurements, modeling, and scaling, *J. Geophys. Res. Biogeosciences*, *114*(4), 1–15, doi:10.1029/2009JG001003.

Rowe, M. D., C. W. Fairall, and J. A. Perlinger (2011), Chemical sensor resolution requirements for near-surface measurements of turbulent fluxes, *Atmos. Chem. Phys.*, *11*(11), 5263–5275, doi:10.5194/acp-11-5263-2011.

Ruijrok, W., C. I. Davidson, and K. W. Nicholson (1995), Dry deposition of particles., *Tellus B*, *47*(5), 587–601, doi:10.1034/j.1600-0889.47.issue5.6.x.

Schwarz, J. P. et al. (2006), Single-particle measurements of midlatitude black carbon and light-scattering aerosols from the boundary layer to the lower stratosphere, *J. Geophys. Res. Atmos.*, *111*(16), 1–15, doi:10.1029/2006JD007076.

Schwarz, J. P., S. J. Doherty, F. Li, S. T. Ruggiero, C. E. Tanner, A. E. Perring, R. S. Gao, and D. W. Fahey (2012), Assessing Single Particle Soot Photometer and Integrating Sphere/Integrating Sandwich Spectrophotometer measurement techniques for quantifying black carbon concentration in snow, *Atmos. Meas. Tech.*, *5*(11), 2581–2592, doi:10.5194/amt-5-2581-2012.

Sisterson, D. L., R. A. Peppler, T. S. Cress, P. J. Lamb, and D. D. Turner (2016), The ARM Southern Great Plains (SGP) Site, *Meteorol. Monogr.*, *57*, 6.1-6.14, doi:10.1175/AMSMONOGRAPHS-D-16-0004.1.

Spackman, J. R., R. S. Gao, W. D. Neff, J. P. Schwarz, L. A. Watts, D. W. Fahey, J. S. Holloway, T. B. Ryerson, J. Peischl, and C. A. Brock (2010), Aircraft observations of enhancement and depletion of black carbon mass in the springtime Arctic, *Atmos. Chem. Phys.*, *10*(19), 9667–9680, doi:10.5194/acp-10-9667-2010.

Spirig, C., A. Neftel, C. Ammann, J. Dommen, W. Grabmer, A. Thielmann, A. Schaub, J. Beauchamp, A. Wisthaler, and A. Hansel (2005), Eddy covariance flux measurements of biogenic VOCs during ECHO 2003 using proton transfer reaction mass spectrometry, *Atmos. Chem. Phys.*, *5*(2), 465–481, doi:10.5194/acp-5-465-2005.

Stephens, M., N. Turner, and J. Sandberg (2003), Particle identification by laser-induced incandescence in a solid-state laser cavity, *Appl. Opt.*, *42*(19), 3726, doi:10.1364/AO.42.003726.

Taipale, R., T. M. Ruuskanen, and J. Rinne (2010), Lag time determination in DEC measurements with PTR-MS, *Atmos. Meas. Tech.*, *3*(4), 853–862, doi:10.5194/amt-3-853-2010.

Wesely, M. (1989), Parameterization of surface resistances to gaseous dry deposition in regional-scale numerical models, *Atmos. Environ.*, *23*(6), 1293–1304, doi:10.1016/0004-6981(89)90153-4.

Wienhold, F. (1995), Micrometeorological measurement and source region analysis of nitrous oxide fluxes from an agricultural soil, *Atmos. Environ.*, *29*(17), 2219–2227, doi:10.1016/1352-2310(95)00165-U.

Wilczak, J. M., S. P. Oncley, and S. A. Stage (2001), Sonic Anemometer Tilt Correction Algorithms, *Boundary-Layer Meteorol.*, *99*(1), 127–150, doi:10.1023/A:1018966204465.

Wyngaard, J. C. (1973), *On surface-layer turbulence, in Workshop on Micrometeorology*, edited by D. A. Haugen, American Meteorlogical Society, Boston.

Yasunari, T. J., Q. Tan, K. M. Lau, P. Bonasoni, A. Marinoni, P. Laj, M. Ménégoz, T. Takemura, and M. Chin (2013), Estimated range of black carbon dry deposition and the related snow albedo reduction over Himalayan glaciers during dry pre-monsoon periods, *Atmos. Environ.*, *78*, 259–267, doi:10.1016/j.atmosenv.2012.03.031.

Zhang, L., S. Gong, J. Padro, and L. Barrie (2001), A size-segregated particle dry deposition scheme for an atmospheric aerosol module, *Atmos. Environ.*, *35*(3), 549–560, doi:10.1016/S1352-2310(00)00326-5.

# CHAPTER 3 – OBSERVATIONALLY DRIVEN SIZE RESOLVED DRY DEPOSITION PARAMETERIZATION IMPACTS RADIATIVE FORCING IN CHEMICAL TRANSPORT MODELS[3]

## Overview

Removal of aerosols from the atmosphere occurs via wet and dry deposition. Dry deposition is suggested as a significant source of uncertainty in global chemical transport and climate models. Most global models follow parameterizations that were developed when direct measurements of particle deposition were sparse. Since then, new measurement techniques have enabled many more size-resolved particle flux measurements. Integrating those measurements, including data we collected over a grassland in Oklahoma and a ponderosa pine forest in Colorado, we show that model parameterizations of particle deposition velocities across many particle size ranges, including the accumulation mode, may be off by as much as an order of magnitude over terrestrial ecosystems. As accumulation mode particles drive the cloud condensation nuclei that influence the indirect radiative effect, this persistent inaccuracy wreaks havoc with estimated particle concentrations, size distributions, and thus predictions of radiative forcing. Relative to observations, previous parameterizations overestimated deposition in the accumulation and fine mode particles, and underestimated in the coarse modes. We present a revised and observationally driven parameterization that is easily implemented into a chemical transport model, GEOS-Chem. Using this revision in GEOS-Chem we find that cloud condensation nuclei increase by 12% and leads to -0.63 W $m^{-2}$ change in the aerosol indirect effect globally. The observationally-constrained

[3] This chapter is with coauthors for review. All analysis of this publicly available data was carried out by Ethan W. Emerson. Measurements collected during BCADS were obtained by Ethan W. Emerson and measurements collected during SPiFFY was done by Holly DeBolt. Modelling was performed by Anna L. Hodshire.

approach reduces the uncertainty of dry deposition in global chemical transport models and improve the accuracy of model outputs.

**Introduction**

The aerosol direct and indirect effect are the largest sources of uncertainty associated with anthropogenic forcing (Houghton and Intergovernmental Panel on Climate Change. Working Group I., 2001;Solomon et al., 2007;Stocker, 2014;Lee et al., 2013). Aerosols affect climate through two distinct processes: the direct effect, through which aerosols either scatter or absorb radiation thereby warming or cooling the climate directly, and the indirect effect, through which aerosols interact with clouds which alter droplet concentration, cloud albedo, and precipitation. (Lohmann and Feichter, 2005) The effect of anthropogenic aerosols on cloud droplet concentrations and thus radiative properties is one of the largest sources of uncertainty on radiative forcing during the industrial period. (Carslaw et al., 2013) These cloud drop concentrations, along with albedo and precipitation, are driven by cloud condensation nuclei (CCN) the small particles that nucleate liquid water to become cloud droplets. (Farmer et al., 2015) Dry deposition in the accumulation mode is identified as the single most important process affecting global mean CCN uncertainty. (Lee et al., 2013) Thus improving our understanding of dry deposition of accumulation mode particles can directly reduce uncertainties in models of radiative forcing.

The removal of particles is determined by both wet and dry deposition. Wet deposition refers to the removal of particles by precipitation, while dry deposition refers to direct uptake by terrestrial surfaces. (Schwede and Lear, 2014) While wet deposition is typically thought to dominate aerosol lifetime, dry deposition remains a globally important first order loss process that scales with concentration and is critical for accurate spatial and temporal distributions. (Gong et al., 2015;Lee et al., 2017;Schwede and Lear, 2014) Dry deposition in most global models stems

from theoretical work conducted by Slinn. (Slinn, 1977;Slinn and Slinn, 1980;Slinn, 1982) The derivatives include the Wesely (1989), Zhang et al. (2001), Seinfeld and Pandis (2006) parameterizations that are often implemented in air quality models. (Solazzo et al., 2012) All of these parameterizations follow a resistance model and generally predict a deposition velocity minimum in the super-micron coarse mode. At the time of Slinn's pioneering work, there were few particle flux measurements over the terrestrial biosphere, but direct measurements of particle deposition have progressed substantially over the past decade.

Direct measurements, including our work over grasslands and pine forests described below, have provided mounting evidence for a minimum deposition velocity that occurs within the accumulation mode. (Hicks et al., 2016;Saylor et al., 2019;Petroff et al., 2008;Petroff and Zhang, 2010;Zhang and Vet, 2006;Pryor et al., 2008) Parameterizations considering this observational evidence have been developed in recent years (e.g. Petroff et al. (2008), Kouznetsov and Sofiev (2012), Zhang and He (2014), Zhang and Shao (2014), Saylor et al. (2019)), but are sophisticated and computationally intense. To our knowledge only the Petroff and Zhang (2010) algorithm has been implemented into a global model, specifically to examine the spatial distributions and radiative effects from black carbon. (Wu et al., 2018)

Size resolved dry deposition measurements are not accurately described by the Zhang et al. (2001) parameterization. Figure 3.2 identifies the key components used in a typical dry deposition scheme for surface resistance: gravitational settling, Brownian diffusion, interception, and impaction processes. (Zhang et al., 2001) Using this framework and modifications suggested by Petroff and Zhang (2010) we modify six land use independent empirical coefficients to describe observed deposition velocities presented herein as well as observations presented throughout the literature. This revised parameterization leverages a substantial number of measurements that were

not available to either Zhang et al. (2001) or Slinn, 1982. These modifications are easily accomodated by a global chemical transport model (GEOS-Chem with the TOMAS aerosol microphysics module). Using the revised scheme we examine the impact of an observationally driven dry deposition routine that accurately describes measurements and reduces aerosol dry deposition uncertainty. These changes affects aerosol concentrations, radiative forcing, emission inventories, cloud condensation nuclei, and PM2.5, inaccurate representation of observed dry deposition velocities of this magnitude affects almost all processes aerosols interact with.

*Dry Deposition Models: Approach and Historical Context*

Slinn (1982) describes dry deposition velocities ($V_d$) as a size-dependent resistance model with several components: gravitational settling of particles, interception, impaction and Brownian diffusion. Gravitational settling is treated with a single parameter describing settling velocity, Vg. The resistance to particles moving through the atmosphere to reach the forest canopy surface is described as the aerodynamic resistance $R_a$, while interception impaction and Brownian diffusion control whether a particle actually deposits to a leaf or other surface, and is described by the surface resistance $R_s$.

$$V_d = V_g + \frac{1}{R_a + R_s} \tag{3.1}$$

where $V_g$ is the gravitational setting velocity. $R_a$ and $R_s$ are the aerodynamic resistances above the canopy and the surface resistance respectively. The gravitational setting velocity is computed as

$$V_g = \frac{\rho d_p^2 g C}{18\eta} \tag{3.2}$$

where $\rho$ is the density of the particle, $d_p$ is the diameter of the particle, $g$ is gravitational acceleration, $C$ is the Cunningham slip correction factor for small particles, and $\eta$ is the viscosity coefficient of air. While the Cunningham slip correction is typically described as

$$C = 1 + \frac{2\lambda}{d_p}(1.257 + 0.4e^{-0.55d_p/\lambda}) \tag{3.3}$$

where $\lambda$ is the mean free path of air molecules, this equation is slightly modified in GEOS-Chem to:

$$C = 1 + \frac{1}{d_p}(15.60 + 7.00e^{-0.59d_p}) \tag{3.4}$$

While GEOS-Chem separates the aerodynamic resistance and surface resistance into different component, it is computed as

$$R_a = \frac{ln\left(\frac{z_R}{z_0}\right) - \psi_H}{\kappa u_*} \tag{3.5}$$

where $z_R$ is the reference height where $V_d$ is calculated, $z_0$ is the roughness height, $\kappa$ is the von Karman constant, and $u_*$ is the friction velocity, and $\psi_H$ is the stability function for heat:

$$\psi_H = 2ln\left[\frac{1}{2}\left(1 + \sqrt{1 - 16\frac{z}{L_0}}\right)\right] \text{ when } \frac{z}{L_0} \in [-2; 0] \tag{3.6a}$$

$$\psi_H = -5\frac{z}{L_0} \text{ when } \frac{z}{L_0} \in [0; 1] \tag{3.6b}$$

The surface resistance ($R_s$) is a function of the particle collection efficiencies due to three loss processes: Brownian diffusion ($E_b$), impaction ($E_{Im}$), and interception ($E_{In}$). $R_s$ is parameterized as

$$R_s = \frac{1}{\varepsilon_0 u_* (E_b + E_{Im} + E_{In})\, R_1} \tag{3.7}$$

where $\varepsilon_0$ is an empirical coefficient and is set to 3 for all land use covers (LUCs), and $R_1$ is a correction factor for particle rebound modifying collection efficiencies at the surface. $R_1$ is computed as a function of the Stokes number (*St*) as

$$R_1 = e^{-1/\sqrt{St}} \tag{3.8}$$

The collection efficiency of Brownian diffusion is described as a function of the Schmidt number (Sc)

$$E_B = Sc^{-\gamma} \tag{3.9}$$

where Sc is the ratio of kinematic viscosity of air ν to particle Brownian diffusivity (D), and γ is a LUC-dependent variable that varies between 1/2 and 2/3 with larger values for rougher surfaces. Brownian diffusivity is calculated by

$$D = \frac{Ck_BT}{3\pi\mu d_p} \tag{3.10}$$

where $k_B$ is Boltzmann's constant, T is temperature (K), and μ is the dynamic viscosity of air at temperature T.

The parameter governing impaction is the Stokes number (St) which has two forms, one for smooth surfaces (*3*.11a) and one for vegetated surfaces (*3*.11b). (Slinn, 1982)

$$St = \frac{V_g {u_*}^2}{\nu} \tag{3.11a}$$

$$St = \frac{V_g u_*}{gA} \tag{3.11b}$$

Slinn (1982) suggested two parameterizations for smooth (*3*.12a) and vegetated (*3*.12b) surfaces to described the collection efficiency by impaction

$$E_{Im} = 10^{-\frac{3}{St}} \tag{3.12a}$$

$$E_{Im} = \frac{St^2}{1+St^2} \tag{3.12b}$$

This was subsequently refined by Peters and Eiden (1992) to the following form derived from a spruce forest

$$E_{Im} = \left(\frac{St}{\alpha+St}\right)^{\beta} \tag{3.13}$$

Where α and β are constants (0.8 and 2 respectively) from best fit for data collected by Belot and Gauthier (1974). This particular form is used by Zhang et al. (2001) where α varies with LUC and β is 2 and this is the collection efficiency implemented in GEOS-Chem.

The collection efficiency by interception refers to the process by which a particles passes a surface at a distance less than its physical dimensions. A simple form is used to calculate collection efficiency by interception

$$E_{In} = \frac{1}{2}\left(\frac{d_p}{A}\right)^2 \tag{3.14}$$

where *A* is the characteristic radius for different LUCs and seasonal categories (SSC). (Slinn, 1982).

The algorithm for surface resistance currently implemented in GEOS-Chem (and many other global models) is from Zhang et al. (2001). This algorithm is fundamentally based on Equation *3.*7, and uses Equations *3.*9, *3.*13, and *3.*14 to describe the collection efficiencies from Brownian diffusion, impaction, and interception. GEOS-Chem uses Equations *3.*11a and *3.*11b to compute the Stokes number (relevant to impaction, Equation *3.*13), and Equation *3.*8 to correct for particle rebound. This algorithm affords a simple and computationally efficient method of determining the surface resistance and thus dry deposition velocities. Given the observational

evidence that models and measurements disagree, we rewrite Equations 9, 13, and 14 to a more general form that is based on Zhang et al. (2001).

$$E_B = C_b Sc^{-2/3} \tag{3.15}$$

$$E_{Im} = C_{Im}\left(\frac{St}{\alpha+St}\right)^{\beta} \tag{3.16}$$

$$E_{In} = C_{In}\left(\frac{d_p}{A}\right)^{\upsilon} \tag{3.17}$$

These equations represent a physical basis for deposition with empirical coefficients that can be easily modified to represent observations.

**Methods**

*Site & Instrumentation*

Two distinct field campaigns are used in this study: (1) data collected during the five distinct measurement periods of the Seasonal Particles in Forest Flux studY (SPiFFY) at the Manitou Experimental Forest and (2) data collected during the BCADS 2017 campaign. (Emerson et al., 2018) The Manitou Experimental Forest and SGP are well-known sites, and have been described elsewhere (Fischer et al., 2007;Riley et al., 2009;Sisterson et al., 2016;Fulgham et al., 2019;Ortega et al., 2014).

Instruments were housed in a temperature controlled enclosure at the base of the tower during both field campaigns. During SPiFFY, the inlet was located at 26 m above ground level with an inlet length of ~30 m (3/8'' i.d. copper tubing) with a turbulent flow rate of 19 L $min^{-1}$ and a residence time of 3 s. During BCADs, the inlet was located 2.7 m above ground level with a length of ~4.5m of 4.3 mm internal diameter stainless steel tubing operated at 12 L $min^{-1}$ and a residence time of 0.3 s. In both field campaigns the inlet was aligned downward (45°±15º angle), with a wire mesh screen to exclude insect and debris contamination, and proximal to the sonic anemometer (slightly below in both cases, <50 cm distance).

Particles were measured by sampling off the bypass line at 0.6 $cm^3$ $s^{-1}$ using the Ultra-High Sensitivity Aerosol Spectrometer (UHSAS, Droplet Measurement Technologies, Inc., Longmont CO) operating with a 1054 nm wavelength laser counting particles with an optical diameter from 60 nm to 100 nm at 10 Hz. Particles were collected into 99 original size bins that were aggregated into 12 bins (diameter ranges in nm): 60-70, 70-84, 84-103, 103-126, 126-153, 153-177, 177-204, 204-286, 286-403, 403-506, 506-711, and 711-1000. The UHSAS operated on its own internal PC collecting data at 10Hz with continuous timestamps. The UHSAS was calibrated prior to each field campaign with polystyrene latex spheres.

Three dimensional, high frequency (10 Hz) windspeed data were collected using a Campbell CSAT III anemometer during summer 2015, winter 2016, spring 2016, and summer 2016 and an Applied Technologies Inc. A-probe sonic anemometer during fall 2016. These data were collected on a separate computer, and time stamps were synced using Meinberg.

*Eddy Covariance Flux Analysis*

We measure surface-atmosphere exchange with the eddy covariance flux technique. This technique measures the vertical flux ($F_c$) for a given scalar crossing the measurement plane of a horizontally homogenous area. $F_c$ is determined by the covariance of the vertical windspeed (w) and scalar (*c;* e.g. species mixing ratio or particle concentration)

$$F_c = \overline{\langle w'c' \rangle} = \frac{1}{n} \sum_{i=0}^{n} (c_i - \bar{c}) \ (w_i - \overline{w}) \tag{3.18}$$

where n is the number of points used in the calculation (18000 for these data), $w_i$ and $c_i$ are instantaneous measurements of vertical windspeed and scalar respectively, and $\overline{w}$ and $\overline{c}$ are the mean vertical windspeed and scalar measurement. (Baldocchi et al., 1988) Eddy covariance flux measurements can be calculated over varying timescales, but 30-minutes is typical and employed

here. The deposition velocity is determined from the flux and the mean concentration over the 30-minute flux period as:

$$F_c = -V_d \bar{c} \tag{3.19}$$

Where a positive $V_d$ indicates deposition and a negative $V_d$ implies an emission process.

We employed the following approach to calculate eddy covariance fluxes of size-resolve particle bins:

1) Calculation of particle diameter (determined by UHSAS)
2) Timelag correction: scalar data was corrected to adjust for the timelag between the sonic and UHSAS data. Sonic data was adjusted by -3 s and -0.3 s for the SPiFFY and BCADS campaigns according to bypass flow rates.
3) Sonic rotation: a two-dimensional rotation to windspeed in three axes to account for the sonic anemometer not being precisely level with the ground. (Massman, 2000;Wilczak et al., 2001)
4) Flux calculation: Equation *3*.18
5) Quality control: stationarity test and wind direction
    a. The stationarity test is applied to ensure that calculated fluxes do not vary substantially within the time-scale of analysis and is calculated by comparing 5-minute fluxes to the 30-minute flux. (Foken and Wichura, 1996)
    b. Flux periods with an average wind direction that is obstructed by the sampling tower were removed.
6) Corrections: many corrections (storage, time response, sensor separation, tube attenuation, Webb-Pearman-Leuning (WPL), de-spiking, and de-trending) were considered and only the storage correction is found to be significant and is thus included.

a. During horizontally homogenous conditions, the turbulent flux below the measurement height can be different. Due to a lack of below sensor measurements, we use a one-point storage term developed by Rannik et al. (2009)

$$F_{storage} = \int_0^{z_r} \frac{\partial \bar{c}}{\partial t} dz \approx z_r \frac{\overline{c(t+\Delta T)} - \overline{c(t)}}{\Delta T} \quad (3.20)$$

where $c$ is the concentration and $t$=2 min with $\Delta T$=30 min. These values were calculated for all flux periods that ended within 10 seconds of the next one starting.

7) Uncertainty: flux uncertainty is computed using Finkelstein and Sims (2001). All data discussed are presented as particle size bin averages. We present an average calculated limit of detection as the uncertainty associated with a single measurement can surpass the magnitude of the measurement.(Langford et al., 2015)

$$\overline{LOD} = \frac{1}{N} \sqrt{\sum_{i=1}^{N} (\alpha \times RE_i)_i^2} \quad (3.21)$$

where α is a specified confidence interval (α=3 for the 99$^{th}$ percentile) and $RE_i$ is the error of a particular flux period as calculated using Finkelstein and Sims (2001). We propagate the flux limit of detection calculated in Equation *3*.21 to a deposition velocity limit of detection using Equation *3*.19.

*Spectral Analysis*

Eddy covariance requires a sufficiently fast sensor response time. This has been previously shown for the UHSAS as well as other particle counting methods (Petroff et al., 2018;Deventer et al., 2015;Mammarella et al., 2011). We show an example cospectrum (Figure 3.1) for a day during the Summer 2015 SPIFFY campaign. The characteristic inertial subrange ($f^{-7/3}$) predicted by

Kolmogorov Theory (Kaimal and Finnigan, 1994) is observed between 0.1 and 3 Hz and demonstrates a sufficiently fast sensor response time for this instrument. Additionally, the particle data follows the sensible heat cospectrum and that is a near ideal measurement.

**Revised Particle Dry Deposition**

To address the differences between observations and model outputs we have revised coefficients (implicitly or explicitly) that exist in the commonly employed Zhang et al. (2001) in models such as GEOS-Chem. We used the BCADS and SPiFFY datasets to revise the algorithm, they afforded all relevant meteorological parameters at 30-minute intervals. However, while these datasets provide substantial depth between 60-1000 nm particle size ranges, they do not provide information on particle deposition outside of that range. To this end, we consider measurements collected by other groups across other particle size ranges and an array of land use types. The resulting parameterization follows the structure of Zhang 2001, but with key elements of Petroff and Zhang 2010. This 'Revised' parameterization provides an improved representation of both our and other data. Table 1 summarizes the resulting parameterizations, including changes to the interception and Brownian diffusion collection efficiencies.

Fundamentally, the current parameterization in GEOS-Chem suggests a minimum deposition velocity around 1 μm, whereas observations suggest that it is closer to 0.1 μm (Figure 3.4). Brownian diffusion, interception, and impaction collection efficiencies are the ensemble that dictates where the minimum occurs. In the Zhang 2001 parameterization, the Brownian and impaction collection efficiencies drive the location of the minimum deposition velocity. At the time of the Zhang et al. (2001) parameterization, this made sense as many of the flux measurements and deposition velocities were based on smooth and non-vegetated surfaces and thus minimized

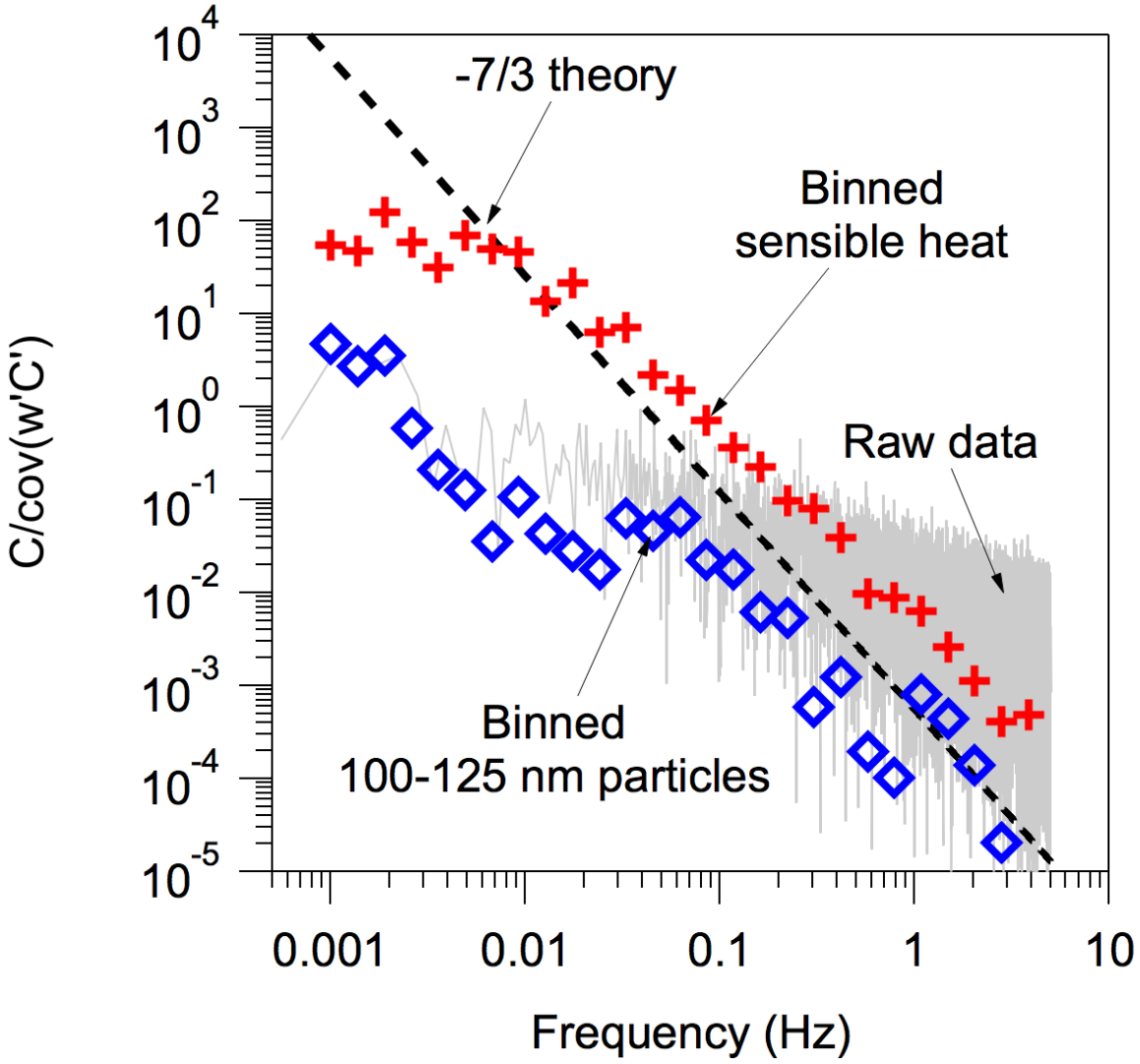


**Figure 3.1**: Example cospectrum for 100-125 nm particles and sensible heat from 13-July 2015 at 8 AM during the SPIFFY field campaign.

**Table 1**: Collection efficiency parameters that govern the surface resistance term from two previously published model algorithms and a revised scheme driven by observations.

| | Zhang 2001 | Petroff 2010 | Revised |
|---|---|---|---|
| **Brownian** | $C_B Sc^{-\gamma}$ | $C_B Sc^{-\gamma} * Re^{-1/2}$ | $C_B Sc^{-\gamma}$ |
| γ | 0.5-0.58 | 2/3 | 2/3 |
| $C_B$ | 1 | 0.7-1.262 | 0.2 |
| **Interception** | $C_{In}\left(\frac{d_p}{A}\right)^{\upsilon}$ | $C_{In}\left(\frac{d_p}{L}\right)^{\upsilon}$ **or** $C_{In}\left(\frac{d_p}{L}\right)\left[2+\ln\left(\frac{4L}{d_p}\right)\right]$ | $C_{In}\left(\frac{d_p}{A}\right)^{\upsilon}$ |
| υ | 2 | 1 | 0.8 |
| $C_{In}$ | 0.5 | 0.14-0.81 | 2.5 |
| **Impaction** | $C_{Im}\left(\frac{St}{0.8+St}\right)^{2}$ | $C_{Im}\left(\frac{St}{\alpha+St}\right)^{2}$ | $C_{Im}\left(\frac{St}{\alpha+St}\right)^{1.7}$ |
| β | 2 | 2 | 1.7 |
| $C_{Im}$ | 1 | 0.47-0.6 | 0.4 |
| **Notes** | | For vegetated surfaces, smooth surfaces are parameterized in a different way. 26 land use surfaces are parameterized in this model | |
| **Notes** | | Our measurements indicate the term $Re^{-1/2}$ is typically around 0.02±0.01 with a max of 0.18, | |
| **Notes** | | L is the same parameter as A in Zhang and the revised parameterization. Slightly different values are used | |

the need for a substantial interception component. Considering the wealth of measurements over evergreen needle leaf forests, it is evident that this particular parameter needed reconsidering. Changing the empirical coefficients affecting this parameter shifted the minimum deposition and deposition velocities were based on smooth and non-vegetated surfaces and thus minimized the need for a substantial interception component. Considering the wealth of measurements over evergreen needle leaf forests, it is evident that this particular parameter needed reconsidering. Changing the empirical coefficients affecting this parameter shifted the minimum deposition velocity towards smaller particles and in concert with relatively small changes to the Brownian diffusion coefficients the minimum could be efficiently centered around the observed minimum deposition velocity for needle leaf forests. The reconsideration of the Brownian diffusion and interception collection efficiencies was originally presented in a detailed microphysical model by Petroff and Zhang (2010), who observed that this change would result in a model that more accurately described observations.

The extensive duration of our measurements enabled us to consider the impact that $U_*$ has on deposition velocity in modifying the empirical coefficients to better fit our data and previously published data. Over the accumulation mode, our observations from the Manitou Experimental Forest suggest that for small particles (<100 nm), the Zhang et al. (2001) tends to overestimate the deposition velocity as a function of $U_*$. Within the heart of the accumulation mode (150-285 nm) the existing parameterization appears to capture the deposition velocity quite well, and beyond 400 nm the counting statistics and uncertainty begin to dominate and limit our ability to suggest concrete conclusions. Above 400 nm our parameterization as a function of $U_*$ shows a deposition velocity that is a factor of 2 or more above the Zhang et al. (2001) model.

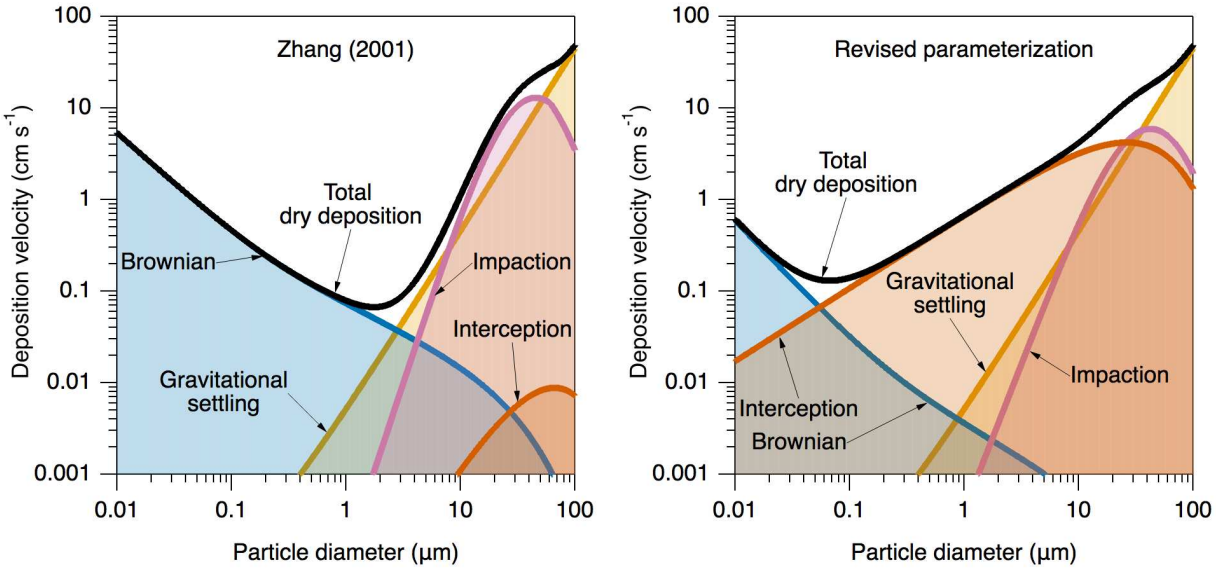


**Figure 3.2:** Dry deposition parameterization from Zhang et al. (2001) used in GEOS-Chem and a revised parameterization based on the work by Zhang et al. (2001). Shown is the deposition velocity contribution of the three collection efficiencies governing the surface resistance and the gravitational settling velocity. Models are both for evergreen needle leaf land use types, friction velocity ($U_*$) = 0.4 m $s^{-1}$, and an assumed particle density of 1500 kg $m^{-3}$.

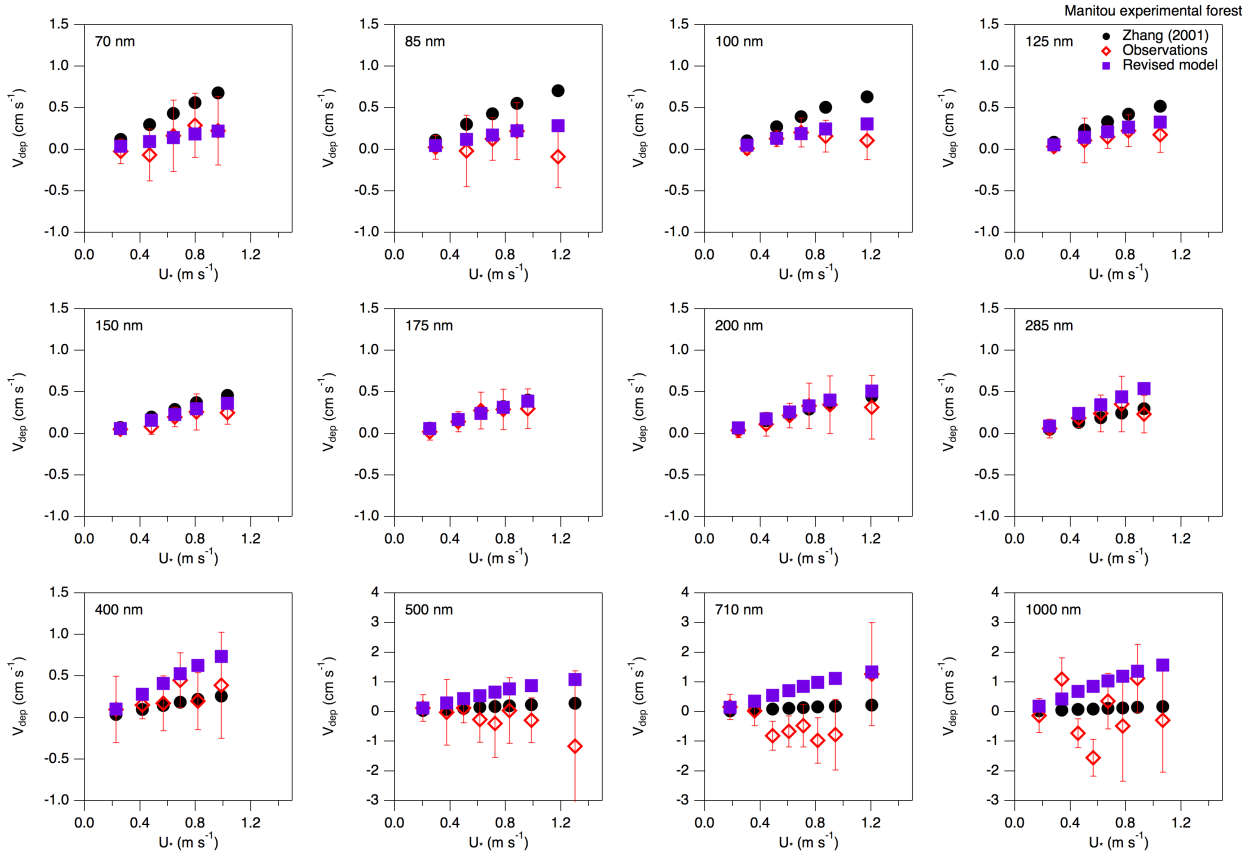


**Figure 3.3**: Direct deposition velocity measurements from the Manitou Experimental Forest binned by friction velocity (N=200 per bin). Also shown is the Zhang et al. (2001) used in GEOS-Chem and a revised parameterization.

Our data lack the certainty above 400 nm to accurately re-parameterize the model as a function of $U_*$ – but the existing literature for particle sizes beyond our measurements fills in the gaps. These data are also considered in our revised parameterization. Deviations from measurements in concert with the $U_*$ functionality arrive at a modified parameterization that describes observations across a variety of land use types. Over the land use types presented in Figure 3.4, many observations are captured with a 5x bounding factor over the 10x bounding factor that was used by Lee et al. (2013) in their assessment of uncertainties contributing to the CCN indirect effect uncertainty. Some of the measurements are not captured by the 5x bounding region, but the model shown uses an assumed $U_*$ which may not be representative of that measurement. $U_*$ is distinct from uncertainty as it is a parameter that is commonly measured and also used in the model. Analysis from our observations at SPiFFY suggest that a 5x bounding region describes 95% of the variability of measured deposition velocities compared to the revised model's predicted deposition velocity. There are fewer particle flux observations over the remaining land use types. However, available data suggests that deposition velocities over broadleaf forests and water surfaces show a similar sub-micron minima, which is far better captured by the revised parameterization. The parameterization over water surfaces is distinct from terrestrial surfaces because there is no interception parameter, but a stronger $U_*$ as there are only two collection efficiencies driving the shape of the curve. As water is the dominant surface over earth, this revision in dry deposition may have substantial consequences for the global atmospheric lifetime of particles. Particle flux observations over grasslands are less abundant, providing a key limitation for that surface, particularly for particles < ~100 nm

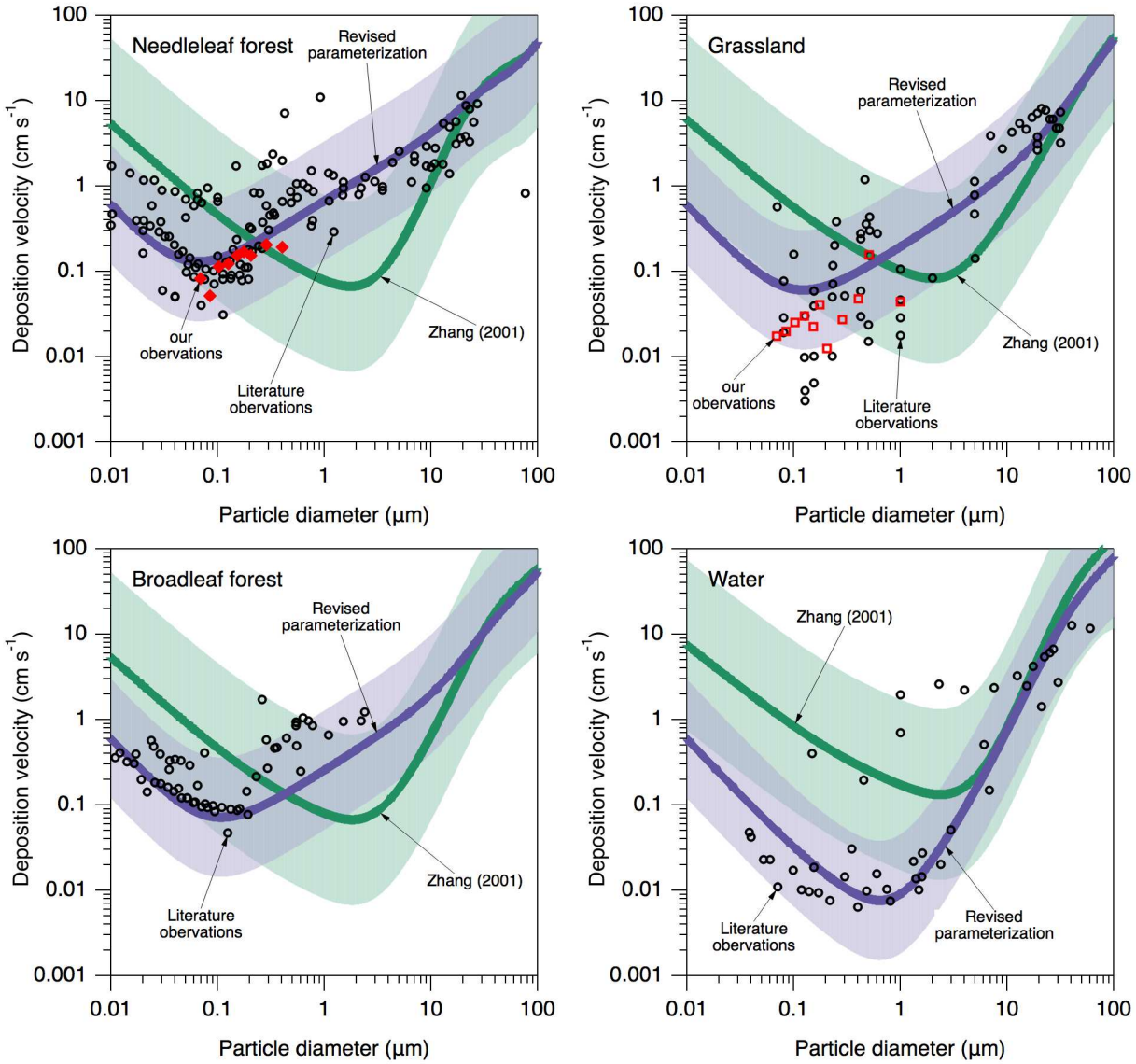


**Figure 3.4**: Dry deposition velocities as a function of particle diameter across four land use types used in GEOS-Chem. Literature observations are shown, as is the model parameterization currently in use in GEOS-Chem (green) with a two-orders of magnitude bounding range shown. The revised parameterization is shown in purple with a 5x bounding range shown. Observations that consider the $U_*$ are shown in red for the needle leaf and grassland land use types.

**Implications of a Revised Dry Deposition Parameterization**

A revised dry deposition model of this magnitude has substantial impacts aerosol processes globally. While deposition velocities of particles in the fine and accumulation modes decrease, particle concentrations for the N3 size bin decrease by 35% globally and a 33% decrease is also observed over land surfaces (averaged between the surface and 900 hPa). This modeled decrease is most prevalent over land surfaces and closer to the surface where $R_s$ term is dominant. Higher in the atmosphere the changes are less pronounced, but still substantial. Modeled decreases for the N3 size bin are attributed to efficient coagulation that occurs for small particle sizes. Particles in the N80 size range are modeled to increase substantially; a 56% increase globally and 36% increase over land surfaces. We primarily attribute this increase to the order of magnitude decrease in dry deposition velocities in the revised parameterization, but the likely increase in coagulation would contribute to the accumulation of particles in this size range. Ocean surfaces exhibit increases in particle concentration across much of the globe, size ranges, and altitudes with some exceptions observed for the N3 size range in Figure 3.5. Differences between the land and ocean behavior is largely driven by the differences in deposition velocities. Over land surfaces the revised parameterization suggests deposition velocities that are higher than the previous scheme for coarse mode aerosol, this is not the case for ocean surfaces. Ocean surfaces in the revised scheme have slower deposition velocities across all particle size ranges. Larger particles over land show a decrease in particle number concentration for sizes that the revised scheme suggests are depositing faster than previously thought. Given the magnitude of change for the revised dry deposition scheme, it is unsurprising that particle concentrations

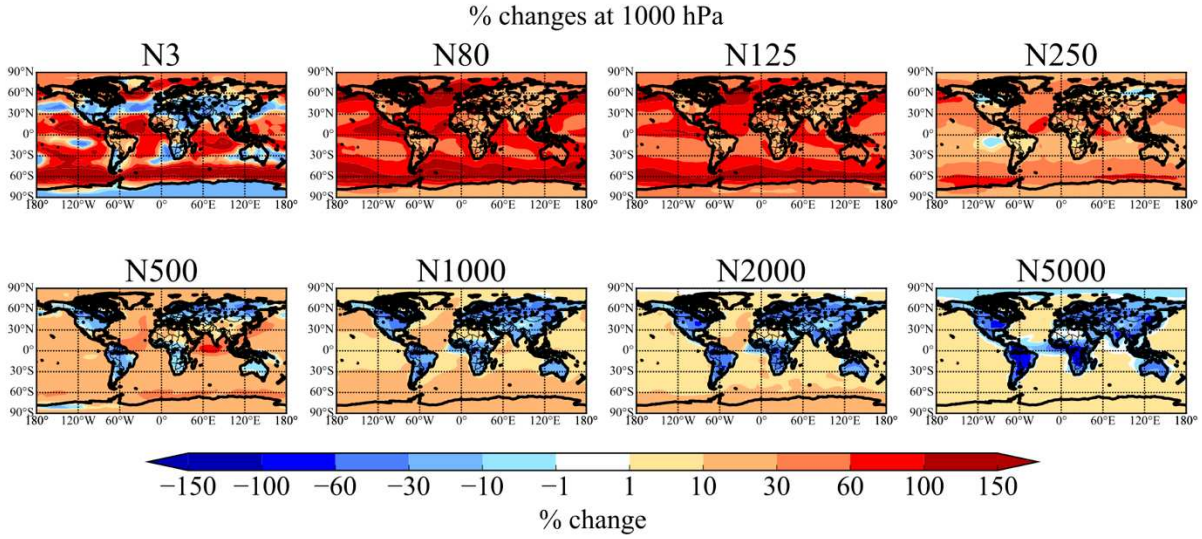


**Figure 3.5**: Percent change of aerosol concentration from base case GEOS-Chem model to the revised dry deposition parameterization. Size cutoffs such as N3 refer to all particle 3 nm and larger.

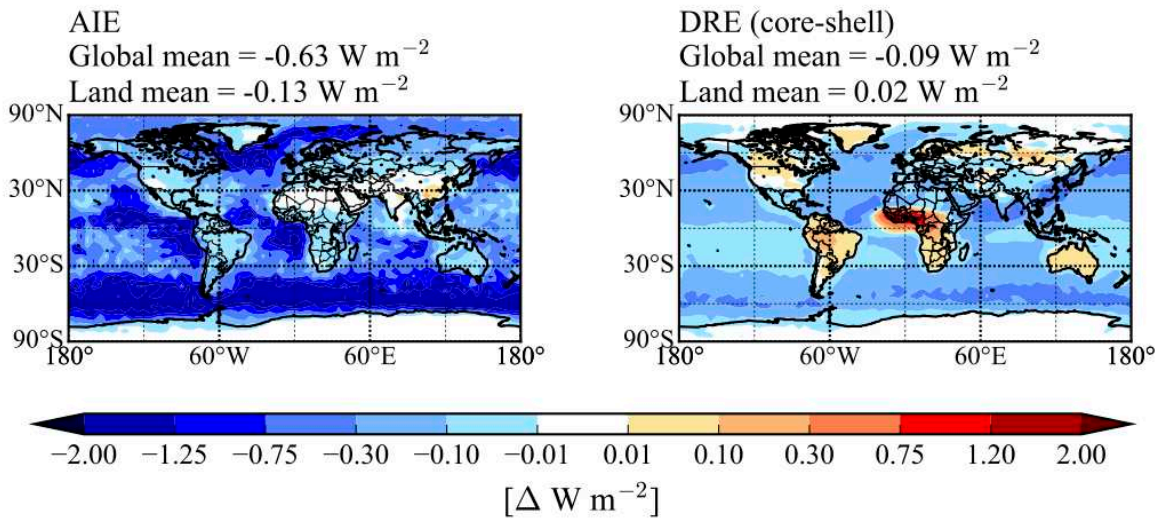


**Figure 3.6**: Changes in aerosol indirect effect (left) and direct radiative effect in W m$^{-2}$ compared to the base case model run.

The clear global changes in particle number concentration have a substantial impact on CCN and thus the aerosol indirect effect. CCN number concentrations increase by 12% which leads to a -0.63 W $m^{-2}$ decrease from the aerosol indirect effect over all land use types (Figure 3.6). Over land surfaces only, the decrease is not as substantial (-0.13 W $m^{-2}$). Ocean surfaces play a large role in the modeled aerosol indirect effect (e.g. Southern Ocean, Figure 3.6) as dry deposition velocities over that land surface type are reduced by an order of magnitude for CCN relevant particle sizes.

Changes in particle number concentration do not affect the aerosol direct effect as much as the indirect effect. However, the effect globally is still substantial with a modeled decrease of -0.09 W $m^{-2}$ globally. Land surfaces show a slight warming effect, 0.02 W $m^{-2}$, which is most pronounced over sub-Saharan Africa, South America, Australia, Greenland, and scattered parts of North America and Eurasia. Despite the substantial increases in particle concentrations over the oceans, a cooling effect from the direct effect is observed across all oceans except for the sub-Saharan outflow into the South Atlantic.

**Conclusion**

Using eddy covariance observations we suggest a revised parameterization to that one currently implemented in GEOS-Chem and other chemical transport models. This revised parameterization follows the framework suggested by Zhang et al. (2001) which is built upon the dry deposition scheme developed by Slinn (1982). Six empirical coefficients that affect the collection efficiencies of Brownian diffusion, impaction, and interception were modified to fit our observations over two land use surfaces while considering the overall shape of the deposition velocity curve that is described by observations collected by many other groups. Furthermore, we

consider the influence of friction velocity on deposition velocity in our measurement of accumulation mode particles.

The most significant change in the revised parameterization is the substantial increase of collection efficiency by interception. This change, coupled to changes in Brownian diffusion shift the deposition velocity minimum from 2 μm to 0.1 μm. While this is a substantial change, it is not unprecedented as others have suggested both observational evidence that this is occurring as well as revised parameterizations. By using a commonly employed parameterization we minimize the difficulty of implementation by simply changing six empirical coefficients to capture the bulk of observations across a variety of land use types.

From the compared dry deposition scheme to our suggested scheme the nature of the curve differs substantially. Across many land use types, the deposition velocity in the accumulation mode and submicron mode is approximately an order of magnitude slower. The two parameterizations have a crossover point slightly above the accumulation mode and at larger particle diameters past this crossover, deposition velocities are faster than previously modeled and suggests a shorter lifetime. For very coarse aerosol particles, the deposition velocities converge and there are minimal differences above 10 μm. The implications of this change are large. This suggests that submicron and accumulation mode particles across many land use types persist in the atmosphere longer than previously thought and that more coarse particles deposit out more quickly.

Our work suggests that dry deposition has generally been inaccurately described, there still exists uncertainty and spread within eddy covariance flux measurements. Process level insight into eddy covariance data is still needed, as are measurements across a variety of land use types and within grid boxes to capture spatial variability of sub-grid processes. There is also a substantial need to understand dry deposition under less ideal conditions as many eddy covariance data are

collected in remote sites with uniform terrain. Gaining process level insight into dry deposition processes across the size distribution will help reduce uncertainty in global climate models.

This work shows that dry deposition parameterizations used in many chemical transport models is an inaccurate representation. Our revised parameterization suggests an order of magnitude shift in where the dry deposition velocity minimum occurs and is now centered around the accumulation mode across most land use types. This shift, driven by observations, shows an order of magnitude decrease in particle dry deposition velocities for accumulation mode and fine mode particles. Coarse mode particles now have a higher dry deposition velocity. These changes result in a substantial change to the aerosol indirect effect (-0.63 W $m^{-2}$) due to an increase in CCN concentrations across the globe. Dry deposition is typically an overlooked parameter in global climate models, but we suggest that it requires much more attention given the magnitude of this change by a simple observationally driven change to the parameterization.

# CHAPTER 3 REFERENCES


Baldocchi, D. D., Hincks, B. B., and Meyers, T. P.: Measuring Biosphere-Atmosphere Exchanges of Biologically Related Gases with Micrometeorological Methods, Ecology, 69, 1331-1340, 10.2307/1941631, 1988.

Belot, Y., and Gauthier, D.: Transport of micronic particles from atmosphere to foliar surfaces, 1974.

Carslaw, K. S., Lee, L. A., Reddington, C. L., Pringle, K. J., Rap, A., Forster, P. M., Mann, G. W., Spracklen, D. V., Woodhouse, M. T., Regayre, L. A., and Pierce, J. R.: Large contribution of natural aerosols to uncertainty in indirect forcing, Nature, 503, 67-71, 10.1038/nature12674, 2013.

Deventer, M. J., Held, A., El-Madany, T. S., and Klemm, O.: Size-resolved eddy covariance fluxes of nucleation to accumulation mode aerosol particles over a coniferous forest, Agricultural and Forest Meteorology, 214-215, 328-340, 10.1016/j.agrformet.2015.08.261, 2015.

Emerson, E. W., Katich, J. M., Schwarz, J. P., McMeeking, G. R., and Farmer, D. K.: Direct Measurements of Dry and Wet Deposition of Black Carbon Over a Grassland, Journal of Geophysical Research: Atmospheres, 123, 12,277-212,290, 10.1029/2018jd028954, 2018.

Farmer, D. K., Cappa, C. D., and Kreidenweis, S. M.: Atmospheric processes and their controlling influence on cloud condensation nuclei activity, Chem Rev, 115, 4199-4217, 10.1021/cr5006292, 2015.

Finkelstein, P. L., and Sims, P. F.: Sampling error in eddy correlation flux measurements, J Geophys Res-Atmos, 106, 3503-3509, Doi 10.1029/2000jd900731, 2001.

Fischer, M. L., Billesbach, D. P., Berry, J. A., Riley, W. J., and Torn, M. S.: Spatiotemporal Variations in Growing Season Exchanges of CO2, H2O, and Sensible Heat in Agricultural Fields of the Southern Great Plains, Earth Interactions, 11, 1-21, 10.1175/ei231.1, 2007.

Foken, T., and Wichura, B.: Tools for quality assessment of surface-based flux measurements, Agricultural and Forest Meteorology, 78, 83-105, Doi 10.1016/0168-1923(95)02248-1, 1996.

Fulgham, S. R., Brophy, P., Link, M. F., Ortega, J., Pollack, I., and Farmer, D. K.: Seasonal flux measurements over a Colorado pine forest demonstrate a persistent source of organic acids, ACS Earth and Space Chemistry, 10.1021/acsearthspacechem.9b00182, 2019.

Gong, W., Makar, P. A., Zhang, J., Milbrandt, J., Gravel, S., Hayden, K. L., Macdonald, A. M., and Leaitch, W. R.: Modelling aerosol-cloud-meteorology interaction: A case study with a fully coupled air quality model (GEM-MACH), Atmospheric Environment, 115, 695-715, 10.1016/j.atmosenv.2015.05.062, 2015.

Hicks, B. B., Saylor, R. D., and Baker, B. D.: Dry deposition of particles to canopies-A look back and the road forward, Journal of Geophysical Research: Atmospheres, 121, 14,691-614,707, 10.1002/2015jd024742, 2016.

Houghton, J. T., and Intergovernmental Panel on Climate Change. Working Group I.: Climate change 2001 : the scientific basis : contribution of Working Group I to the third

assessment report of the Intergovernmental Panel on Climate Change, Cambridge University Press, Cambridge ; New York, x, 881 p. pp., 2001.
Kaimal, J. C., and Finnigan, J. J.: Atmospheric Boundary Layer Flows: Their Structure and Measurement, Oxford University Press, 1994.
Kouznetsov, R., and Sofiev, M.: A methodology for evaluation of vertical dispersion and dry deposition of atmospheric aerosols, J Geophys Res-Atmos, 117, Artn D01202 10.1029/2011jd016366, 2012.
Langford, B., Acton, W., Ammann, C., Valach, A., and Nemitz, E.: Eddy-covariance data with low signal-to-noise ratio: time-lag determination, uncertainties and limit of detection, Atmospheric Measurement Techniques, 8, 4197-4213, 10.5194/amt-8-4197-2015, 2015.
Lee, L. A., Pringle, K. J., Reddington, C. L., Mann, G. W., Stier, P., Spracklen, D. V., Pierce, J. R., and Carslaw, K. S.: The magnitude and causes of uncertainty in global model simulations of cloud condensation nuclei, Atmospheric Chemistry and Physics, 13, 8879-8914, 10.5194/acp-13-8879-2013, 2013.
Lee, P., McQueen, J., Stajner, I., Huang, J. P., Pan, L., Tong, D., Kim, H., Tang, Y. H., Kondragunta, S., Ruminski, M., Lu, S., Rogers, E., Saylor, R., Shafran, P., Huang, H. C., Gorline, J., Upadhayay, S., and Artz, R.: NAQFC Developmental Forecast Guidance for Fine Particulate Matter (PM2.5), Weather and Forecasting, 32, 343-360, 10.1175/Waf-D-15-0163.1, 2017.
Lohmann, U., and Feichter, J.: Global indirect aerosol effects: a review, Atmospheric Chemistry and Physics, 5, 715-737, 10.5194/acp-5-715-2005, 2005.
Mammarella, I., Rannik, Ü., Aalto, P., Keronen, P., Vesala, T., and Kulmala, M.: Long-term aerosol particle flux observations. Part II: Particle size statistics and deposition velocities, Atmospheric Environment, 45, 3794-3805, 10.1016/j.atmosenv.2011.04.022, 2011.
Massman, W. J.: A simple method for estimating frequency response corrections for eddy covariance systems, Agricultural and Forest Meteorology, 104, 185-198, Doi 10.1016/S0168-1923(00)00164-7, 2000.
Ortega, J., Turnipseed, A., Guenther, A. B., Karl, T. G., Day, D. A., Gochis, D., Huffman, J. A., Prenni, A. J., Levin, E. J. T., Kreidenweis, S. M., DeMott, P. J., Tobo, Y., Patton, E. G., Hodzic, A., Cui, Y. Y., Harley, P. C., Hornbrook, R. S., Apel, E. C., Monson, R. K., Eller, A. S. D., Greenberg, J. P., Barth, M. C., Campuzano-Jost, P., Palm, B. B., Jimenez, J. L., Aiken, A. C., Dubey, M. K., Geron, C., Offenberg, J., Ryan, M. G., Fornwalt, P. J., Pryor, S. C., Keutsch, F. N., DiGangi, J. P., Chan, A. W. H., Goldstein, A. H., Wolfe, G. M., Kim, S., Kaser, L., Schnitzhofer, R., Hansel, A., Cantrell, C. A., Mauldin, R. L., and Smith, J. N.: Overview of the Manitou Experimental Forest Observatory: site description and selected science results from 2008 to 2013, Atmospheric Chemistry and Physics, 14, 6345-6367, 10.5194/acp-14-6345-2014, 2014.
Peters, K., and Eiden, R.: Modeling the Dry Deposition Velocity of Aerosol-Particles to a Spruce Forest, Atmos Environ a-Gen, 26, 2555-2564, Doi 10.1016/0960-1686(92)90108-W, 1992.
Petroff, A., Mailliat, A., Amielh, M., and Anselmet, F.: Aerosol dry deposition on vegetative canopies. Part I: Review of present knowledge, Atmospheric Environment, 42, 3625-3653, 10.1016/j.atmosenv.2007.09.043, 2008.
Petroff, A., and Zhang, L.: Development and validation of a size-resolved particle dry deposition scheme for application in aerosol transport models, Geoscientific Model Development, 3, 753-769, 10.5194/gmd-3-753-2010, 2010.

Petroff, A., Murphy, J. G., Thomas, S. C., and Geddes, J. A.: Size-resolved aerosol fluxes above a temperate broadleaf forest, Atmospheric Environment, 190, 359-375, 10.1016/j.atmosenv.2018.07.012, 2018.
Pryor, S. C., Larsen, S. E., Sorensen, L. L., and Barthelmie, R. J.: Particle fluxes above forests: observations, methodological considerations and method comparisons, Environ Pollut, 152, 667-678, 10.1016/j.envpol.2007.06.068, 2008.
Rannik, Ü., Mammarella, I., Aalto, P., Keronen, P., Vesala, T., and Kulmala, M.: Long-term aerosol particle flux observations part I: Uncertainties and time-average statistics, Atmospheric Environment, 43, 3431-3439, 10.1016/j.atmosenv.2009.02.049, 2009.
Riley, W. J., Biraud, S. C., Torn, M. S., Fischer, M. L., Billesbach, D. P., and Berry, J. A.: Regional CO2and latent heat surface fluxes in the Southern Great Plains: Measurements, modeling, and scaling, Journal of Geophysical Research, 114, 10.1029/2009jg001003, 2009.
Saylor, R. D., Baker, B. D., Lee, P., Tong, D., Pan, L., and Hicks, B. B.: The particle dry deposition component of total deposition from air quality models: right, wrong or uncertain?, Tellus Series B-Chemical and Physical Meteorology, 71, Artn 1445379
10.1080/16000889.2018.1550324, 2019.
Schwede, D. B., and Lear, G. G.: A novel hybrid approach for estimating total deposition in the United States, Atmospheric Environment, 92, 207-220, 10.1016/j.atmosenv.2014.04.008, 2014.
Seinfeld, J. H., and Pandis, S. N.: Atmospheric chemistry and physics : from air pollution to climate change, 2nd ed. ed., J. Wiley, Hoboken, N.J., 2006.
Sisterson, D. L., Peppler, R. A., Cress, T. S., Lamb, P. J., and Turner, D. D.: The ARM Southern Great Plains (SGP) Site, Meteor Mon, 57, 10.1175/Amsmonographs-D-16-0004.1, 2016.
Slinn, S. A., and Slinn, W. G. N.: Predictions for Particle Deposition on Natural-Waters, Atmospheric Environment, 14, 1013-1016, Doi 10.1016/0004-6981(80)90032-3, 1980.
Slinn, W. G. N.: Some Approximations for Wet and Dry Removal of Particles and Gases from Atmosphere, Water Air Soil Poll, 7, 513-543, 1977.
Slinn, W. G. N.: Predictions for particle deposition to vegetative canopies, Atmospheric Environment (1967), 16, 1785-1794, 10.1016/0004-6981(82)90271-2, 1982.
Solazzo, E., Bianconi, R., Pirovano, G., Matthias, V., Vautard, R., Moran, M. D., Appel, K. W., Bessagnet, B., Brandt, J., Christensen, J. H., Chemel, C., Coll, I., Ferreira, J., Forkel, R., Francis, X. V., Grell, G., Grossi, P., Hansen, A. B., Miranda, A. I., Nopmongcol, U., Prank, M., Sartelet, K. N., Schaap, M., Silver, J. D., Sokhi, R. S., Vira, J., Werhahn, J., Wolke, R., Yarwood, G., Zhang, J. H., Rao, S. T., and Galmarini, S.: Operational model evaluation for particulate matter in Europe and North America in the context of AQMEII, Atmospheric Environment, 53, 75-92, 10.1016/j.atmosenv.2012.02.045, 2012.
Solomon, S., Intergovernmental Panel on Climate Change., and Intergovernmental Panel on Climate Change. Working Group I.: Climate change 2007 : the physical science basis : contribution of Working Group I to the Fourth Assessment Report of the Intergovernmental Panel on Climate Change, Cambridge University Press, Cambridge ; New York, viii, 996 p. pp., 2007.
Stocker, T.: Climate change 2013 : the physical science basis : Working Group I contribution to the Fifth assessment report of the Intergovernmental Panel on Climate Change, Cambridge University Press, New York, xi, 1535 pages. pp., 2014.

Wesely, M. L.: Parameterization of surface resistances to gaseous dry deposition in regional-scale numerical models, Atmospheric Environment (1967), 23, 1293-1304, 10.1016/0004-6981(89)90153-4, 1989.
Wilczak, J. M., Oncley, S. P., and Stage, S. A.: Sonic anemometer tilt correction algorithms, Boundary-Layer Meteorology, 99, 127-150, Doi 10.1023/A:1018966204465, 2001.
Wu, M., Liu, X., Zhang, L., Wu, C., Lu, Z., Ma, P.-L., Wang, H., Tilmes, S., Mahowald, N., Matsui, H., and Easter, R. C.: Impacts of Aerosol Dry Deposition on Black Carbon Spatial Distributions and Radiative Effects in the Community Atmosphere Model CAM5, Journal of Advances in Modeling Earth Systems, 10, 1150-1171, 10.1029/2017ms001219, 2018.
Zhang, J., and Shao, Y.: A new parameterization of particle dry deposition over rough surfaces, Atmospheric Chemistry and Physics, 14, 12429-12440, 10.5194/acp-14-12429-2014, 2014.
Zhang, L., and Vet, R.: A review of current knowledge concerning size-dependent aerosol removal, China Particuology, 4, 272-282, 10.1016/s1672-2515(07)60276-0, 2006.
Zhang, L., and He, Z.: Technical Note: An empirical algorithm estimating dry deposition velocity of fine, coarse and giant particles, Atmospheric Chemistry and Physics, 14, 3729-3737, 10.5194/acp-14-3729-2014, 2014.
Zhang, L. M., Gong, S. L., Padro, J., and Barrie, L.: A size-segregated particle dry deposition scheme for an atmospheric aerosol module, Atmospheric Environment, 35, 549-560, Doi 10.1016/S1352-2310(00)00326-5, 2001.

# CONCLUSION – CONSIDERATIONS OF ATMOSPHERIC LIFETIME AND FUTURE MEASUREMENTS

This dissertation focuses on understanding the atmospheric evolution and lifetime of gas phase NOx, condensed phase refractory black carbon, and total scattering particles. These are three relevant pollutants for climatological effects and can adversely affect human health. Understanding the evolution and fate of these pollutants is imperative to understanding the magnitude of potential impacts.

NOx is a direct anthropogenic pollutant that interacts with other gas phase radical species and volatile organic compounds in a catalytic cycle to form other criteria pollutants. Through direct measurements and zero-dimensional box modelling, we examine the sinks for NOx and volatile organic compounds that affect NOx sinks. The grouping of volatile organic compounds through positive matrix factorization into emission factors that co-vary allows for a thorough investigation into the drivers of criteria pollutants. The key pollutants formed through the coupled HOx-NOx cycles are ozone, nitric acid, and peroxy acetyl nitrate. Other compounds such as organic nitrates and peroxy nitrates are compounds that can be incorporated into organic aerosol or behave as a temporary NOx reservoir. The relative abundances of these compounds depend on several chemical factors: the chemical speciation in the atmosphere, overall abundance of volatile organic compounds, and NOx abundance. These factors dictate how likely a compound is likely to propagate ozone formation or terminate as nitric acid.

Ozone continues to be a heavily investigated pollutant in the Northern Colorado Front Range Metropolitan Area (NFRMA). The initial portion of this thesis focuses on understanding process level chemistry occurring in the NFRMA through data analysis and modelling and yields similar conclusions to previous works. Measurements and modelling suggest that oil and natural

gas influence the trace gas reactivity and thus the reactive nitrogen partitioning through changes to $HO_x$-$NO_x$ cycling. Measurements also show that there is a biogenic influence and it can play a strong role due to the complex mechanism and high reactivity. This influence varies year to year depending on short term climatological effects. Perturbations to this catalytic cycle show that suppressing a single criteria pollutant may shift the problem to a different criteria pollutant. For example, as $NO_x$ reductions continue and volatile organic compound emissions remain the same or constant the concern may become nitric acid abundances which will react with gas phase ammonia present in the region to form particulate nitrate. To draw an intriguing comparison, recent literature out of the Salt Lake City region measured the composition of the particulate matter in the region and found that it was dominated by particulate nitrate. (Womack et al., 2019) While these measurements were conducted in the winter where air stagnated, a similar scenario exists in the NFRMA under cyclonic conditions. This suggests that understanding a single criteria pollutant to inform mitigation strategies can miss the underlying chemistry. A much broader understanding needs to be implemented that considers the many shunts from the $HO_x$-$NO_x$ cycle and the role of other pollutants.

The second component of this dissertation is to directly measure dry deposition rates of black carbon and scattering aerosol. The single particle soot photometer is shown to be a robust instrument to measure black carbon deposition fluxes of total mass and particle number. Further work is required to use this instrument to perform size resolved particle fluxes of black carbon as evidenced by the uncertainty ranges shown in Figure 4.1 for refractory black carbon cores and core and coating. This is an especially important task as black carbon strongly impacts the climate through both the direct and indirect effects. (Bond, 2004;Bond et al., 2013) Black carbon has a strong effect in the Arctic, and direct measurements of black carbon deposition in that region are

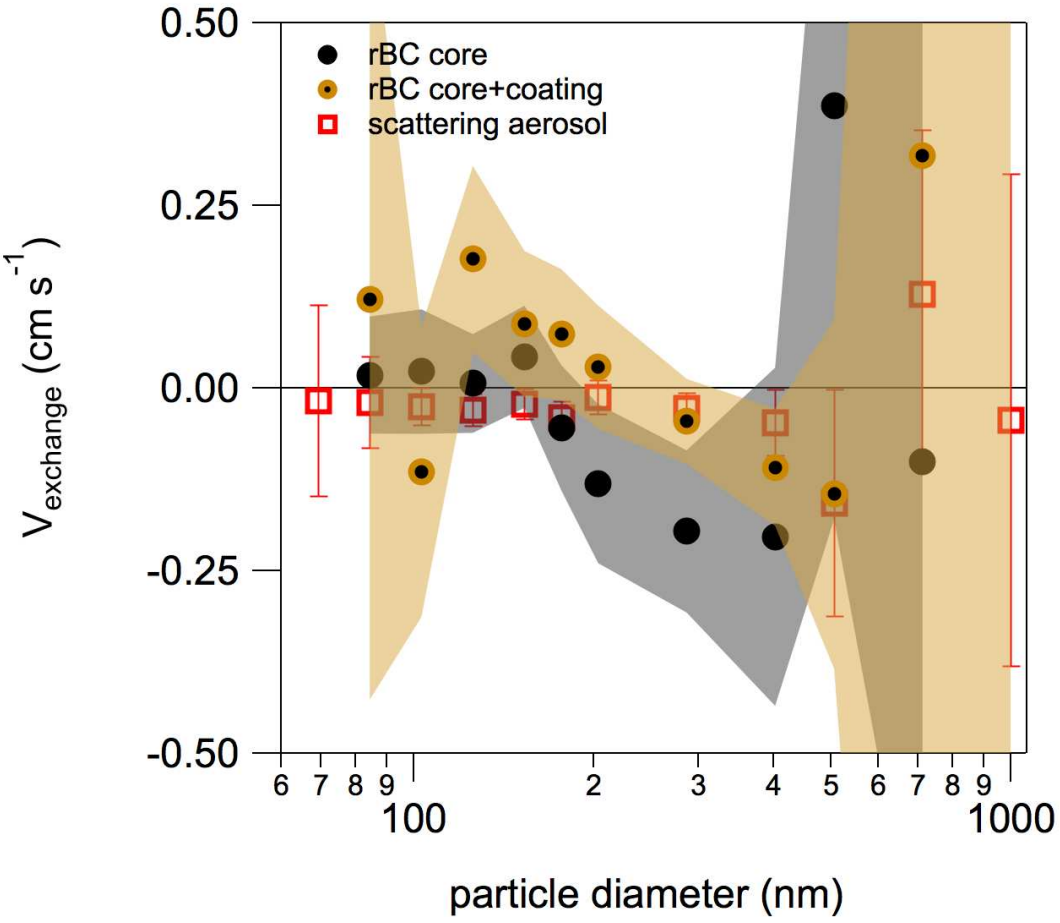


**Figure 4.1**: Size-resolved total scattering aerosol measurements along with size resolved refractory black carbon measurements considering just the core diameter as well as the core and coating diameter. Uncertainty ranges are shown as shaded ranges for refractory black carbon.

required to provide observational constraints on the magnitude and thus potential radiative impacts. Our preliminary analysis suggests that black carbon follows size resolved measurements of total scattering aerosol particles, but these data are limited by poor signal to noise due to limited counting statistics in each size bin. Changing the size resolved deposition scheme for black carbon will have a profound impact on global climate models (Wu et al., 2018).

Like several other previous studies, our observations indicate that the dry deposition scheme commonly implemented in global climate models is incorrect in size-dependence, magnitude and estimated uncertainty. Using aggregated observations from the literature and our extensive observations from the Manitou Experimental Forest and the Southern Great Plains, we suggest a revised scheme with a reduced role for Brownian diffusion and enhanced role for interception processes. This parameterization shifts the minimum deposition velocity to the accumulation mode and suggests that deposition in this range is slower by about one order of magnitude than previously modeled. These changes have a substantial impact on global climate models because particles in the accumulation mode are key cloud condensation nuclei. Particle concentrations change across all land use types and at all altitudes. Any process aerosol particles interact with are altered and includes cloud condensation nuclei, radiative forcing, PM2.5 concentrations, and a host of other effects.

This parameterization represents a step forward in reducing the uncertainty and improving the accuracy of climate and chemical transport models. However, more work could fully explore particle deposition - further eddy covariance measurements are needed. Empirical model parameterizations are only as good as the observations they use and over some environments (e.g. ocean surfaces) we are severely data limited. Additionally, physical models provide process level insight that empirical models lack, but elucidating physical models is challenging as substantial

amounts of data are required to fully explain observed phenomena. Further improvements are needed to reduce uncertainty and gain greater insights into process level phenomena.

Dry deposition is a significant driver of uncertainty in global climate models (Lee et al., 2013). Chapter 3 of this dissertation highlights the substantial impact of a revised parameterization based on observations on particle concentration and the aerosol indirect effect. While the revised parameterization is grounded in observations, there is still work that can be done to further reduce parameterization uncertainty over many land use types where we are data limited (e.g. ocean, grassland, and urban environments). Short field campaigns take snapshots of a specific time and place and enable us to investigate underlying processes. Long term measurements (a year a more) are sparse. Long term monitoring sites sacrifice the diversity of sites, but they still allow for process level insight and capture the complexity and temporal variability of a single site. Keeping sophisticated instrumentation operational for long periods of time in potentially remote environments remains a stumbling block for long term eddy covariance flux measurements. Simplifying instrumentation to enable both long-term and numerous measurements is a promising research direction.

Fundamentally, this dissertation focuses the concept of atmospheric lifetime and two components that affect lifetime. The first is chemical lifetime and how changing volatile organic compounds, NO, and $NO_2$ impact production of pollutants relevant for human and ecological health in the NFRMA. The second component focuses on the lifetime of atmospheric particles (black carbon and scattering aerosol) and identifies dry deposition is an important contributor to particle lifetime. Furthermore, we identify that existing particle dry deposition schemes do not accurately describe particle dry deposition observations by more than an order of magnitude and

suggest a revised dry deposition scheme that has strong effect on atmospheric particle concentrations, lifetime, and the aerosol indirect effect.

Bond, T. C.: A technology-based global inventory of black and organic carbon emissions from combustion, Journal of Geophysical Research, 109, 10.1029/2003jd003697, 2004.

Bond, T. C., Doherty, S. J., Fahey, D. W., Forster, P. M., Berntsen, T., DeAngelo, B. J., Flanner, M. G., Ghan, S., Kärcher, B., Koch, D., Kinne, S., Kondo, Y., Quinn, P. K., Sarofim, M. C., Schultz, M. G., Schulz, M., Venkataraman, C., Zhang, H., Zhang, S., Bellouin, N., Guttikunda, S. K., Hopke, P. K., Jacobson, M. Z., Kaiser, J. W., Klimont, Z., Lohmann, U., Schwarz, J. P., Shindell, D., Storelvmo, T., Warren, S. G., and Zender, C. S.: Bounding the role of black carbon in the climate system: A scientific assessment, Journal of Geophysical Research: Atmospheres, 118, 5380-5552, 10.1002/jgrd.50171, 2013.

Lee, L. A., Pringle, K. J., Reddington, C. L., Mann, G. W., Stier, P., Spracklen, D. V., Pierce, J. R., and Carslaw, K. S.: The magnitude and causes of uncertainty in global model simulations of cloud condensation nuclei, Atmospheric Chemistry and Physics, 13, 8879-8914, 10.5194/acp-13-8879-2013, 2013.

Womack, C. C., MeDuffie, E. E., Edwards, P. M., Bares, R., de Gouw, J. A., Docherty, K. S., Dube, W. P., Fibiger, D. L., Franchin, A., Gilman, J. B., Goldberger, L., Lee, B. H., Lin, J. C., Lone, R., Middlebrook, A. M., Millet, D. B., Moravek, A., Murphy, J. G., Quinn, P. K., Riedel, T. P., Roberts, J. M., Thornton, J. A., Valin, L. C., Veres, P. R., Whitehill, A. R., Wild, R. J., Warneke, C., Yuan, B., Baasandorj, M., and Brown, S. S.: An Odd Oxygen Framework for Wintertime Ammonium Nitrate Aerosol Pollution in Urban Areas: NOx and VOC Control as Mitigation Strategies, Geophysical Research Letters, 46, 4971-4979, 10.1029/2019gl082028, 2019.

Wu, M., Liu, X., Zhang, L., Wu, C., Lu, Z., Ma, P.-L., Wang, H., Tilmes, S., Mahowald, N., Matsui, H., and Easter, R. C.: Impacts of Aerosol Dry Deposition on Black Carbon Spatial Distributions and Radiative Effects in the Community Atmosphere Model CAM5, Journal of Advances in Modeling Earth Systems, 10, 1150-1171, 10.1029/2017ms001219, 2018.

# APPENDIX A – DEVELOPMENT OF EDDYFARM: OPEN SOURCE PARTICLE FLUX PROCESSING SOFTWARE[4]

## Overview

Processing eddy covariance flux data presents a daunting task and for particle flux measurements there is no clear approach. Herein I document my approach, development and considerations for processing eddy covariance particle flux measurements. While this program is focused on processing particle flux measurements, it is easily adaptable to any other measurement technique. Further development of this software for that use is pending.

## Introduction

EddyFARM is not the only package that is capable of processing data for eddy covariance flux analysis. Other packages such as EddyPro, EddyUH, and TK3 are readily available packages, however it is not clear *how* they operate. These software packages present three challenges: (1) data formatting, it is necessary to get data of whatever format into the format they accept and (2) lack of transparency of how a calculation is performed, and (3) lack of ability to modify the software to meet the needs of a user. This is where EddyFARM is unique, IGOR Pro is capable of many import types of data and converting it into a 'wave' (essentially a vector) and EddyFARM operates with clear, commented, and referenced functions that allow for easy operation and modification. Additionally there is a graphical user interface (GUI) that allows for intuitive processing.

## EddyFARM

As mentioned previously this software is based on processing ultra high sensitivity aerosol

[4] This appendix is written to document the use of EddyFARM. This software will be available as a fully open source stand alone package with a GNU General Public License. A technical note regarding this software and comparisons is likely to be published. This was entirely written and developed by Ethan W. Emerson.

spectrometer (UHSAS; Droplet Measurement Technologies Inc., Longmont, Colorado, USA) data and sonic anemometer data.

*Pre-processing*

As with any processing there is a certain amount of preparation work that is required to process data. Firstly, the data needs to be loaded. In EddyFARM this can be done by simply selecting a folder with any number of '.xlsx' files. If only the first ten, last ten, or continuous subset is desired this can be achieved by 'Force Start/Stop' where values can be set to force start and stop based on the file list. This is typically one of the slowest steps and depends highly on the machine configuration and whether data is being pulled from an external hard drive which will slow the processing down substantially. Once data is loaded bin boundaries of the data will show up. These data can be subsequently re-binned by selecting any number of the data. The use of this is two-fold, first it allows more robust counting statistics to be developed, as it is ideal to have at least ten particles per tenth of a second per bin [*Vong et al.*, 2010], secondly, it allows for faster processing. If an error is made, that can be easily undone as the raw data is stored and never directly modified. Once the data has been re-binned, the total number of particles can be calculated, but note that this is always the complete total of particles and will include all bin. If something else is desired, a little bit of hunting through the code will be required to identify the component that needs to be modified. This can also be accomplished by understanding how to perform matrix operations in Igor and some quick renaming of the appropriate wave. It is necessary to calculate the concentration of particles for the units to work out in the flux calculation. This leverages the onboard measurements of the flow through the instrument to determine particle concentration. The calculation of dn/dlog(dp) can also be performed. All calculations can be found in the following manner: (1) "CTRL+T" (2) right click on any button (3) Go to button-whatever (4) read the

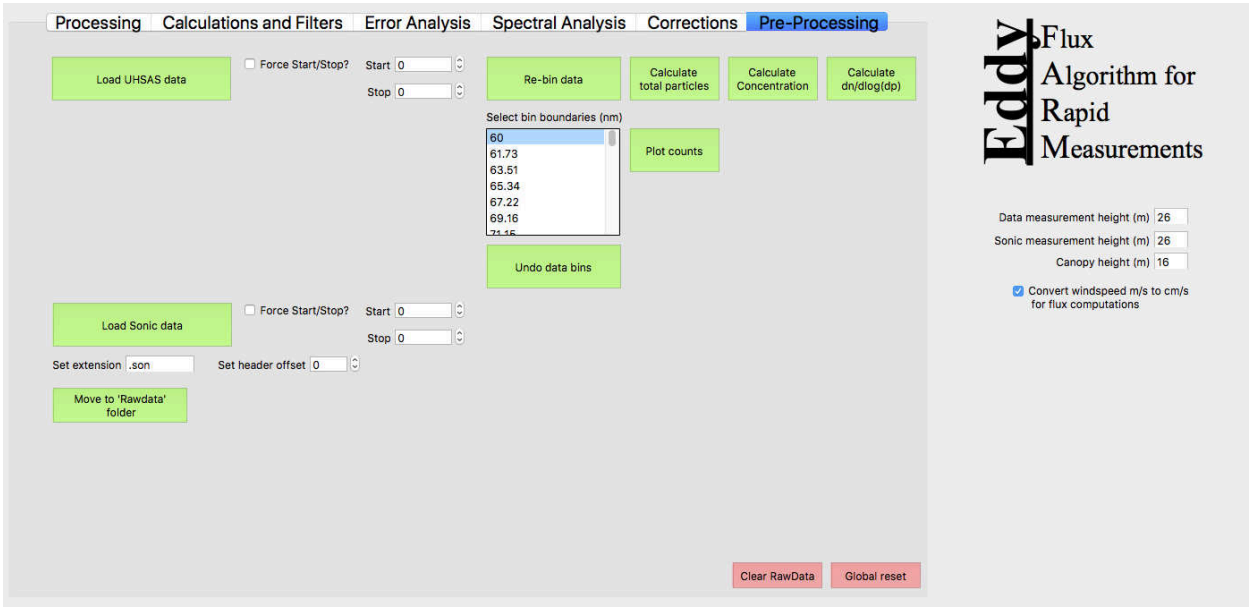


**Figure A.1**: Pre-processing panel.

function or go to the called function within the button function. Sonic data is currently based on a .son CSAT output and largely operates in the same manner as the UHSAS load data. Simply load the data and move on. The final step of pre-processing is to hit the 'Move to 'Rawdata' folder'. This combines the sonic and UHSAS data into a single data folder.

From here the focus moves to processing the data. First, on the far right under the logo there are three require inputs (1) data measurement height, (2) sonic measurement height, (3) canopy height. These inputs and the check box provide important data for subsequent processing and maintaining unit agreement. The processing from here continues to be straightforward; the drop down menus afford the user easy selection of the appropriate waves. Data wave must be in units that are consistent with a flux calculation (e.g. particle concentration in # $cm^{-3}$). The particle wave is used to keep track of the number of particles to be used in statistical analyses. All of the sonic data inputs are based in u, v, w coordinate format which appears to be commonly used. Temperature is essential for the calculation of sensible heat. Calculation of the wind direction and correction for not having the sonic aligned with true north can be adjusted as well. If this is not done, an error will surface or the program will execute it automatically. The assumption implemented in EddyFARM is that the timewaves for scalar and wind data are not the same and thus it is essential to assign them independently. There is an additional feature as it is common for the UHSAS and other instruments to keep track of housekeeping parameters (e.g. on board temperature, laser power, etc.) These parameters can be kept track of if data needs to be excluded based on criteria. Select the relevant housekeeping file and the corresponding timewave for that data, as they might be recorded on a lower resolution time basis.

Given that most instruments do not record on a precise frequency resolution it is necessary to grid the UHSAS and sonic data to the nearest time grid point. This allows for data recorded on

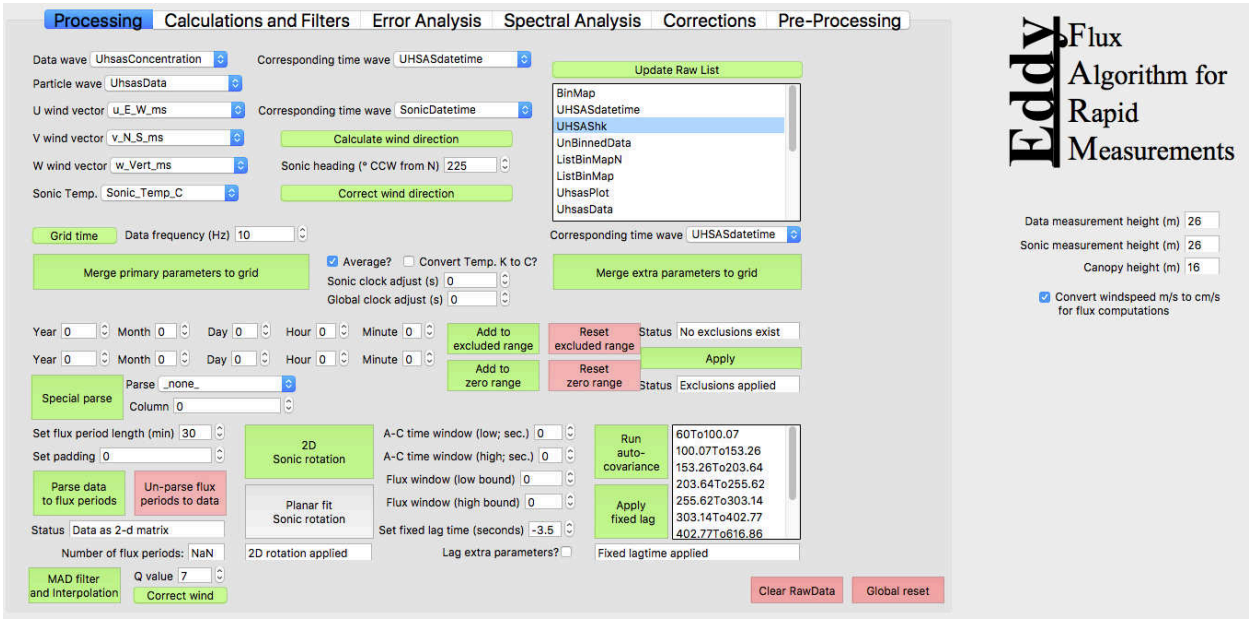


**Figure A.2**: Processing tab example

the highest resolution to be downscaled to 5 Hz, 1 Hz, or simply onto the desired 10 Hz data frequency. The following merge function can be executed in two ways, it can be merged as an average of data falling within half the range of the desired frequency or as a sum. Generally, concentration data is done as an average and particle number data is done as a sum. There is an open discussion as to whether it should be a sum then a re-calculation of concentration based on the average flow rate over the gridded data frequency. This is also the step where the sonic and data time waves are aligned. It is *critical* that the offset between these two is consistent over the duration of the campaign. This needs to be accounted for prior to processing by using clock-syncing software. A merge for the housekeeping parameters is done with a second button in the GUI.

Simple pre-filtering can be performed on the gridded data. This is setup for instances that would be known to confound the data analysis (e.g. exclude fire periods). This is done by selecting the range of influence and adding it to the excluded range. This can be a tedious process if there are many times that require data to be excluded. For data that can be excluded based on housekeeping data or diagnostic data there is a later section of code that is capable of handling that process. There is limited functionality to analyze zero periods separately and that is a realm of development that can be conducted. After exclusionary periods are added to this wave, it can be applied which 'NaNs' out data within exclusion periods. There is additional features that are in development such as a special parse function that is more flexible, but it does not currently exist.

The cleaned-up data is now suitable for processing into flux periods. Typically, data is parsed into 30-minute flux periods although it can be set shorter or longer. The assignment of a flux period length can be a recursive process if it is determined to be too short or greater statistics are required. This operation effectively converts data from a 2-dimensional matrix into a 3-

dimensional matrix where each layer represents a flux period, a column represents a binned particle size, and each row is a time point. This setup allows for computationally efficient operations to be conducted.[5] Once the data has been parsed into flux periods the number of flux periods is listed. This provides some insight into the dataset size for a given flux period length.

A first data consideration is to apply a median absolute deviation filter and interpolation. This is a de-spiking routine for sonic data that is commonly employed [*Hampel*, 1974]. Although this is common in eddy covariance flux analysis, other statistical approaches have been suggested [*Rousseeuw and Croux*, 1993]. Nonetheless the effect is to remove erroneous spikes in the data that can occur. This is a step that can be tested with and without. Plotting sonic data provides a useful indication as to whether or not this is necessary. Once sonic data has been de-spiked it is necessary to revise the wind direction calculation as that is likely to change subtly.

Sonic rotations are a key component of eddy covariance. It is a requirement of eddy covariance flux analysis to have the average vertical wind speed over the flux period length be zero [*Baldocchi et al.*, 1988; *Foken and Wichura*, 1996]. As of this dissertation, only a 2-dimensional sonic rotation is implemented. This is setup to force all horizontal wind into the U-direction and force the average vertical wind speed over the flux period length to zero. Once this has been applied the sonic data is fixed.

Another essential component of eddy covariance processing is the determination of lagtime. This is necessary for closed path sensors where there is a delay time between when a particle is sampled from a particular eddy to the time that it is actually measured by the instrument. There are two general approaches that are employed, a fixed lagtime and an auto-covariance lagtime. The first method is based on the pumping speed of the bypass pump and the internal

[5] There are substantially more places where computation speed can be increased by leveraging more matrix operations. There are a number of processes within EddyFARM that are slow.

diameter and length of the tubing used to transport particles from the sonic to the instrument. The auto-covariance lagtime is substantially different. For each flux period the data wave is lagged relative to the sonic in data frequency steps and the covariance is calculated. This is done for some window of time. For some scalar data a very clear maximum can be observed for a specific lagtime through the analysis [*Fulgham et al.*, 2019]. However, some methods will extract the absolute maximum covariance independent of the 'reality' of that lagtime within the window [*Langford et al.*, 2015]. The auto-covariance method can be run in EddyFARM, however there is no functionality to extract the maximum value. It is recommended that the data and lagtimes be carefully analyzed for all particle size bins as bias can occur if an incorrect lagtime is used. Generally, particles use a prescribed lagtime as it is rare for the auto-covariance analysis to yield a substantial peak [*Langford et al.*, 2015].

Following the lagtime analysis the workflow of EddyFARM shifts to processing the data into an eddy covariance flux. There are 14 different calculations provided in EddyFARM and they are shown in Table 1. These calculations can be used as filtering criteria (e.g. stationarity test) or to examine specific instances of a phenomenon (e.g. deposition under unstable conditions). The program allows for easy analysis that prints the corresponding stats of any particular parameter for a specific size bin if desired. Furthermore, it is possible to filter the data based on those 14 calculations and identify the number that meet a particular criteria. Additional filtering can be done for housekeeping and specific sonic parameters (e.g. filter out specific wind sectors or abberent voltages measured on the UHSAS). These filters can be applied one on top of another until quality controlled data are obtained. While many filters can be applied it is sometimes only necessary to apply one or two depending on the scientific question. Once all filtering is complete it is necessary to propagate the filtered data into another folder. To minimize unnecessary data only relevant

| Table 1: Calculations available in EddyFARM | |
|---|---|
| Calculation | Citation |
| Flux period stats | |
| Flux | [*Baldocchi et al.*, 1988] |
| Vertical exchange | [*Baldocchi et al.*, 1988] |
| Stationarity | [*Foken and Wichura*, 1996] |
| Friction velocity ($U_*$) | [*de Arellano et al.*, 2015] |
| Footprint | [*de Arellano et al.*, 2015] |
| Monin-Obukhov Length | [*Baldocchi et al.*, 1988] |
| Stability parameter | [*Moore*, 1986] |
| Integral timescale | [*Baldocchi et al.*, 1988; *de Arellano et al.*, 2015] |
| Roughness length | [*Baldocchi et al.*, 1988; *de Arellano et al.*, 2015] |
| ITC - W | [*Baldocchi et al.*, 1988; *de Arellano et al.*, 2015] |
| ITC - V | [*Baldocchi et al.*, 1988; *de Arellano et al.*, 2015] |
| Storage | [*Rannik et al.*, 2009] |
| Vertical loss | [*Kristensen et al.*, 1997] |

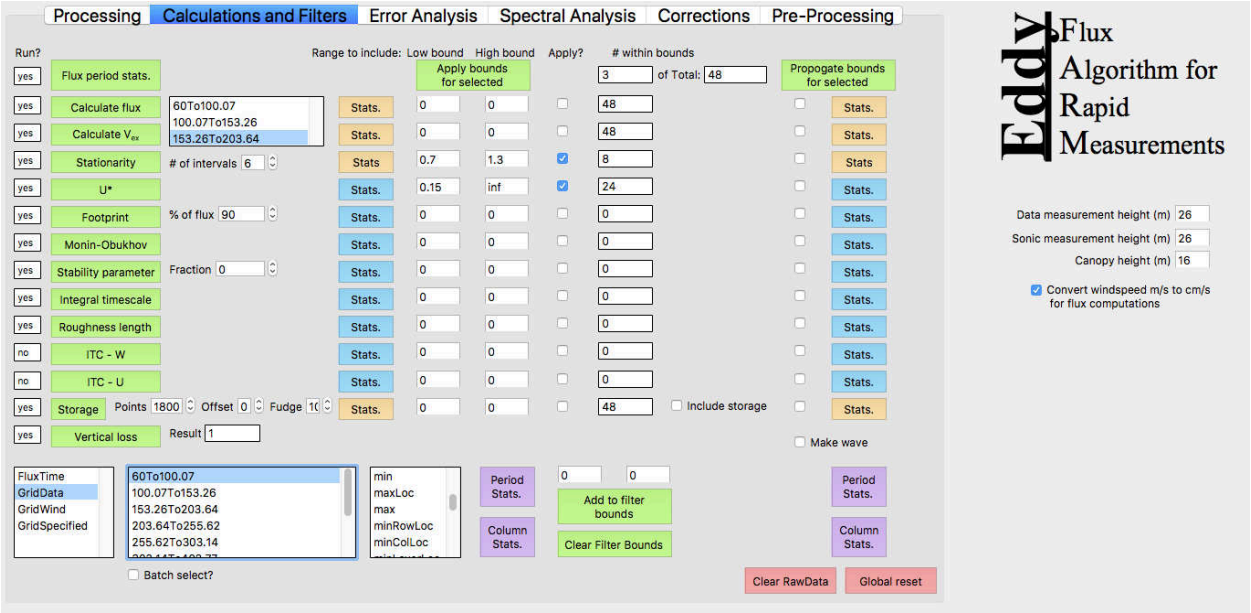


**Figure A.3**: Calculations and Filters tab example

waves need to be propagated. Statistics of the cleaned up waves can be accessed through the GUI.

It is important to examine the error associated with any flux period as well as the ensemble average. This can be done in a number of different ways in EddyFARM and this also allows for quick comparisons to be done between different error analysis methods. Table 2 summarizes the methods that are available in EddyFARM. These tend to be computationally slow as they result in many covariance calculations performed iteratively for a single flux period. The error analysis panel affords the opportunity to filter flux periods based on the error. What is not yet included is filtering for error that exceeds the magnitude of the flux. Flux error analysis is an active area of research and no clear consensus has been reached on what particular method to use, but careful examination is necessary to identify patterns and limitations. Literature suggests methods to determine an average uncertainty and limit of detection; and these have been used to provide a reasonable representation of error associated with a campaign [*Emerson et al.*, 2018; *Langford et al.*, 2015]. EddyFARM allows for the quality controlled data and error analysis data to be combined. Further refinement of quality controlled data based on the error analysis results can be performed.

Spectral analysis is the final component that is available in EddyFARM for eddy covariance processing. This allows for each flux period for each particle size bin to be analyzed. There are many types of spectral analyses that are possible with EddyFARM (co-spectra along with power, quad, amplitude, coherence, and phase spectra). These each have their uses, but most commonly the cospectral density and power spectral density are used for analysis. These spectral density plots are shown visually within the GUI and can be modified in the following ways: normalized by frequency, normalized by flux, and forced positive. Theory lines can be displayed as well to see if the spectra have the desired inertial subrange [*Kaimal and Finnigan*, 1994].

| Table 2: Error analysis methods for eddy covariance flux analysis | |
|---|---|
| Error Analysis Method | Citation |
| Billesbach | [*Billesbach*, 2011] |
| Finkelstein | [*Finkelstein and Sims*, 2001] |
| Random | [*Wienhold et al.*, 1995] |
| RMSE | [*Langford et al.*, 2015] |
| Wyngaard | [*Wyngaard and Izumi*, 1973] |
| Flux Uncertainty (counts) | [*Fairall*, 1984] |
| Counting uncertainty | [*Hinds*, 1999] |
| Whitenoise | [*Mauder et al.*, 2013] |

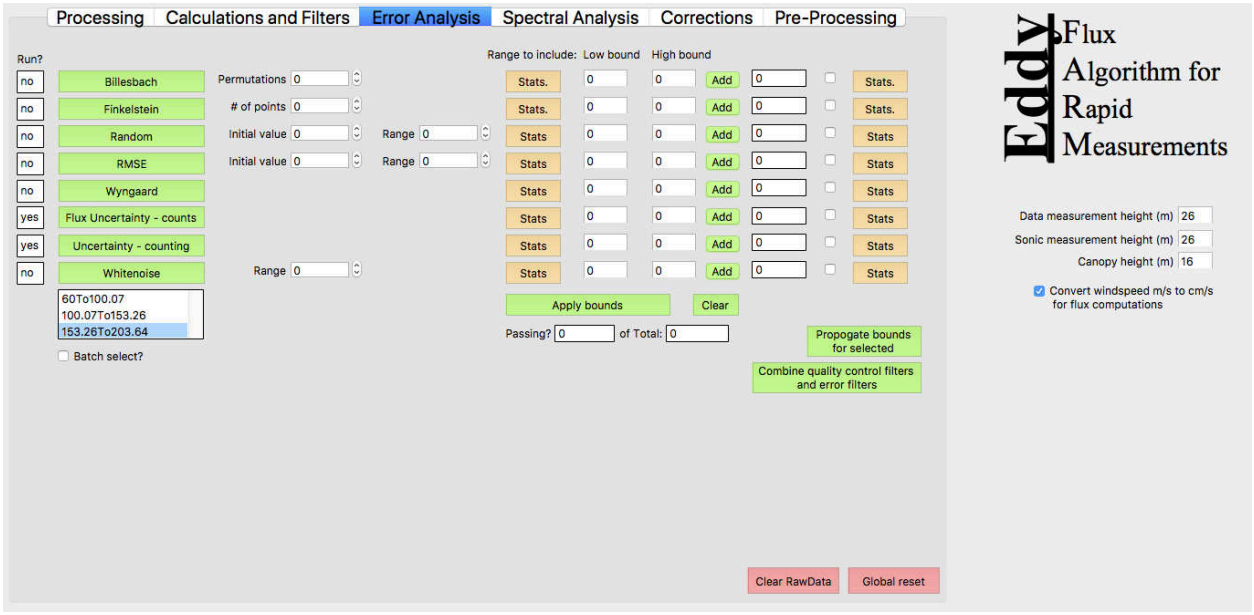


**Figure A.4**: Error analysis tab example

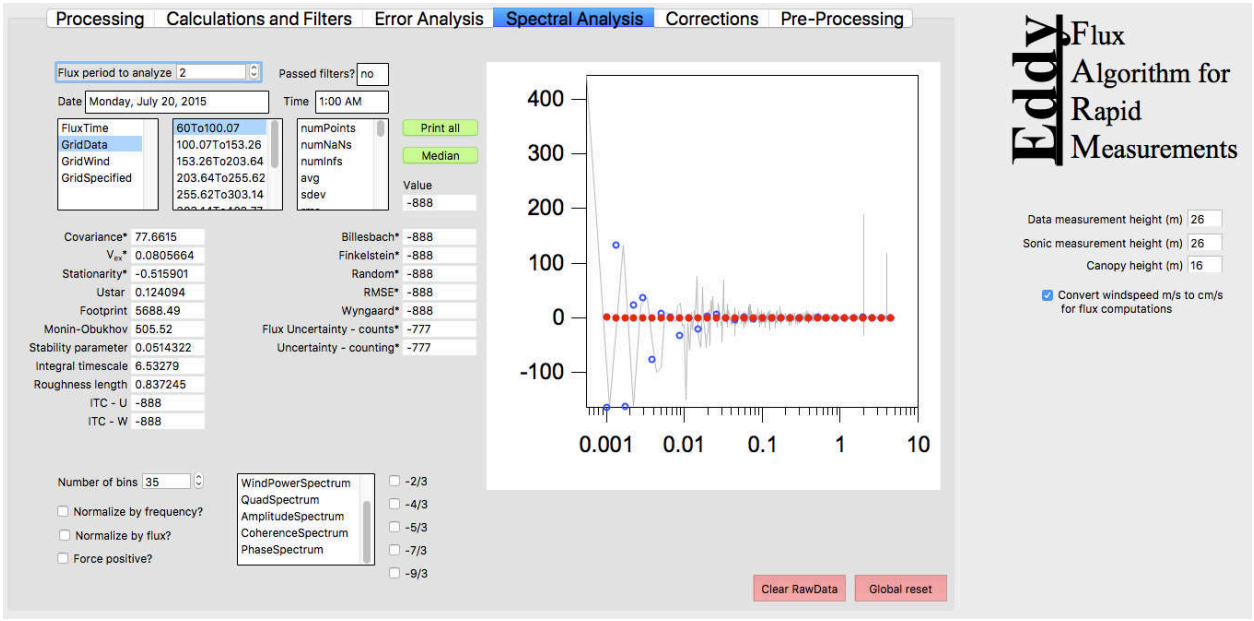


**Figure A.5**: Spectral analysis tab example

Additionally, all parameters that have been calculated in previous steps are called on and displayed in the GUI for rapid analysis.

**Conclusions**

EddyFARM is designed as a flexible platform to begin processing eddy covariance flux data. The software does not provide the 'answer' but it should aid in getting to interpretable flux data more quickly. This software has not undergone extensive validation against other processing programs, but the code is easily accessible and reasonably easy to check.

# APPENDIX A REFERENCES


Baldocchi, D. D., B. B. Hincks, and T. P. Meyers (1988), Measuring Biosphere-Atmosphere Exchanges of Biologically Related Gases with Micrometeorological Methods, *Ecology*, *69*(5), 1331-1340, doi:10.2307/1941631.

Billesbach, D. P. (2011), Estimating uncertainties in individual eddy covariance flux measurements: A comparison of methods and a proposed new method, *Agricultural and Forest Meteorology*, *151*(3), 394-405, doi:10.1016/j.agrformet.2010.12.001.

de Arellano, J. V. G., C. C. van Heerwaarden, J. H. van Stratum, and K. van den Dries (2015), *Atmospheric Boundary Layer: Integrating Air Chemistry and Land Interactions*, Cambridge University Press.

Emerson, E. W., J. M. Katich, J. P. Schwarz, G. R. McMeeking, and D. K. Farmer (2018), Direct Measurements of Dry and Wet Deposition of Black Carbon Over a Grassland, *Journal of Geophysical Research: Atmospheres*, *123*(21), 12,277-212,290, doi:10.1029/2018jd028954.

Fairall, C. W. (1984), Interpretation of Eddy-Correlation Measurements of Particulate Deposition and Aerosol Flux, *Atmospheric Environment*, *18*(7), 1329-1337, doi:Doi 10.1016/0004-6981(84)90041-6.

Finkelstein, P. L., and P. F. Sims (2001), Sampling error in eddy correlation flux measurements, *J Geophys Res-Atmos*, *106*(D4), 3503-3509, doi:Doi 10.1029/2000jd900731.

Foken, T., and B. Wichura (1996), Tools for quality assessment of surface-based flux measurements, *Agricultural and Forest Meteorology*, *78*(1-2), 83-105, doi:Doi 10.1016/0168-1923(95)02248-1.

Fulgham, S. R., P. Brophy, M. F. Link, J. Ortega, I. Pollack, and D. K. Farmer (2019), Seasonal flux measurements over a Colorado pine forest demonstrate a persistent source of organic acids, *ACS Earth and Space Chemistry*, doi:10.1021/acsearthspacechem.9b00182.

Hampel, F. R. (1974), Influence Curve and Its Role in Robust Estimation, *J Am Stat Assoc*, *69*(346), 383-393, doi:Doi 10.2307/2285666.

Hinds, W. C. (1999), *Aerosol technology : properties, behavior, and measurement of airborne particles*, 2nd ed., xx, 483 p. pp., Wiley, New York.

Kaimal, J. C., and J. J. Finnigan (1994), *Atmospheric Boundary Layer Flows: Their Structure and Measurement*, Oxford University Press.

Kristensen, L., J. Mann, S. P. Oncley, and J. C. Wyngaard (1997), How close is close enough when measuring scalar fluxes with displaced sensors?, *Journal of Atmospheric and Oceanic Technology*, *14*(4), 814-821, doi:Doi 10.1175/1520-0426(1997)014<0814:Hcicew>2.0.Co;2.

Langford, B., W. Acton, C. Ammann, A. Valach, and E. Nemitz (2015), Eddy-covariance data with low signal-to-noise ratio: time-lag determination, uncertainties and limit of detection, *Atmospheric Measurement Techniques*, *8*(10), 4197-4213, doi:10.5194/amt-8-4197-2015.

Mauder, M., M. Cuntz, C. Drue, A. Graf, C. Rebmann, H. P. Schmid, M. Schmidt, and R. Steinbrecher (2013), A strategy for quality and uncertainty assessment of long-term eddy-covariance measurements, *Agricultural and Forest Meteorology*, *169*, 122-135, doi:10.1016/j.agrformet.2012.09.006.

Moore, C. J. (1986), Frequency-Response Corrections for Eddy-Correlation Systems, *Boundary-Layer Meteorology*, *37*(1-2), 17-35, doi:Doi 10.1007/Bf00122754.

Rannik, Ü., I. Mammarella, P. Aalto, P. Keronen, T. Vesala, and M. Kulmala (2009), Long-term aerosol particle flux observations part I: Uncertainties and time-average statistics, *Atmospheric Environment*, *43*(21), 3431-3439, doi:10.1016/j.atmosenv.2009.02.049.

Rousseeuw, P. J., and C. Croux (1993), Alternatives to the Median Absolute Deviation, *J Am Stat Assoc*, *88*(424), 1273-1283, doi:Doi 10.2307/2291267.

Vong, R. J., I. J. Vong, D. Vickers, and D. S. Covert (2010), Size-dependent aerosol deposition velocities during BEARPEX'07, *Atmospheric Chemistry and Physics*, *10*(12), 5749-5758, doi:10.5194/acp-10-5749-2010.

Wienhold, F. G., M. Welling, and G. W. Harris (1995), Micrometeorological Measurement and Source Region Analysis of Nitrous-Oxide Fluxes from an Agricultural Soil, *Atmospheric Environment*, *29*(17), 2219-2227, doi:Doi 10.1016/1352-2310(95)00165-U.

Wyngaard, J. C., and Y. Izumi (1973), Statistical Characteristics of Reynolds Stress in a Turbulent Boundary-Layer, *Phys Fluids*, *16*(3), 455-456, doi:Doi 10.1063/1.1694364.

# APPENDIX B – SINGLE PARTICLE SOOT PHOTOMETER DATA PROCESSING AND LEADING EDGE ONLY FITTING ALGORITHM[5]

## Overview

The single particle soot photometer (SP2) is a powerful instrument. Its use is somewhat hampered by a lack of manufacturer provided software to extract and analyze the data easily. Software to process the data from the SP2 is readily available from the Paul Scherrer Institute and developed by Martin Gysel, this software is complicated and somewhat challenging to use. Given this gap, a simple approach to analyzing SP2 data and performing leading edge only fits is provided.

## Introduction

The single particle soot photometer (SP2; Droplet Measurement Technologies Inc., Longmont, Colorado, USA) is a robust instrument that is capable of measuring particle by particle data on the μs timescale [*Stephens et al.*, 2003]. Processing data from such an instrument is demanding as each particle results in data from 8 different channels. These data typically contain 50-200 points each and represent a signal that is measured from the instrument. The lack of an efficient and straightforward approach to process such data is bridged by SP2 Analysis package (written in Igor) discussed here. This serves as an overview of how processing SP2 using the SP2 Analysis package

## SP2 Analysis

The SP2 package exports data in a binary format (.sp2b) that is not readily obvious how it can be interpreted. Fundamentally this is used to track all of the relevant parameters the SP2

[5] This algorithm was entirely written and developed by Ethan W. Emerson. Joshua Schwarz provided valuable insight into the leading edge only fitting routine and approach.

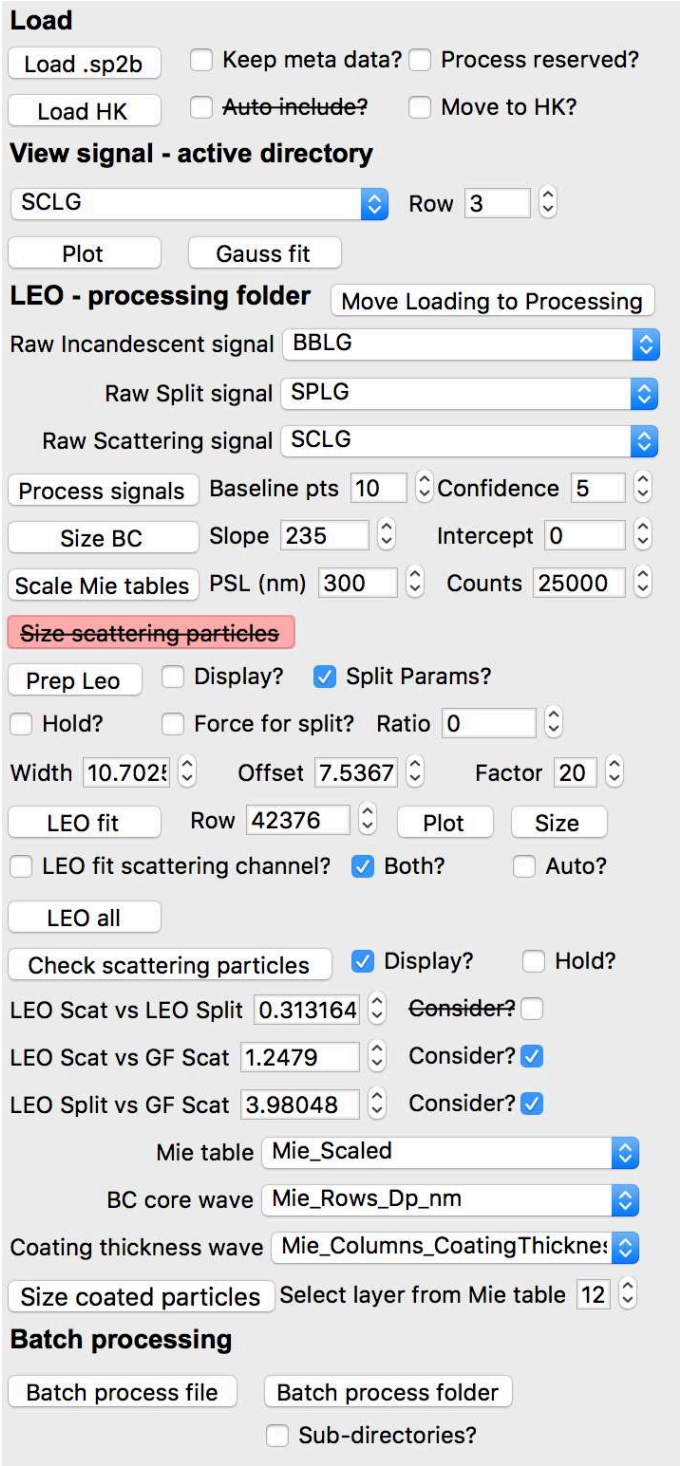


**Figure B.1**: SP2 Analysis processing panel.

outputs with the exception of the housekeeping data which is stored elsewhere and recorded on a different time resolution (typically) and saved every time the program to run the SP2 is opened (or daily).

This program begins with loading a .sp2b file to be processed. Figure B.1 shows the graphical user interface (GUI) of the SP2 Analysis program. Simply clicking the 'Load .sp2b' from the GUI will execute the procedure. It is important to note that this is structured around loading a single file at a time. However, there is code within the Igor procedure that makes it very clear how this could be modified to load many .sp2b files at a time. There are two check boxes to the right of this that ask two questions: 'keep meta data' and 'process reserved'. These can be checked at the users discretion. Meta data is data that is brought along with the .sp2b file, this is not essential for processing the signal data. The reserved data is extra columns essentially that exist in the .sp2b file, these are generally not used.[6] A critical component of loading .sp2b file is that Igor and the SP2 Analysis program understand the SP2 configuration used otherwise the data will be mislabeled and gross misinterpretation can occur. The 'Load_SP2_Single' function outlines how to define each channel using variables. This section is well commented and clearly explained, but it is essential to double check this regularly. Housekeeping data (.hk) data can also be loaded into the main folder although it is strongly recommended that this data is moved immediately to the housekeeping folder within the data browser of Igor.

Once data is loaded it is possible to view each and every signal individually from each channel. This is provided to check that signal visually look good and free of electronic noise or other oddities. Gaussian fits can be applied where appropriate (e.g. pure scattering particles from any scattering channel).

[6] At least as far as I know, I have never used the reserved waves for anything.

Here the program moves to processing the raw signals into something more manageable. This is done under the guise of the Leading Edge Only (LEO) processing, but if only refractory black carbon masses are desired, this can be accomplished. Begin by moving the data from the 'Loading' folder in the data browser to the 'Processing' folder, the GUI has a button for this. Assign the respective channels in the GUI appropriately. To process the signals this is done by selecting the 'Process Signals' button. This will output a matrix of data for every detection event recorded by the SP2, the contents of the matrix differs slightly for each channel. For the incandescent channel it contains the following: baseline average of the first n points, standard deviation of the baseline over those n points, maximum value, maximum value location, the amplitude, and a 'real' indicator. The first n points are defined by the user. For a signal to be 'real' that is also defined by the user to be the number of confidence intervals above the standard deviation from the baseline. This is an instance where there is a lack of redundancy in the program. There could be a second check with the other incandescent detector to ensure that an incandescent signal is recorded by both incandescent detectors. This offers the potential for further development. The split (position sensitive) channel has slightly different parameters that are extracted. Figure B.2 shows an example particle with the split detector shown. Processing the split detector results in tracking baseline average of the first n points, the standard deviation of the baseline, the first maximum height, maximum location, the zero crossing (interpolated over two points that go from positive to negative), the minimum, minimum location. Again, a particle that is above the set confidence interval times the standard deviation is defined as a real particle. The scattering detector is still different than the split detector as a Gaussian fit is performed on this signal and those parameters are extracted as well. The regular statistics of maximum, maximum location are obtained as well, but the data are focused on the Gaussian fit.

To size particles it is necessary to have a calibration for the incandescent channel. There is code and functions within the SP2 Analysis package to do so, but there are a variety of ways to do this. Generally, size selected fullerene soot is measured by the SP2 and that size selection is converted to mass using a Gysel parameterization. The counts measured are plotted vertically vs the mass. The slope of the best fit line is input into the GUI. This enables the program to size each incandescent particle. As of this writing there is no functionality to size scattering particles, but this addition would be straightforward and is discussed later.

The development and implementation of the leading edge only analysis is presented and discussed extensively elsewhere [*Gao et al.*, 2007].Generally, this is the method by which a core shell particle can be accurately sized using the SP2. This method works under the assumption that a scattering coating is made up of some organic coating that is vaporized by the 3 W 1064 nm Nd:YAG laser of the SP2. As the particle enters the beam it scatters almost instantaneously as it begins to heat up, at a certain point that coating boils and vaporizes and the scattering signal is degraded. After this the refractory black carbon core heats up and incandesces. On the SP2 this is observed as a degraded scattering signal that is decreasing in amplitude prior to the onset of the maximum of the incandescent signal.

A necessary first step in the LEO fitting analysis is to scale the provided Mie Theory tables based on poly styrene latex spheres (PSLs). To do this, simply input the diameter of the PSLs used and the scattering channel counts for the PSLs. This linearly scales the non-linear tables. These can be used as a lookup for a scattering particle diameter. The Mie Tables contain different layers that represent different assumed indexes of refraction for the coating, but a single index of refraction for refractory black carbon.

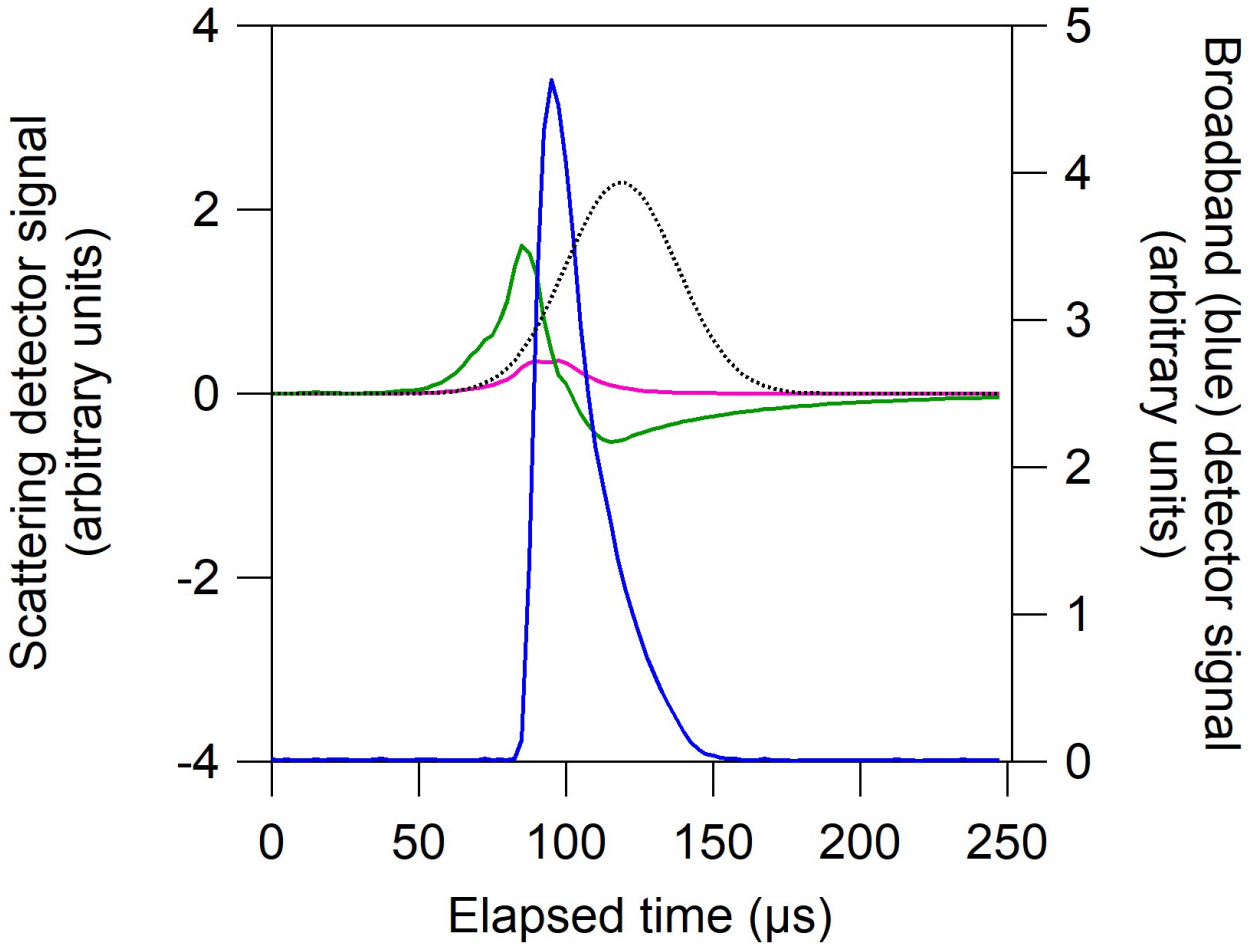


**Figure B.2**: Example detection events for an incandescent particle with some amount of scattering signal from a coating or the incandescent particle itself. The split (position sensitive) detector is shown in green, incandescent is shown in blue, the scattering channel is shown in pink, and a Gaussian leading edge only fit is shown in dashed black.

To prepare for LEO fitting it is necessary to determine some components that allow for a more accurate determination of the Gaussian signal from the degraded scattering signal. This is done by clicking the 'Prep LEO' button. This examines particles that have no observed incandescent signal and determining a number of LEO variables. Fundamentally there are two that are used for the LEO fitting. The first is the width of the Gaussian signal from the scattering channel which is independent of particle diameter. The second is the delay time between the zero crossing of the position sensitive detector to the center of the Gaussian signal (Figure B.3). With a constant flow rate this should not change. This allows three of the four parameters used in a Gaussian fit to be constrained:

$$F_{LEO}(x) = y_0 + A \exp\left\{-\left(\frac{(x - x_0)}{w}\right)^2\right\}$$

where $y_0$ is the baseline of the fit, constrained from each LEO fit, $x_0$ is the peak center which is set based on the delay time, and w which is the scattering signal width. LEO fits can be obtained in batch and examined one by one to test how the algorithm and instrument setup are operating.

It is essential to test how the LEO fit performs relative to a known quantity. The best way to do this with real data is to compare what the LEO fitting algorithm estimates relative to the Gaussian fit of the full scattering signal (Figure B.3). Ideally this should fall near the one to one line indicating that the LEO fitting only needs $1/20^{th}$ or so of the maximum signal to represent the Gaussian. This helps establish confidence in the approach. This also enables one to decide whether to LEO fit the scattering channel or the split channel, whichever one is more sensitive is best. This tends to be the split detector.

From here it is quick to analyze particles for the coating. This is done by selecting the appropriate Mie Tables, core waves, and coating thickness waves. The defaults of these should be correct. The particle core is calculated based on the lookup table as is the coating and appended to

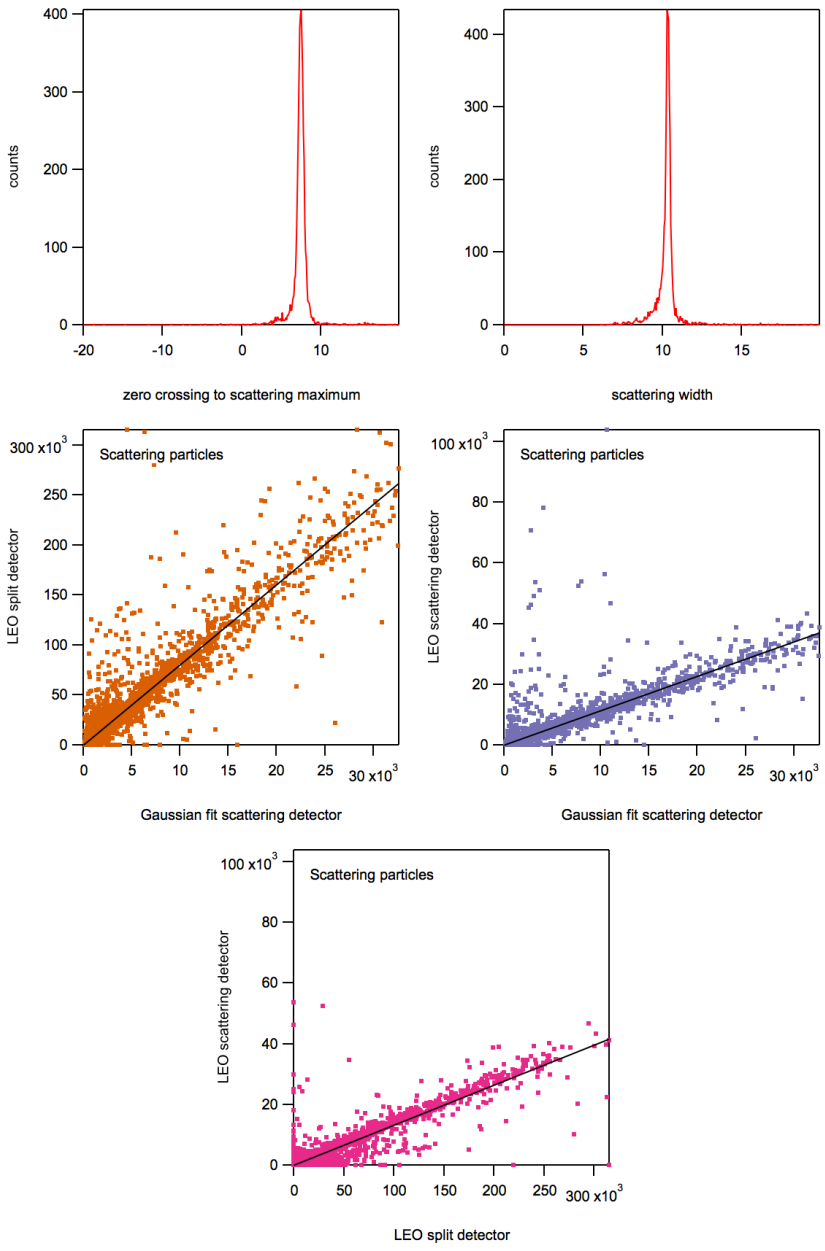


**Figure B.3**: Example of SP2 Analysis for LEO fitting. Top panels are histograms of scattering particles from a single .sp2b file. There is a very tight relationship between the zero crossing to scattering maximum on the left and then a very tight distribution of scattering widths. This is to be expected. The next three plots are examining the quality of a LEO fit. A linear relationship should exist between the LEO fits from the split detector and the scattering detector and the Gaussian fits for scattering only particles as those are 'the answer'. The slope does not necessarily have to be one for the LEO scattering vs the Gaussian Fit of the scattering detector, but that is helpful. A non-unity slope is accounted for. The LEO scattering vs LEO split detector slope indicates which detector is more sensitive.

the particle by particle information. Examining the limit of detection is an important component of the LEO fitting analysis. However, this has not been fully examined in the literature and something to be mindful of. There is uncertainty in these numbers and they should not be taken as fact. Thorough testing is needed to develop confidence in the algorithms representation of reality even if the math is well-grounded. Once this has been done it is straightforward to process entire folders and directories of data.

Some final considerations. It is imperative to maintain constant flow rates throughout experiments and if flows are changing this needs to be checked. This can be done by flowing PSLs through the instrument to determine the delay time as that changes with flow rate or simply sampling ambient air, there are plenty of purely scattering particles present. Additionally, frequent samplings of PSLs will help ensure appropriately scaled Mie tables and can account for changes in laser power.

**Conclusion**

The purpose of this appendix is to provide some helpful information to process SP2 data using the SP2 Analysis Code and some information regarding LEO fitting. LEO fitting in particular is nuanced and should not be taken for granted. This continues to be an active area of research and simply publishing data output from this program cannot be advised. However, it is a tool that can be used to analyze data and then test the tool to develop confidence in the data output.

# APPENDIX B REFERENCES

Gao, R. S., et al. (2007), A Novel Method for Estimating Light-Scattering Properties of Soot Aerosols Using a Modified Single-Particle Soot Photometer, *Aerosol Science and Technology*, *41*(2), 125-135, doi:10.1080/02786820601118398.

Stephens, M., N. Turner, and J. Sandberg (2003), Particle identification by laser-induced incandescence in a solid-state laser cavity, *Appl Opt*, *42*(19), 3726-3736, doi:10.1364/ao.42.003726.